UNIVERSITÀ DEGLI STUDI DI PADOVA

Facoltà di Scienze MM.NN.FF.

ISTITUTO NAZIONALE DI FISICA NUCLEARE

Laboratori Nazionali di Legnaro

in collaboration with Confindustria Veneto

MASTER THESIS

in

"Surface Treatments for Industrial Applications"

High temperature annealing for thermally diffused Nb_3Sn

Supervisor: Prof. V. Palmieri

Co-Supervisor: Dr. A.A.Rossi

Student: Dott. Atroshchenko Konstantin

Matr. N°: 1002712

Academic Year 2009-10

Contents

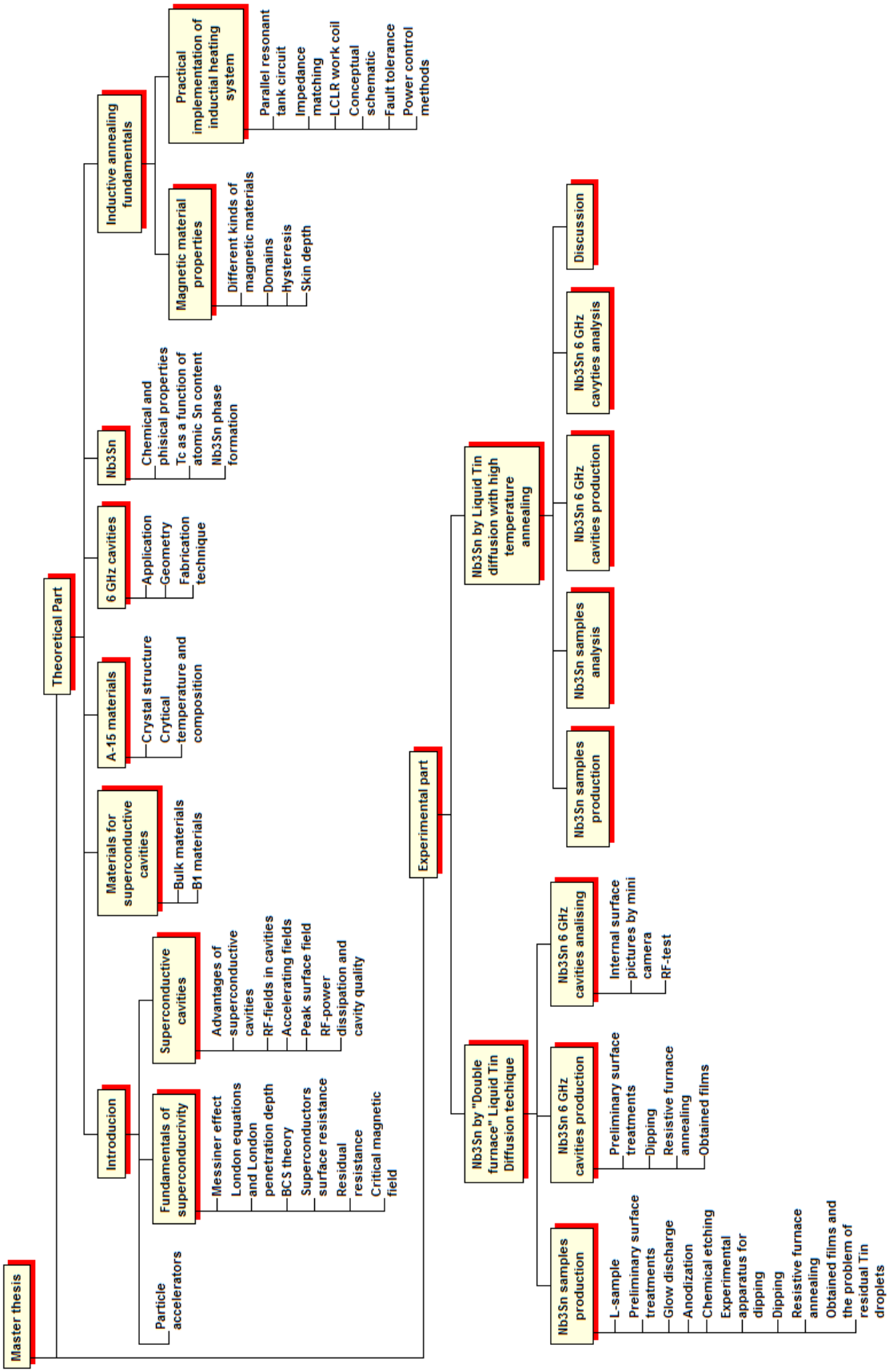
Master thesis
Theoretical Part
Introducion
Particle accelerators
Fundamentals of superconducrivity
Messiner effect
London equations and London penetration depth
BCS theory
Superconductors surface resistance
Residual resistance
Critical magnetic field
Superconductive cavities
Advantages of superconductive cavities
RF-fields in cavities
Accelerating fields
Peak surface field
RF-power dissipation and cavity quality
Materials for superconductive cavities
Bulk materials
B1 materials
A-15 materials
Crystal structure
Crytical temperature and composition
6 GHz cavities
Application
Geometry
Fabrication technique
Nb3Sn
Chemical and phisical properties
Tc as a function of atomic Sn content
Nb3Sn phase formation
Inductive annealing fundamentals
Magnetic material properties
Different kinds of magnetic materials
Domains
Hysteresis
Skin depth
Practical implementation of inductial heating system
Parallel resonant tank circuit
Impedance matching
LCLR work coil
Conceptual schematic
Fault tolerance
Power control methods
Experimental part
Nb3Sn by "Double furnace" Liquid Tin Diffusion techique
Nb3Sn samples production
L-sample
Preliminary surface treatments
Glow discharge
Anodization
Chemical etching
Experimental apparatus for dipping
Dipping
Resistive furnace annealing
Obtained films and the problem of residual Tin droplets
Nb3Sn 6 GHz cavities production
Preliminary surface treatments
Dipping
Resistive furnace annealing
Obtained films
Nb3Sn 6 GHz cavities analising
Internal surface pictures by mini camera
RF-test
Nb3Sn by Liquid Tin diffusion with high temperature annealing
Nb3Sn samples production
Nb3Sn samples analysis
Nb3Sn 6 GHz cavities production
Nb3Sn 6 GHz cavyties analysis
Discussion

Abstract

International Committee for Future Accelerators recommended that the Linear Collider design has to be based on the superconducting technology. And this is the reason why the international scientific society directed efforts to improving superconductive technology and reducing its cost.

In this work, in the framework of researching a valid alternative to Nb for RF superconducting cavities, thin film Nb_3Sn has been investigated. The goal will be the achievement of superconducting cavities working better than the Nb ones at 4.2 K.

In order to improve the existing technology of substrates coating by thermally diffused Nb_3Sn a new high temperature annealing technology has been developed. In the first part of the work, is given the short theoretical review of RF superconductivity, main superconductors that are used to be a good alternative to a pure Nb and fundamentals of the induction heating theory. Second part is dedicated to the existing double furnace technology, developed in the superconductivity lab in LNL. The influence of preliminary surface treatments like glow discharge of the sample, anodization and chemical etching on the quality of thermally diffused Nb_3Sn was studied. And in the third part is given the description of the new induction heating system, suggested for annealing of the 6 GHz cavities. Also in the third part we will go through the results of coating samples and cavities with thermally diffused Nb_3Sn with high temperature annealing and the results of the RF – test.

Finally, it is important to mention, that from the very beginning of investigation the induction heating for annealing 6 GHz cavities it became clear that the technology has an enormous potential in producing thermally diffused Nb_3Sn.

Introduction

0.1 Particle accelerators

In the past century, physicists have explored smaller and smaller scales, cataloguing and understanding the fundamental components of the universe, trying to explain the origin of mass and probing the theory of extra dimensions. And in recent years, experiments and observations have pointed to evidence that we can only account for a surprising five percent of the universe.

The International Linear Collider will give physicists a new cosmic doorway to explore energy regimes beyond the reach of today's accelerators. The proposed electron-positron collider (ILC) will complement the Large Hadron Collider, a proton-proton collider at the European Center for Nuclear Research (CERN) in Geneva, Switzerland, together unlocking some of the deepest mysteries in the universe. Consisting of two linear accelerators that face each other, the ILC will hurl some 10 billion electrons and their anti-particles, positrons, toward each other at nearly the speed of light. Accelerator cavities give the particles more and more energy until they smash in a blazing crossfire at the center of the machine. Stretching approximately 35 kilometers in length, the beams collide 14,000 times every second at extremely high energies (500 GeV). Each spectacular collision creates an array of new particles that could answer some of the most fundamental questions of all time. The current baseline design allows for an upgrade to a 50-kilometers, 1 TeV machine during the second stage of the project.

Planning, designing, funding and building the proposed International Linear Collider will require global participation and global organization. An international team of more than 60 scientists and engineers leads the Global Design Effort (GDE) for the ILC. The GDE team sets the design and priorities for the work of scientists and engineers around the world. From the senior physicist to the undergraduate student, about 2000 people from more than 100 universities and laboratories in over two dozen countries are collaborating to build the ILC, the next-generation particle accelerator.

0.2 Fundamentals of superconductivity

Superconductivity is the ability of certain materials to conduct electric current with practically zero resistance. This produces interesting and potentially useful effects. For a material to behave as a superconductor, low temperatures are required. Superconductivity was first observed in 1911 by H. K. Onnes, a Dutch physicist. His experiment was conducted with elemental mercury at 4K, the temperature of liquid helium. He observed that the electrical resistance disappeared completely near the T_c temperature, which is the characteristic of the material.

0.2.1 Meissner effect

The Meissner effect is the expulsion of a magnetic field from a superconductor during its transition to the superconducting state. Walther Meissner and Robert Ochsenfeld discovered the phenomenon in 1933 by measuring the magnetic field distribution outside superconducting tin and lead samples [1]. The samples, in the presence of an applied magnetic field, were cooled below what is called their superconducting transition temperature. Below the transition temperature the samples canceled all magnetic fields inside, which means they became perfectly diamagnetic. Perfect diamagnetism is the phenomenon when not only a magnetic field is excluded from entering a superconductor, but also that a field in an originally normal sample is expelled as it is cooled through T_c.

0.2.2 London equations and London penetration depth

The London equations, developed by brothers Fritz and Heinz London in 1935, relate current to electromagnetic fields in and around a superconductor. Perhaps the simplest meaningful description of superconducting phenomena, they form the genesis of almost any modern introductory text on the subject. A major feature of the equations is their ability to explain the Meissner effect, wherein a material exponentially expels all internal magnetic fields as it crosses the superconducting threshold.

There are two London equations when expressed in terms of measurable fields:

$$\frac{\partial j_s}{\partial t} = \frac{n_S e^2}{m} E \tag{0.1}$$

$$\nabla \times j_S = -\frac{n_S e^2}{mc} B \tag{0.2}$$

where

- j_s – the superconducting current;
- E and B – electric and magnetic fields within the superconductor;
- E – charge of an electron;
- M – electron mass;
- n_s – phenomenological constant loosely associated with a number density of superconducting carriers.

If equation (0.2) is manipulated by applying Ampere's law

$$\nabla \times B = \frac{4\pi j}{c} \tag{0.3}$$

then the result is the differential equation

$$\nabla^2 B = \frac{1}{\lambda^2} Bb \tag{0.4}$$

$$\lambda \equiv \sqrt{\frac{mc^2}{4\pi n_s e^2}} \tag{0.5}$$

Thus, the London equations imply a characteristic length scale, λ, over which external magnetic fields are exponentially suppressed. This value is the London penetration depth.

0.2.3 BCS theory

For classical superconductors like tin, a very successful microscopic theory was developed by Bardeen, Cooper and Schrieffer which is called BCS theory [2]. They assumed that electrons below T_c begin to condense to pairs of electrons, the so called Cooper pairs. The two electrons in a pair have opposite momentum and spin. They experience an attractive force mediated via quantized lattice vibrations called phonons. This bound state of the two electrons is energetically favorable. As the overall spin of these two paired electrons is zero, many of these pairs can co-exist coherently, just like other bosons. The coherence length describes the distance over which the electrons are correlated. It is given by:

$$\xi = \frac{\hbar v_F}{\Delta} \tag{0.6}$$

where:
v_F – velocity of the electrons near the Fermi level;
2Δ – energy necessary to break up a Cooper pair.

Typical values for the coherence length in niobium are around 39 nm. If one interprets the coherence length as the size of a Cooper pair, one immediately sees that it spans over many lattice constants. Within the BCS theory the energy gap can be calculated:

$$\Delta = 1.76 k_B T \tag{0.7}$$

The exact value of factor 1.76 in the relation of the energy gap and the critical temperature is material dependent and for niobium one finds higher values of $\Delta = 1.9 k_B T_c$. The number of Cooper pairs $n_{cooper} = n_s/2$ is temperature dependent and only at T = 0K all conduction electrons are condensed into Cooper pairs. The superconducting electrons co-exist with their normalconducting counterparts. The number of normalconducting electrons, n_n is given by the Boltzmann factor:

$$n_n(T \to 0) \approx n_s(0) exp\left(-\frac{\Delta(T)}{k_B T}\right) \tag{0.8}$$

0.2.4 Superconductor surface resistance

For a direct current or low frequency alternating currents the superconducting electrons shield the normalconducting electrons from the electromagnetic field so that no power is dissipated. But for alternating currents at microwave frequencies this is not really so. The inertia of the Cooper pairs prohibits them to follow the changing electromagnetic fields immediately, the shielding is not perfect. The normalconducting electrons start to flow and dissipate power. This gives rise to a resistance which depends on the number of normalconducting electrons and the frequency of the alternating current. For temperatures T < $T_c/2$ and energy of the microwave photons of $hf << \Delta$ the surface resistance can be approximated by:

$$R_{BCS}(T, f) = A \frac{f^2}{T} exp\left(\frac{-\Delta}{k_B T}\right) \tag{0.9}$$

The factor A depends on material parameters like coherence length, electron mean free path, Fermi velocity and penetration depth. For niobium the factor A is about 9×10^{-5} $\Omega K/(GHz)^2$. Therefore the BCS resistance at 1.3 GHz is about 600 nΩ at 4.2 K and about 1 nΩ at 2 K.

0.2.5 Residual resistance

The total surface resistance contains also a temperature independent part, which is called residual resistance R_s. The residual resistance is usually dominated by lattice imperfections,

chemical impurities, adsorbed gases and trapped magnetic field. Well prepared niobium surfaces show a residual resistance of a few nΩ [3].

$$R_s = R_{BCS}(T) + R_0 \tag{0.10}$$

Much is reported in literature about the possible origin of the residual resistance: both "physical phenomena" and "accidental mechanisms" (like dust, chemical residuals or surface defects on the cavity walls) contribute to parasitic losses. Due to the variety of the phenomena involved, it is very hard to express one formula predicting them.

0.2.6 Critical magnetic field

When the external field increases to some value, which is H_c so that the free energy of the superconducting state $F_s(H)$ becomes equal to the free energy of the normal state (F_n), the two phases are in equilibrium:

$$F_c(H) = F_n = F_s(H = 0) + \mu_0 V_s \int_0^{H_c} H dH \tag{0.11}$$

Here V_s is the superconductor volume. All the flux enters the superconductor at H_c, which is called the thermodynamic critical field.

0.3 Superconductive cavities

A superconducting cavity is the device used to provide energy to the particles that are crucial to an accelerator. Most commonly used are radio frequency (rf) cavities, an example of which is shown in Figure 0.1.

In the past, copper cavities were used for acceleration, but over the last 20 years, superconducting bulk niobium technology has proven itself as the alternative. A superconducting bulk niobium resonant structure has been successfully used in many machines: among them HERA and TESLA (DESY, Hamburg, Germany), CEBAF (Thomas Jefferson Laboratories, Newport News, Virginia, USA), the KEK B-factory (KEK, Tzukuba, Japan), the LHC (CERN, Geneva,

Switzerland). Superconductors have played a pioneering role at both the energy frontier and the high current one. Extensive research has therefore been performed to understand the performance limitations of superconducting cavities and to improve upon the achieved accelerating gradients.

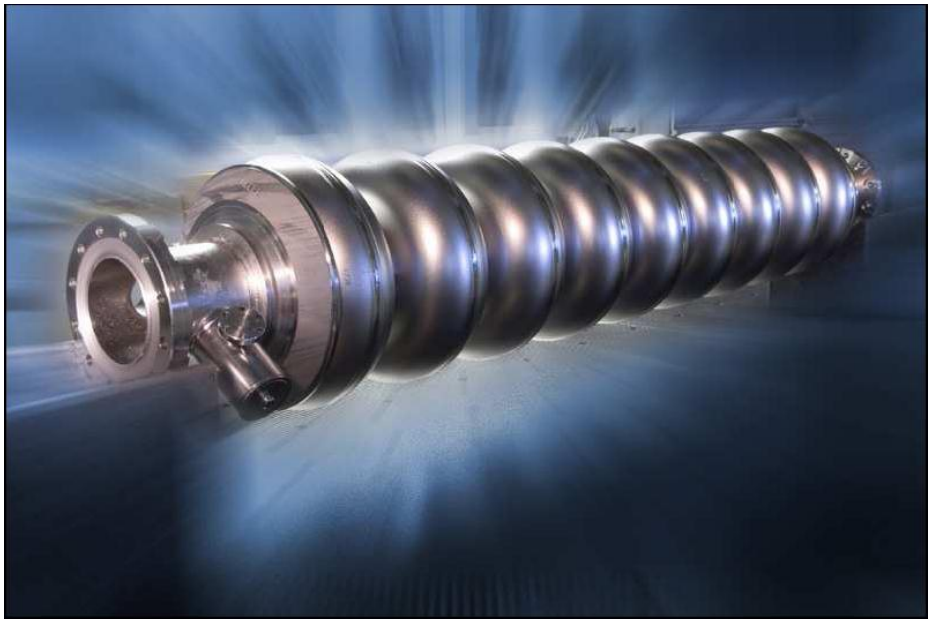

Figure 0.1. A bulk Niobium tesla – type 9 cells superconductive cavity

0.3.1 Advantages of superconductive cavities

Although not completely loss free above T = 0 K, as in the dc case, superconducting cavities dissipate orders of magnitude less power than normal conducting accelerating structures. The dramatically reduced resistivity translates into a number of very important advantages. They include:

1. *Operating cost savings*: Even when taking into account the cost of refrigerating superconducting cavities, their power demand in cw applications is more than two orders of magnitude less than that of equivalent copper cavities.

2. *Capital cost savings*: The reduced power requirements translate into capital cost savings, since fewer (and sometimes simpler) klystrons are needed.

3. *High gradient*: The relatively low power consumption also enables superconducting cavities to operate at high cw gradients.

4. *Reduced impedance*: The aperture of superconducting cavities is large; thereby minimizing disruptive interactions of the cavity with the beam, higher currents can therefore be accelerated.

0.3.2 RF – fields in cavities

The RF – field in cavities are derived from the eigenvalue equation

$$\left(\nabla^2 - \frac{1}{c^2}\frac{\partial^2}{\partial t^2}\right) \cdot \left(\frac{E}{H}\right) = 0 \tag{0.12}$$

which is obtained by combining Maxwell's equations [4]. It is subject to the boundary conditions

$$\hat{n} \times E = 0 \tag{0.13}$$

and

$$\hat{n} \times H = 0 \tag{0.14}$$

at the cavity walls. Here:

- $\hat{n}$ is the unit normal to the rf – surface;
- c is the speed of light;
- E and H are the electric and magnetic field respectively.

In cylindrically symmetric cavities, such as the pillbox shape, the discrete mode spectrum given by 0.1 splits into two groups, transverse magnetic I modes and transverse electric (TE) modes. For TM modes the magnetic field is transverse to the cavity symmetry axis whereas for TE modes it is the electric one to be transverse. For accelerating cavities, therefore, only TM modes are useful.

The typical shape of speed of light cavities [5] is shown in Figure 0.2.

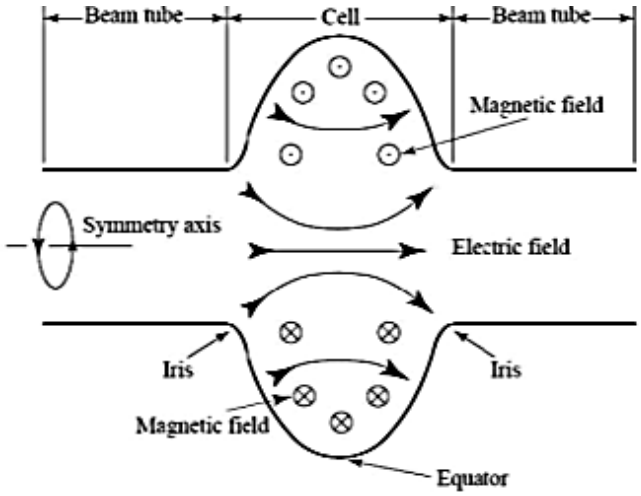

Figure 0.2. Schematic of a generic speed-of-light cavity. The electric field is strongest near the symmetric axis, while the magnetic field is concentrated in the equator region

0.3.3 Accelerating fields

The accelerating voltage (V_{acc}) of a cavity is determined by considering the motion of a charged particle along the beam axis. For a charge q, by definition,

$$V_{acc} = \left|\frac{1}{q} \times \max energy\ gain\ possible\ during\ transmit\right| \tag{0.15}$$

We use 6 GHz speed of light structures in our tests, and the accelerating voltage is therefore given by

$$V_{acc} = \left|\int_{z=0}^{z=d} E_z(\rho = 0, z) e^{\frac{iw_0 z}{c}} dz\right| \tag{0.16}$$

where:
d is the length of the cavity;
w_0 is the eigenfrequency of the cavity mode under consideration.
Frequently, one quotes the accelerating field E_{acc} rather than V_{acc}. The two are related by

$$E_{acc} = \frac{V_{acc}}{d} \tag{0.17}$$

0.3.4 Peak surface fields

When considering the practical limitations of superconducting cavities, two fields are of particular importance: the peak electric surface field (E_{pk}) and the peak magnetic surface field (H_{pk}). In most cases these fields determine the maximum achievable accelerating gradient in cavities. In the ones we have (6 GHz speed of light structures), the surface electric field peaks near the irises, and the surface magnetic field is at its maximum near the equator. To maximize the potential cavity performance, it is important that the ratios of $E_{pk} = E_{acc}$ and $H_{pk} = E_{acc}$ be minimized.

For example, the ratios of monocell TESLA – type cavities are [3]:

$$\frac{E_{pk}}{E_{acc}} = 1.83 \tag{0.18}$$

$$\frac{H_{pk}}{E_{acc}} = 45 \tag{0.19}$$

0.3.5 RF – power dissipation and cavity quality

To support the electromagnetic fields, currents flow in the cavity walls at the surface. If the walls are resistive, the currents dissipate power. The resistivity of the walls is characterized by the material dependent surface resistance R_S which is defined by the power P_d dissipated per unit area:

$$\frac{dP_d}{da} = \frac{1}{2} R_s |H^2| \tag{0.20}$$

In this case, H is the local surface magnetic field. Directly related to the power dissipation is an important figure of merit called the cavity quality (Q_0). It is defined as

$$Q_0 = \frac{w_0}{P_d} \tag{0.21}$$

U being the energy stored in the cavity. The Q_0 is just 2π times the number of rf cycles it takes to dissipate an energy equal to that stored in the cavity. For all cavity modes, the time averaged energy in the electric field equals that in the magnetic field, so the total energy in the cavity is given by

$$U = \frac{1}{2}\mu_0 \int_V |H|^2 dv = \frac{1}{2}\varepsilon_0 \int_V |E|^2 dv \tag{0.22}$$

where the integral is taken over the volume of the cavity. And the dissipated power could be written as

$$P_D = \frac{1}{2}\int_S R_S |H|^2 ds \tag{0.23}$$

where the integration is taken over the interior cavity surface. (By keeping R_S in the integral we have allowed for a variation of the surface resistance with position.) Thus is easy to find the equation for Q_0:

$$Q_0 = \frac{w_0 \mu_0 \int_V |H|^2 dv}{\int_S R_S |H|^2 ds} \tag{0.24}$$

The Q_0 is frequently written as

$$Q_0 = \frac{G}{\overline{R_s}} \tag{0.25}$$

where G is known as a geometrical factor of the cavity, and is given by

$$G = \frac{w_0 \mu_0 \int_V |H|^2 dv}{\int_S |H|^2 ds} \tag{0.26}$$

and $\overline{R_s}$ is the mean surface resistance (weighted by H^2) and is given by

$$\overline{R_S} = \frac{\int_S R_S |H|^2 ds}{\int_S |H|^2 ds} \tag{0.27}$$

For the 6 GHz cavities used in our laboratory G =287 Ω.

1. Materials for the superconductive cavities

The ideal material for superconducting cavities should exhibit a high critical temperature, a high critical field, and, above all, a low surface resistance. Besides, the material for superconducting cavities should be also a good metal in the normal state at low temperature. Unfortunately, these requirements can be conflicting and a compromise has to be found. To date, most superconducting cavities for accelerators are made of niobium. Thin films of other materials such as NbN, Nb_3Sn can also be used [6].

In the theoretical description of superconducting state (BCS theory) three main microscopy parameters need to be used [7]:

- g (ε_F): density of states at the Fermi energy
- *l* electron mean free path (due to impurity scattering)
- V_0: effective (phonon mediated) electron – electron interaction

These represent the effective number of free electrons, their scattering rate, and their (phonon mediated) effective attraction respectively. They can be written in terms of directly measurable corresponding macroscopic parameters:

γ: Sommerfeld constant = $(\pi^2/3) \cdot k_B^2 \cdot g(\varepsilon_F)$
ρ_n: residual resistivity $(1/RRR) = e^2/3 \cdot v_F \cdot g(\varepsilon_F)$
T_c: critical temperature = $1.14 \cdot \theta_D exp\left[-1/\left(V_0 \cdot g(\varepsilon_F)\right)\right]$

(being k_B the Boltzmann constant, RRR the residual resistivity ratio, v_F the Fermi velocity and Θ_D the Deby temperature). In the same frame, for a type II superconductor in the dirty limit, the relevant quantities for rf applications can be in turn expressed in terms of the following macroscopic parameters (CGS units, $T < T_c/2$): the BCS surface resistance (R_{BCS}), the penetration depth (λ), the critical fields (H_c and H_{c1}).

$$R_{BCS} = \frac{R_n}{\sqrt{2}}\left(\frac{\hbar w}{\pi \Delta}\right)^{\frac{3}{2}}\frac{\sigma_1}{\sigma_2} = A\sqrt{\rho_n}\frac{e^{\frac{-\Delta}{k_B T}}}{\sqrt{sT_s T}\left(1+e^{\frac{-\Delta}{k_B T}}\right)^2} w^2 ln\frac{\Delta}{\hbar w} \qquad (1.1)$$

$$\lambda = B\left[\frac{\rho_n}{\eta}T_c\right]^{-1} \qquad (1.2)$$

$$H_c = C \cdot \gamma^{1/2} \cdot \eta \cdot T_c \qquad H_{c1} = D\frac{B \cdot \eta \cdot T_c}{\rho_n} \qquad H_{sh} = 0.75 \cdot H_c \qquad (1.3)$$

where:

- η = s/3.52 = strong coupling correction;
- A = $6 \cdot 10^{-21}$, B = 10^{-2}, C = 2.4, D = $2 \cdot 10^{-4}$.

These approximated expressions clarify that for superconducting alloys and compounds, at a given operating temperature, the best rf performances (low surface resistance and λ, high relevant critical fields) are obtained for high Tc and low ρ_n materials.

For the superconducting cavities could be used:

- Bulk Nb;
- B1 components (structure AB);
- A15 materials (structure A_3B).

1.1 Bulk metals

Lead, as an archetype of a type I superconductor, has been used for low frequency cavities, and has yielded a very low residual surface resistance. It is cheap, and easily available in a pure form. Unfortunately, at frequencies higher than a few hundred MHz, the BCS surface resistance becomes prohibitive, due to the low critical temperature of this material. Moreover, it has poor mechanical characteristics and oxidizes easily, with a subsequent degradation of the properties of the superconducting surface. For these reasons, lead tends to be progressively replaced by niobium, and is now confined to low frequency applications.

In view of the above criteria, Nb appears as a serious candidate for superconducting cavities. It has the highest *T*c of all pure metals. Being a soft type II superconductor, it occupies a position of compromise between the four requirements mentioned above. Niobium homogeneity and purity are important issues for RF applications because it determines the thermal stability of the cavity. It was quickly realized that a frequent gradient limitation in superconducting cavities is due to thermal instabilities triggered by microscopic hot spots, for example normal conducting inclusions.

Comparison of the superconductive properties of Lead and Niobium is given in the table 1.1:

Material	T_c, (K)	λ, (nm)	ξ_0, (nm)
Pb (type 1)	7,2	39	83-92
Nb (type 2)	9,2	32-44	30-60

Table 1.1. Comparison of bulk – metal superconductors

1.2 B1 materials

Among B1 compounds, only few Nitrides and Carbides have critical temperatures higher than that one of Niobium. Table 1.2 reports the B1 compounds that have been found superconductors [8].

B \ A	Sc	Y	La	Ti	Zr	Hf	V	Nb	Ta	Cr	Mo	W	Re
B					3.4	3.1							
C	<1.38	<1.38		3.42	<0.3	<1.20	0.03 3.2*	12	10.35		14.3	10.0	3.4
N	<1.38	<1.4	1.35	5.49	10.7	8.83	8.5	17.3	6.5	<1.28	5.0	<1.38	
P			<1.68										
Sb		<1.02	<1.02										
O				2.0			<0.3	1.39					
S	<0.33	1.9	0.87		3.3								
Se	<0.33	2.5	1.02										
Te		2.05	1.48										

* T_C = 3.2 K was registered in vanadium carbide after implantation of C^+ ions

Table 1.2. T_c of different B1 compounds

The lattice structure of B1 materials is shown on the picture 1.1.

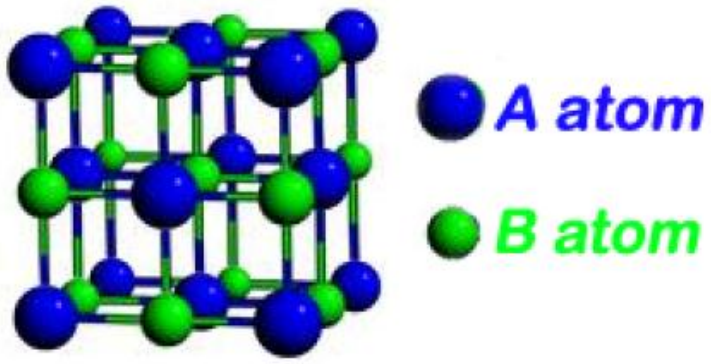

Figure 1.1. Crystal structure of B1 materials

NbN is the only one B1 simple compound that has widely tested for accelerating cavities, because of its high critical temperature of 17.2 K. Mainly two different techniques have been investigated: Thermal diffusion of N into Nb followed by rapid quench cooling and Reactive Sputtering onto Nb cavities. Unfortunately even if no grain boundaries are present and a δ-phase single crystal is considered, the single grain resistivity is not so low: A minimum value of 30 μΩ/cm is expected, due to both metallic and gaseous vacancies in the lattice. This problem that is common to all the other B1 compounds consists in the fact that what corresponds to the equiatomic composition is not the formula Nb1.0N1.0, but Nb0.987N0.987: vacancies randomly distributed in both sublattices amounts to 1.3% respectively [9].

NbC could also be used, because of its high Tc of 12K. Stoichiometric NbC is metastable at ambient temperature and in the stable phase only 80% of the carbon site are occupied. A practical method to produce NbC for coating cavities is the reactive sputtering in CH_4 or C_2H_6 atmosphere.

NbTiN presents all the advantages of the NbN; in the meanwhile it shows electrical conduction properties as more metallic as higher the titanium percentages is. Titanium is a good Nitrogen getter and the more Titanium we have the lower lattice vacancies will be. The Nitrogen stoichiometry hence is closer to 1 than for NbN. NbTiN cavities have been sputtered at CERN and at Saclay. The Q0, at zero field is higher than the Q-value of Niobium cavities, but the accelerating field achieved does not overcome the 10 MV/m limit.

2. A-15 materials

2.1 Crystal structure

Compounds with A-15 structure (generally occurring close to the A_3B stoichiometric ratio) were first discovered to be superconducting when Hardy and Hulm [10] found that V_3Si had a transition temperature of 17.1K. In the following year Nb_3Sn was also discovered with a T_c of 18.1K by Matthias [11].

A atoms are transition elements of groups IV, V or VI. B atoms can be non-transition or transition elements (mainly from group VIII) [12]. As shown in Figure 2.1, a typical feature of the A15 structure is that A atoms form orthogonal chains bisecting the faces of the bcc (body centered cubic) unit cell. The distance between A atoms within a chain is the shortest distance between atoms in the A-15 structure and is shorter than that between A atoms belonging to different chains. B atoms occupy the corners and the center of the bcc structure. The transition temperature of most A15 compounds is strongly influenced by the degree of long range crystallographic order (LRO) or linear chain integrity. T_c is usually maximized for compounds in which the B atom is not a transition metal.

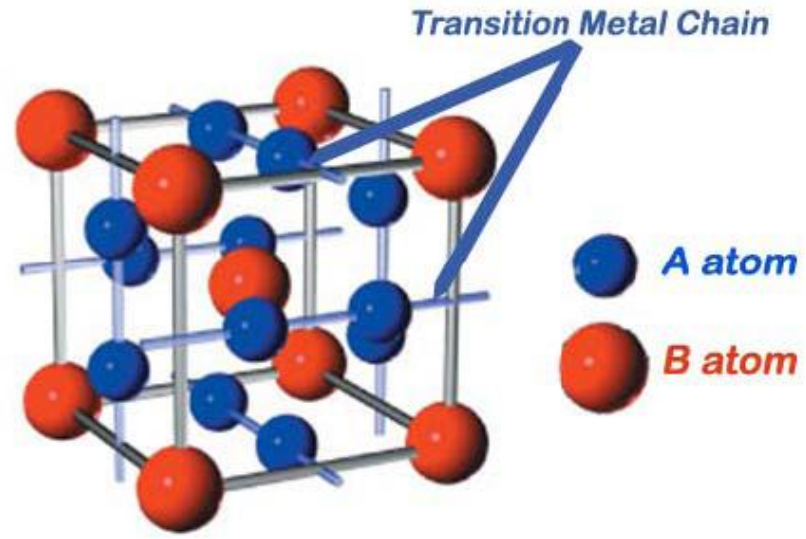

Figure 2.1. Crystal structure of A-15 materials

The stability of the A15 structure is governed more by size considerations than by other atomic or electronic parameters. In this regard it is similar to other topologically close-packed structures. It has a primitive cubic cell of eight atoms, and belongs to the space group O_h^3 −Pm3n. The cubic unit cell has six A atoms at $\frac{1}{4}0\frac{1}{2}$, $\frac{1}{2}\frac{1}{4}0$, $0\frac{1}{2}\frac{1}{4}$, $\frac{3}{4}0\frac{1}{2}$, $\frac{1}{2}\frac{3}{4}0$, $0\frac{1}{2}\frac{3}{4}$; and two B atoms at 000,

$\frac{1}{2}\frac{1}{2}\frac{1}{2}$. The A atoms have a coordination number of 14; the CN14 polyhedron around each A atom contains two A atoms at a distance ½a, four B atoms at distance 5/4a, and eight A atoms at a distance $2r_A = 6/4a$. The B atoms have 12 nearest neighbors (CN12) at a distance $r_A+r_B = 5/4a$. (a is the lattice parameter and r_A and r_B are the atomic radii in this structure of the A and B atoms, respectively.) A conspicuous feature of the A15 structure is the chains of A atoms parallel to the three {100} directions. The interatomic spacing along these chains is 10-15% less than the distance of closest approach in a pure A crystal.

Among the fifty A15 compounds found, the highest critical temperatures (15-20K) are found among Nb and V based compounds, like Nb_3Sn, Nb_3Al, Nb_3Ge, Nb_3Ga, V_3Si. Although they have the highest T_{cs}, Nb_3Ge and Nb_3Ga do not exist as stable bulk materials for the 3:1 stoichiometry. Nb_3Al is stable only at high temperature (1940°C) causing excessive atomic disorder. Moreover, the production of these materials requires non equilibrium processes. On the other hand, Nb_3Sn, V_3Ga, V_3Si are stable bulk materials and have a high T_c. Another A-15 compound of interest is Mo_3Re.

2.2 Critical temperature and compositions

As it was already told above, the T_c of all A-15 materials is strongly influenced by degree of long range order (LRO) and composition. Talking about compounds in which the B atom is not a transition element , T_c is maximized when all the A atoms are on A sites, all the B atoms are on B sites, and the LRO parameter S approaches 1 [13]. The largest effect is seen in V_3Au, in which increasing S from 0.8 to 0.99 increases T_c from 0.7 to 3.2 K. When the B atom is a transition element, the compounds do not have the same sensitivity to ordering.

The critical temperatures of all known superconducting A-15 compounds are listed in Figure 2.2. Only seven of the about fifty superconducting A15 compounds are, on the basis of their high critical temperatures of actual or potential interest [9] . Among them, V_3Si, V_3Ga and Nb_3Sn all have a range of homogeneity that includes the A_3B composition. Maximum T_c is obtainable in bulk samples of this compounds. Nb_3Al and Nb_3Ga include the ideal composition only at temperatures so high that thermal disorder is excessive. Nb_3Ge does not exist in equilibrium at the stoichiometric ratio. Metastable Mo-Re has the highest critical temperature value of even 15 K out of the A_3B stoichiometry, just if grown under thin film form. The metallurgical equilibrium diagrams for the systems containing the foregoing seven phases are given in the following subsections. In the case of V_3Ga and Nb_3Sn, the A15 compound is followed, at increasing B-element concentration, by a series of compounds of much lower melting point. Nb_3Al, Nb_3Ge and Nb_3Ga are all succeeded by a phase σ, 5:3, or 3:2, that is more stable than the A15 phase. It is the presence of this stable phase that prevents the A-15 one from forming at the stoichiometric composition.

The short characteristic of each of the seven materials of interest is given below in the order of reducing T_c.

Nontransition elements	T_c (K)	Transition elements	T_c (K)
Ti_3Sb	6.5	Ti_3Ir	4.2
		Ti_3Pt	0.5
$Zr_{80}Sn_{20}$[a]	0.92		
Zr–Pb	0.76	Zr_3Au	0.9
$Zr_{\sim 3}Bi$[b]	3.4		
		$V_{29}Re_{71}$	8.4
V–Al[c]	14	$V_{70}Os_{30}$	5.7
V_3Ga	15.9	$V_{65}Rh_{35}$	$\simeq 1$
V_3Si	17.0	$V_{63}Ir_{37}$	1.7
$V_{\sim 3}Ge$	6	$V_{\sim 3}Pd$	0.08
$V_{\sim 3}Ge$[c]	11	V_3Pt	3.7
$V_{\sim 79}Sn_{\sim 21}$	3.8	$V_{76}Au_{24}$	3
$V_{77}As_{23}$	0.2	$Nb_{75}Os_{25}$	1.0
$V_{76}Sb_{24}$	0.8	$Nb_{73}Rh_{23}$	2.6
		$Nb_{72}Ir_{28}$	3.2
Nb_3Al	19.1	Nb_3Pt	11
Nb_3Ga	20.7	$Nb_{\sim 3}Au$	11.5
$Nb_{\sim 3}In$[b]	9.2		
$Nb_{82}Si_{18}$[a]	4.4	$Ta_{85}Pt_{15}$	0.4
		$Ta_{\sim 80}Au_{20}$	0.55
Nb–Si[c]	11–17		
Nb–Ge[a]	17	$Cr_{72}Ru_{28}$	3.4
Nb–Ge[c]	23	$Cr_{73}Os_{27}$	4.7
Nb_3Sn	18	$Cr_{78}Rh_{22}$	0.07
Nb–Sb	2	$Cr_{82}Ir_{18}$	0.75
$Nb_{\sim 3}Bi$[b]	3		
		$Mo_{40}Tc_{60}$	13.4
$Ta_{\sim 3}Ge$[c]	8	$Mo_{\sim 65}Re_{\sim 35}$[c]	$\simeq 15$
$Ta_{\sim 3}Sn$	8.3	$Mo_{75}Os_{25}$	13.1
$Ta_{\sim 3}Sb$	0.7	$Mo_{78}Ir_{22}$	8.5
		$Mo_{82}Pt_{18}$	4.6
Mo_3Al	0.58		
Mo_3Ga	0.76	$W_{\sim 60}Re_{\sim 40}$[c]	11
$Mo_{77}Si_{23}$	1.7		
$Mo_{77}Ge_{23}$	1.8		

a Rapid quenching techniques b High-pressure synthesis c Film deposition

Figure 2.2. Critical temperatures of binary A15 compounds known to be superconducting [9].

Nb_3Ge (T_c = 23K):

The most striking feature of Nb_3Ge phase field is that the stoichiometric composition is not included at equilibrium, the highest solubility of Germanium being 23 at.%. At 1000°C, the homogeneity range of the A15 phase is very narrow and is centered at 18 at.% with total width of 1

at.%. It has not been possible to rise T_c above 17÷18 K in bulk sample either by quenching or other means. Metastable stoichiometric, or near stoichiometric, Nb_3Ge can be prepared as thin films with critical temperature of 23 K.

The niobium germanium phase diagram is shown in Figure 2.3 [14].

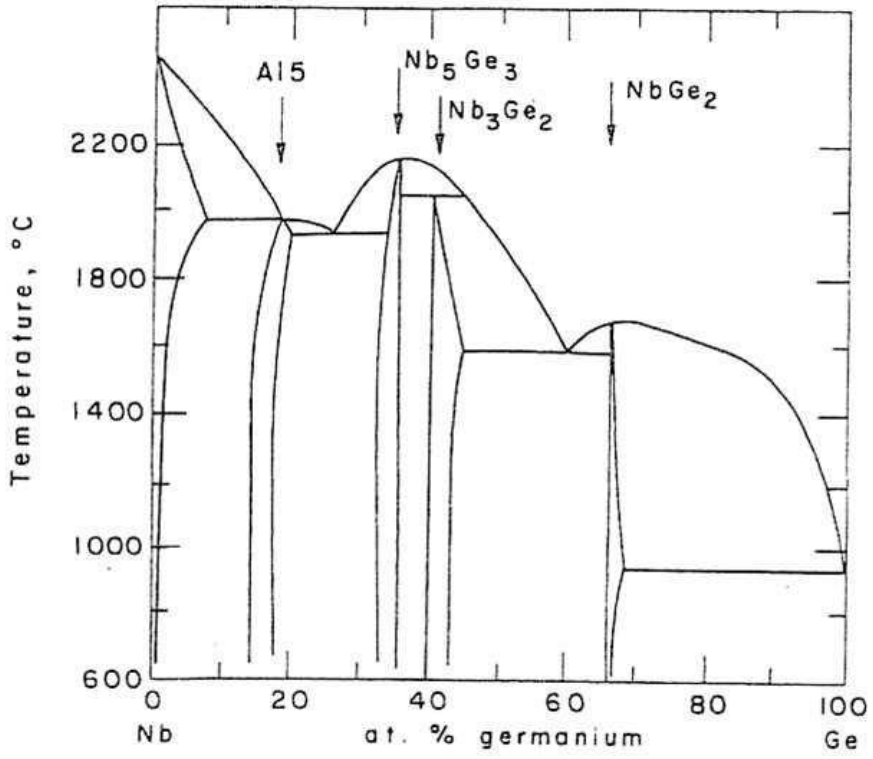

Figure 2.3. The niobium germanium phase diagram

Nb_3Ga (T_c = 20,7K)

The A15 phase forms with 21 at.% Ga, by the peritectic reaction at 1860±C. The stoichiometric composition, 25 at.% Ga, is just attained at 1740±C. Below this temperature the range of homogeneity narrows rapidly and below 1000±C extends from 19.7 to 20.6 at.% Ga. The niobium 25allium phase diagram is shown in Figure 2.4 [15].

The "zoomed" version of the A15 phase field, and the critical temperature of samples corresponding to compositions along the A15-Nb_5Ga_3 phase boundary are shown in Figure 2.5a,b. These vary from 9 K for a specimen corresponding to 20.8 at.% Ga to 18 K for 24.3 at.% Ga. T_c for the latter specimen quenched from 1740±C and subsequently annealed at T < 700±C, which allows an increase in LRO without precipitation of Nb_5Ga_3, was 20.7 K.

Nb_3Al (T_c = 19,1K)

The Nb-Al phase diagram is shown in Figure 2.6. Nb_3Al is formed by a peritectoid reaction from the bcc solid solution and σ-Nb_2Al phase at 1730±C, and contains 26 at.% Al. The A15 phase aluminum content decreases with reducing temperature: the homogeneity range at $1000^{O}C$ is

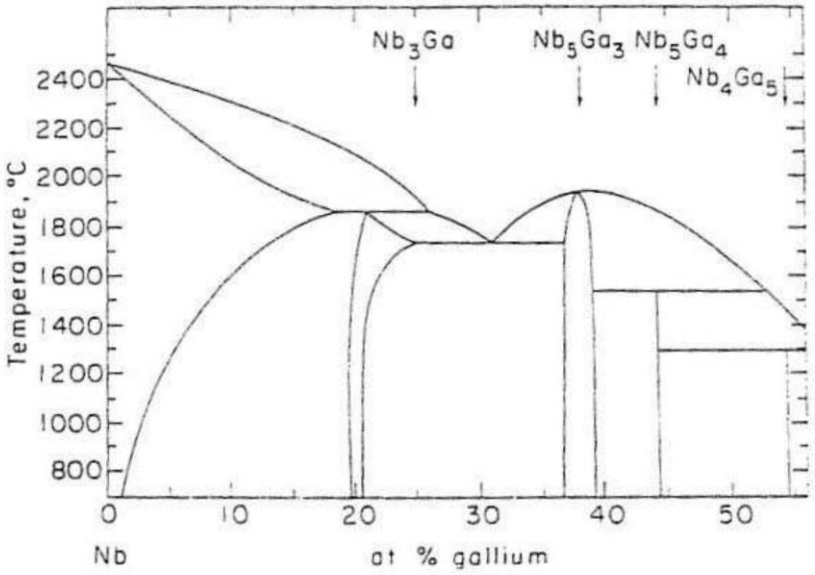

Figure 2.4. Niobium Gallium phase diagram

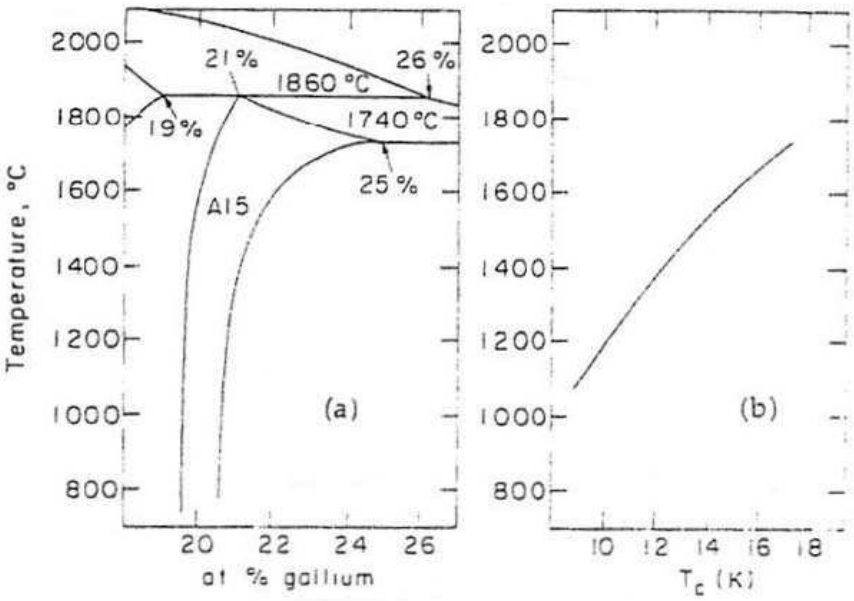

Figure 2.5. (a): The A15 phase field in the Nb-Ga system; (b): the variation of critical temperature T_c with composition along the Ga-rich phase boundary

19-22 at.% Al. The work of Moehlecke [16] has largely confirmed this diagram, though he was able to obtain the A15 phase with a maximum of only 24.5 at.% Al at 1730±C.

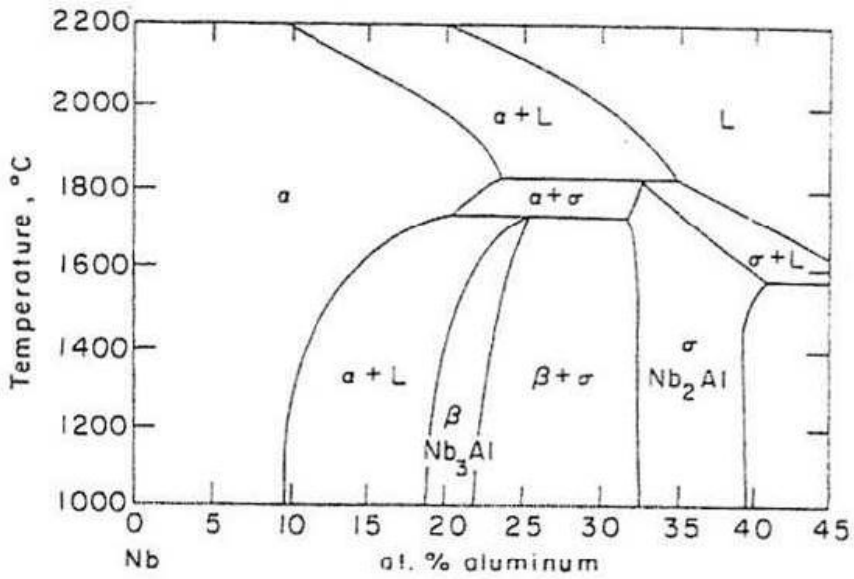

Figure 2.6. Portion of the niobium aluminum phase diagram

Nb_3Sn (T_c = 18K)

Nb_3Sn is one of the best known high field material among the family of A-15 superconductor with a T_c of 18.3 K and is used for the production of intense magnetic field reaching a record value of 21T [17]. The A15 phase for the Nb-Sn intermetallic system is in the composition range of 18 to 25 at.% Sn (see Chapter 4). The superconducting parameters, T_c, Δ, H_{c2}, depend strongly on the Sn content [18]. Close to stoichiometry (24.5at.% Sn) and as a result of perfect ordering in the stoichiometric phase, ρ_n drops below 20μΩcm. Therefore, R_{BCS} for Nb_3Sn has the potential to be much lower and Q – value much higher than for Nb. More extended information about Nb_3Sn see in the chapter 4.

V_3Si (T_c = 17K)

V_3Si is the first of the A-15 discovered with T_c=17K at perfect stoichiometry. This material is one of the few examples of an A-15 compounds that forms normal from the melt. The A15 phase in the Vanadium-Silicon system is stable between 19 and 25 at.% Silicon. Large single crystals can be grown in the whole range either by zone melting or by recrystallization at 1870°C. There is a linear increase in T_c from 19 at. % to 25 at. % silicon, where a maximum T_c of 17.1K is achieved. For this compound, the variation of resistivity in normal state before transition has been studied in detail. Figure 2.7 reports the RRR value versus the Silicon content.

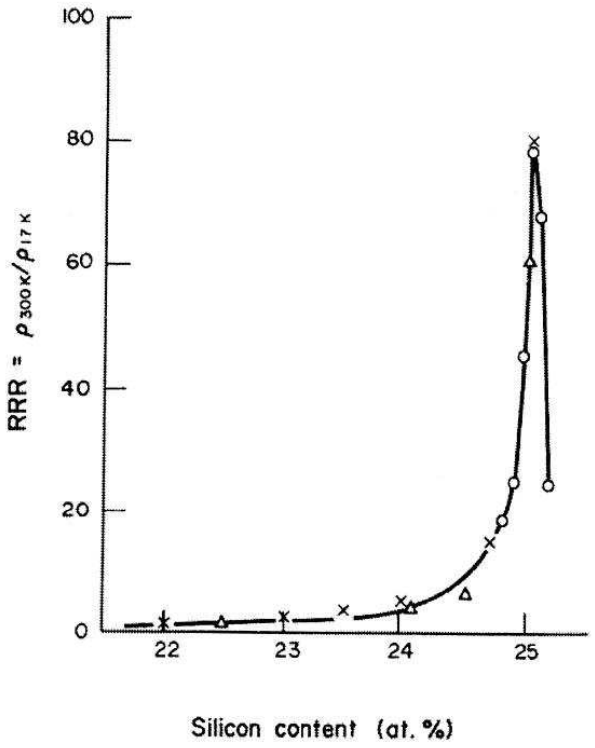

Figure 2.7. V_3Si: RRR values versus silicon content [9]

V_3Ga (T_c = 15,9)

The V_3Ga phase is formed by solid state reaction directly from the bcc solid solution at 1300±C and at a composition corresponding to the stoichiometric formula V_3Ga. The range of homogeneity is a maximum, from 21-31.5 at.% Ga, at 1010±C, and falls to 21-29 at.% Ga at 600±C. This wide range of homogeneity makes V_3Ga an ideal compound for study the effects of composition upon T_c.
Critical temperature has a maximum value at 25 at.% Ga and falls by ~1 K per atomic percent change in composition. V_3Ga has the highest electronic density of states of all known A15 compounds.

Mo – Re (T_c ~ 15K)

Metastable Mo-Re has the highest critical temperature value of even 15 K out of the A_3B stoichiometry, if grown under thin film form. It has been already applied for cavity prototyping [19]. The superconducting critical temperature in bulk bcc $Mo_{100-x}R_x$ rises from 0.92 K for pure molybdenum up to 12 K at x = 40. The solubility of interstitial elements, particularly oxygen, is low in Mo-Re alloys. Moreover, there is indication that such contamination does not depress superconductivity. If compared with other alloys, Mo-Re shows low values of the GL parameter, k, and consequently rather high values of H_{c1} and coherence length. This contributes to decrease the

effect of small inhomogeneities by proximity effect. The highest T_c values have been observed for sputtered films onto substrates held at 1000±C in the composition $Mo_{60}Re_{40}$ and 1200±C in the composition $Mo_{38}Re_{62}$.

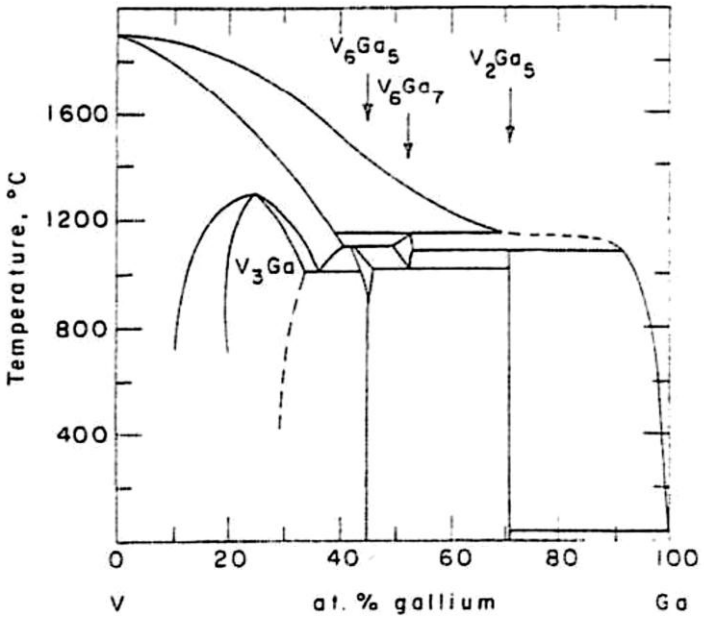

Figure 2.8. V_3Ga: Vanadium gallium phase diagram

3. 6 GHz cavities

3.1 Application

The common limitation of systems conceived for the RF characterization of samples consists in the difficulty of scaling the measured results to the real resonator. In LNL we use 6 GHz cavities (see Figure 3.1) which are completely equal in shape to the real scale model. Performing RF tests on a large amount of cavities it is possible to study alternative thin film superconducting materials, traditional and innovative surface treatments [20,21]. Using 6GHz cavities is possible to perform a high numbers of rf tests reducing research budget. RF measured samples will never be comparable to a real large cavity. It is always an indirect measurement. 6 GHz cavities are at the same time easy to handle like a sample but they are "real" cavities. 6 GHz cavities are made from larger cavities fabrication remaining material using spinning technology (see Figure 3.0), they don't need welding (even for flanges) and finally they can be directly measured inside a liquid helium dewar (see Figure 3.1). While 1,3 – 1,5 GHz cavities need no less than 1 week time preparation for the RF test. With 6 GHz cavities it is possible to perform more than one rf test per day.

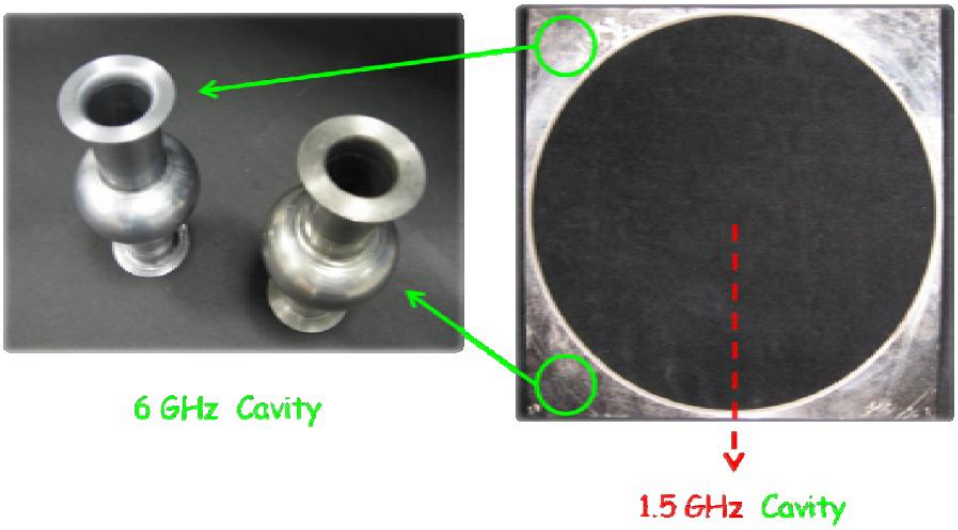

Figure 3.0. On the right the scrap, of a large Nb – cavity, from which is possible to obtain 4 6GHz cavities (on the left) without any welding by spinning technology

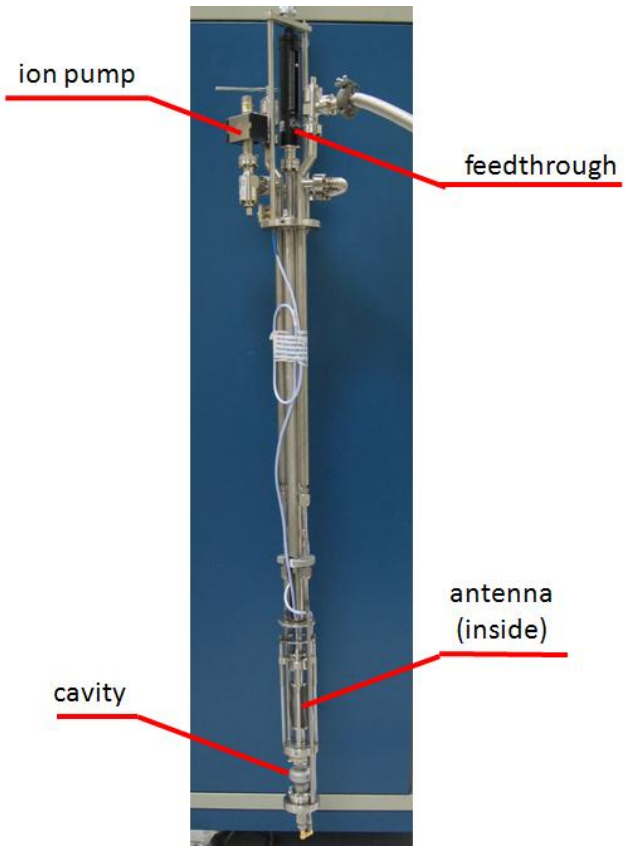

Figure 3.1. Stand for providing rf-test of 6 GHz cavities

3.2 Geometry.

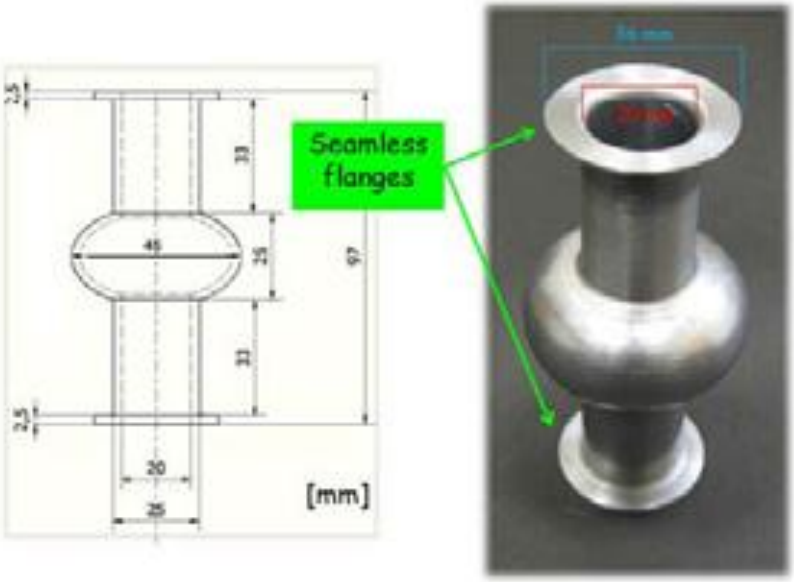

Figure 3.2. The 6 GHz cavity geometry

6 GHz cavities are 97 mm long, have a 45 mm diameter cell, an electrical length of 25 mm and the same shape as a large resonator. It has two large flat flanges at the ends. For each of the flanges available surface is equal to 7 cm^2, in order to ensure the vacuum sealing.

3.3 Fabrication technique

In order to improve the characteristics of the cavity in LNL is used the spinning fabrication technique. This technology has several advantages in comparison with welding one [22]:

- no welding;
- short fabrication time;
- equipment could be adapted for any size of the cavity, and any quantity of cells;
- comparably low fabrication costs;
- no intermediate annealing;
- almost no scraps;

The process of spinning of the 1,5 GHz cavity is depicted on figure 3.3. But it is also used for producing 6 GHz Nb – cavities.

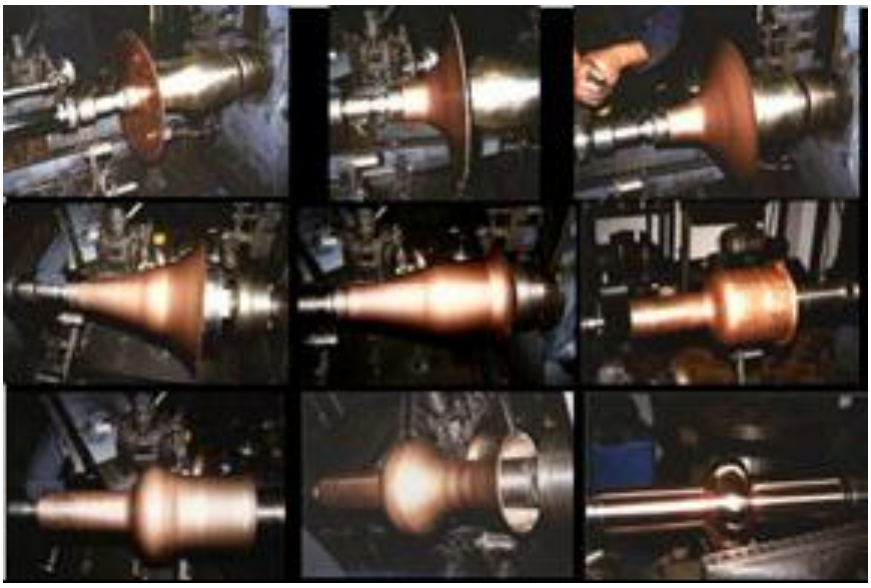

Figure 3.3. Producing of the 1,5 GHz cavity by spinning technology

The process is mainly divided in four steps. A circular disk of 400 mm diameter and 3 mm thickness is first preformed onto a frustum shaped mandrel, then the first half-cell is formed and a

cylindrical shape is given to the remaining part of the piece, by means of a second pre-mandrel. The third step consists in spinning the obtained manufact onto a collapsible mandrel that has exactly the same shape of the cavity interior, up to when the roller overcomes the equator and fixes the piece to spin onto the mandrel. Then the fourth and last step consists in inserting a further frustum-shaped collapsible mandrel in order to guide the material when spinning the second half-cell. Both collapsible mandrels are then removed.

6 GHz Nb cavities, produced by spinning technology are shown on the figure 3.4

Figure 3.4. 6 GHz Nb cavities, produced by spinning technology

4. Nb_3Sn

4.1 Chemical and physical properties

Nb_3Sn or triniobium-tin is a metallic chemical compound of niobium (Nb) and tin (Sn), used industrially as a type II superconductor. This intermetallic compound is a A-15 phases superconductor, and the A15 phase is in the composition range of 18 to 25 at.% Sn. T_c is equal 18 K. The Niobium-Tin phase diagram is shown on the figure 4.0

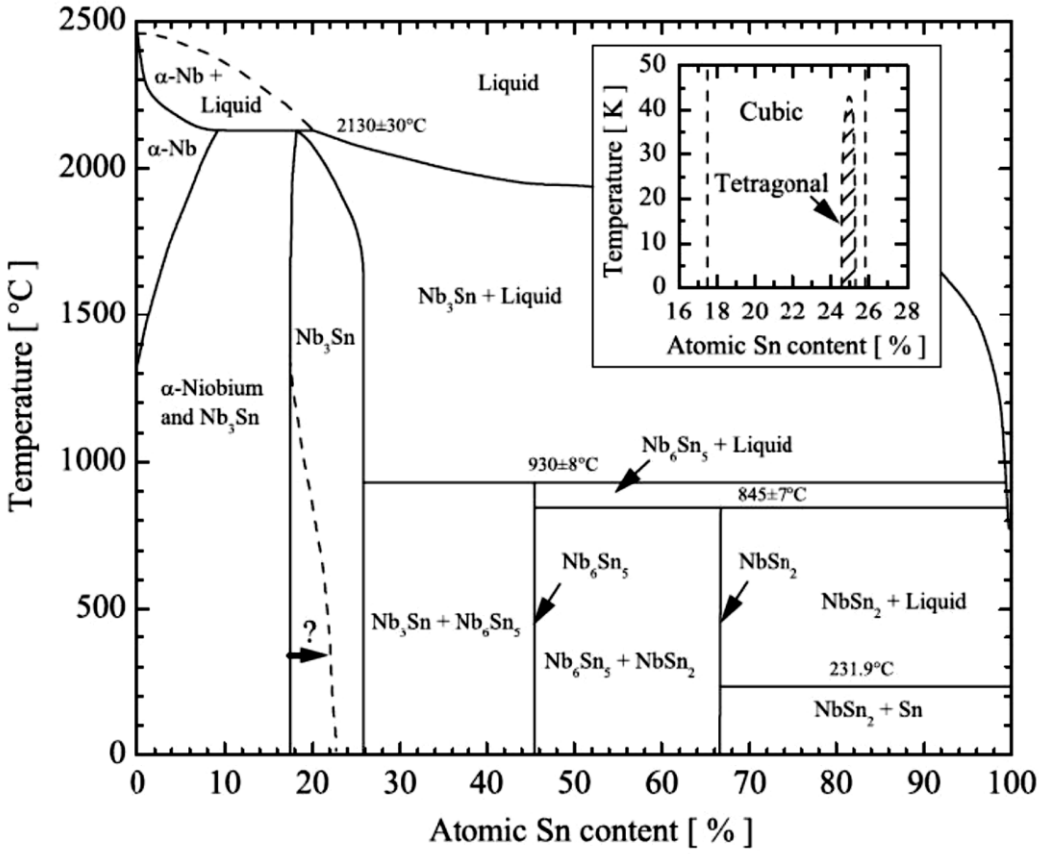

Figure 4.0. Niobium – Tin phase diagram

According the diagram on the figure 4.0, the A15 phase is unstable below 930°C. Also, one can see that there are several spurious phases, and this is a limitation in production of the cavities.

$Nb_{1-\beta}Sn_{\beta}$ exists in the brittle A15 crystal structure with a cubic unit cell, as schematically depicted in Figure 4.1. The Sn atoms form a bcc lattice and each cube face is bisected by orthogonal Nb chains. The importance of these chains is often emphasized to qualitatively understand the generally high critical temperatures of A15 compounds. In bcc Nb the shortest spacing between atoms is about 0.286 nm, starting from a lattice parameter a = 0.330 nm [26]. In the A15 lattice, with a lattice parameter of about 0.529 for the stoichiometric composition [27], the distance between the Nb atoms is about 0.265 nm. That is why A-15 $Nb_{1-\beta}Sn_{\beta}$ has high T_c in comparison to bcc Nb. Variations in T_c are often discussed in terms of long-range crystallographic ordering [28,29,30] since deviations in the Nb chains will affect the DOS peak. The deficiency in the A15 structure causes Sn vacancies, but it is thermodynamically unstable. So the Nb atoms will occupy Sn sites and this affects the continuity of the Nb chains which causes a rounding-off of the DOS peak.

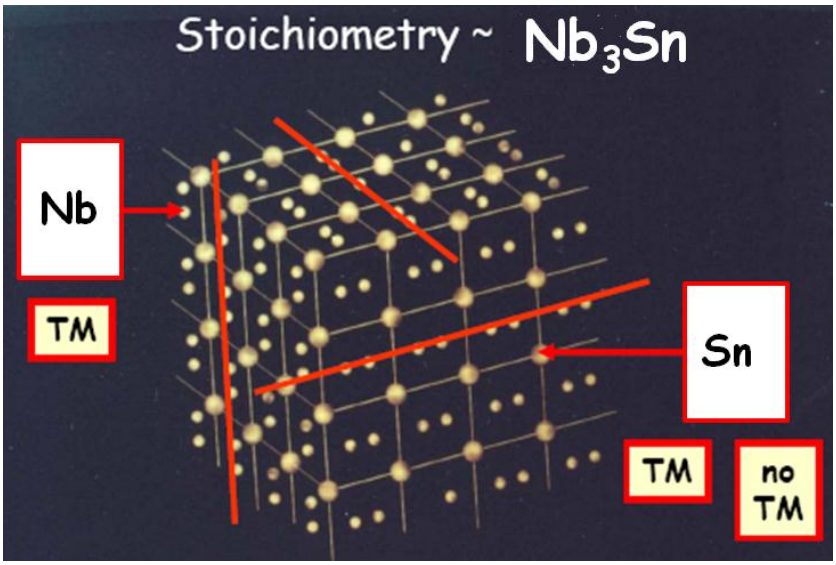

Figure 4.1. Niobium – Tin crystal structure

4.2 T_c as a function of atomic Sn content

Compositional gradients could occur in Nb-Sn samples whatever method is used. That is why it is important to know the variation of the critical temperature with composition. The dependence of T_c as a function of the Sn content is depicted on the figure 4.2 [27].

$$T_c = \frac{-12.3}{1+e^{\frac{\beta-0.22}{0.009}}} + 18.3 \qquad (4.0)$$

Equation 4.0 assumes a maximum T_c of 18.3 K, the highest recorded value for Nb_3Sn

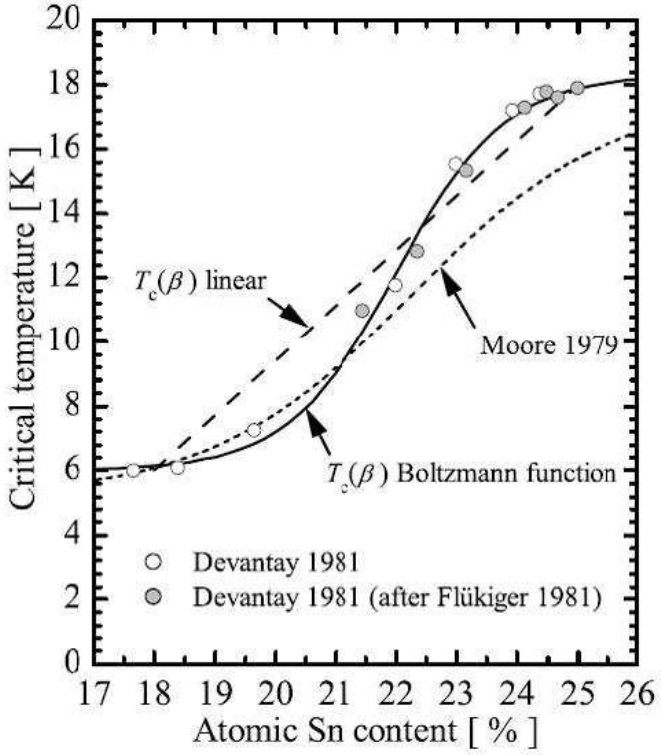

Figure 4.2. T_c as a function of the Sn content

4.3 Nb_3Sn phase formation

The Nb_3Sn phase formation occurs through the diffusion process, which doesn't depend on the matter state. The diffusion can be described through the Fick's Laws. Fick's first law is used in steady-state diffusion, i.e., when the concentration within the diffusion volume does not change with respect to time ($J_{in} = J_{out}$). In one (spatial) dimension, it can be written:

$$J = -D\frac{\partial \phi}{\partial x} \tag{4.1}$$

where:

- J – diffusion flux in dimensions of [$\frac{mol}{m^2 sec}$];
- D – diffusion coefficient or diffusivity in dimensions of [m^2/sec];
- ϕ (for ideal mixtures) – concentration in dimensions of [mol/m^3];
- x – position (length), in dimensions of [m].

D is proportional to the velocity of the diffusing particles, which depends on the temperature, viscosity of the fluid and the size of the particles according to the Stokes – Einstein relation. In two or more dimensions we must use the r operator, which generalizes the first derivative, obtaining

$$J = -D\nabla\emptyset \tag{4.2}$$

The driving force for the one-dimensional diffusion is the quantity $-\frac{\partial\emptyset}{\partial x}$ which (for ideal mixtures) is the concentration gradient. In chemical systems other than ideal solutions or mixtures, the driving force for diffusion of each species is the gradient of chemical potential of this species. Then Fick's first law (one - dimensional case) can be written as:

$$J_i = -\frac{Dc_i}{RT}\frac{\partial\mu_i}{\partial x} \tag{4.3}$$

where:

- i denote the ith species;
- c – concentration (mol/m^3);
- R – universal gas constant [J/(K mol)];
- T – absolute temperature (K);
- μ – chemical potential (J/mol).

Fick's second law is used in non-steady or continually changing state diffusion, i.e. when the concentration within the diffusion volume changes with respect to time.

$$\frac{\partial\emptyset}{\partial t} = D\frac{\partial^2\emptyset}{\partial x^2} \tag{4.4}$$

where:

- ϕ – concentration in dimensions of [mol/m^3];

- t – time [s];
- D – diffusion coefficient in dimensions of [m^2/s];
- x – position, [m].

It can be derived from the Fick's First law and the mass balance:

$$\frac{\partial \emptyset}{\partial t} = -\frac{\partial}{\partial x} J = \frac{\partial}{\partial x}\left(D \frac{\partial}{\partial x} \emptyset\right) \tag{4.5}$$

Assuming the diffusion coefficient D to be a constant we can exchange the orders of the differentiating and multiplying by the constant:

$$\frac{\partial}{\partial x}\left(D \frac{\partial}{\partial x} \emptyset\right) = D \frac{\partial}{\partial x} \frac{\partial}{\partial x} \emptyset = D \frac{\partial^2 \emptyset}{\partial x^2} \tag{4.6}$$

and, thus, receive the form of the Fick's equations as was stated above. For the case of diffusion in two or more dimensions the second Fick's Law is:

$$\frac{\partial \emptyset}{\partial t} = D \nabla^2 \emptyset \tag{4.7}$$

which is analogous to the heat equation. If the diffusion coefficient is not a constant, but depends upon the coordinate and/or concentration, the second Fick's Law becomes:

$$\frac{\partial \emptyset}{\partial t} = \nabla \cdot (D \nabla \emptyset) \tag{4.8}$$

An important example is the case where ϕ is at a steady state, i.e. the concentration does not change by time, so that the left part of the above equation is identically zero. In one dimension with constant D, the solution for the concentration will be a linear change of concentrations along x. In two or more dimensions we obtain:

$$\nabla^2 \emptyset = 0 \tag{4.9}$$

which is Laplace's equation..

The diffusion coefficient at different temperatures is often found to be well predicted by

$$D = D_0 \cdot e^{-\frac{E_A}{RT}} \tag{4.10}$$

where:

- D – diffusion coefficient;
- D_0 – maximum diffusion coefficient (at infinite temperature);
- E_A – activation energy for diffusion;
- T – temperature in units of kelvins;
- R – gas constant.

An equation having this form is known as the Arrhenius equation. The laws described above normally apply to the ideal case of two interdiffusing solid species, but in a real situation, we need to consider the defects role.

Liquid tin diffusion occurs in two distinct steps: the initial simple bulk diffusion and a second stage characterized by the grain boundary diffusion influence on the growth kinetics. After the Nb_3Sn nucleation, crystallites grow up. The time dependence of the thickness follows a $t^{0,5}$ low until the film forms a barrier slowing down the diffusion process. The proposed mechanism is the intermetallic compound solution – dissolution [126]: this means equilibrium establishing between Sn diffusing (promoting the layer growing) and the one dissolving back to the liquid.

As one can see from the Nb-Sn phase diagram, the A15 phase stability is guaranteed above 930±C. At a lower temperature the possibility to obtain the formation of spurious phases becomes concrete.

5. Inductive heating fundamentals

5.1 Introduction

Induction heating is the process of non – contact heating an electrically conducting object (in our case – 6 GHz superconductive cavity) by electromagnetic induction, where eddy currents are generated within the metal and resistance leads to Joule heating of the metal. An induction heater consists of an electromagnet, through which a high-frequency alternating current (AC) is passed. Heat may also be generated by magnetic hysteresis losses in materials that have significant relative permeability. The frequency of AC used depends on the object size, material type, coupling (between the work coil and the object to be heated) and the penetration depth.

Since it is non-contact, the heating process does not contaminate the material being heated. It is also very efficient since the heat is actually generated inside the cavity. This can be contrasted with other heating methods where heat is generated in a flame or heating element, which is then applied to the workpiece. For these reasons Induction Heating lends itself to some unique applications in science, industry and SRF science in particular.

5.2 Magnetic material properties

Each electron in an atom has a net magnetic moment due to the orbiting and spin. Orbiting related to the motion of the electron around its nucleus. The orbiting motion of the electron gives rise to a current loop, generating a very small magnetic field with its moment through its axis of rotation. Spin can either be in positive (up) direction or in negative (down) direction. Thus each electron in an atom has a small permanent orbital and spin magnetic moment.

When an external magnetic field H is applied, the magnetic moment in the material tends to become aligned with this field, resulting in a magnetization of the solid. Assuming a linear relation between the magnetization vector and the magnetic field makes it possible to write [31, 32]

$$M = \chi_m H + M_0 \tag{5.0}$$

where

- χ_m – dimensionless quantity called the magnetic susceptibility (a measure of how sensitive a material is to a magnetic field);

- M_0 – is a fixed vector that bears no functional relationship to H and is referred to the state of permanent magnetization.

The magnetic flux density and the magnetic field are related to each other according to

$$B = \mu_0(H + M) \tag{5.1}$$

Combining Eq. (5.0) and (5.1) gives

$$B = \mu_0(1 + \chi_m)H + \mu_0 M_0 = \mu_0\mu_r H + \mu_0 M_0 = \mu H + \mu_0 M_0 \tag{5.2}$$

where

- μ – permeability of the material
- μ_r – relative permeability, which is given by the permeability of a material over μ_0.

5.2.1 Different kinds of magnetic materials

For some solid materials, the atoms have a permanent dipole moment due to incomplete cancellation of the electron spin and/or orbital magnetic moments. However, due to the thermal agitation, the atoms are randomly oriented and result in zero net magnetic moment of the solid. Applying an external field on such material the atoms start to align, resulting in a small positive susceptibility usually in the order of 10^{-5} to 10^{-2}. Aluminum, Titanium and Niobium are examples of paramagnetic materials. Due their low relative permeability, μ_r, paramagnetic materials are all treated as nonmagnetic. On the figure 5.1 (a) is depicted the orientation of magnetic moments in a different kinds of materials.

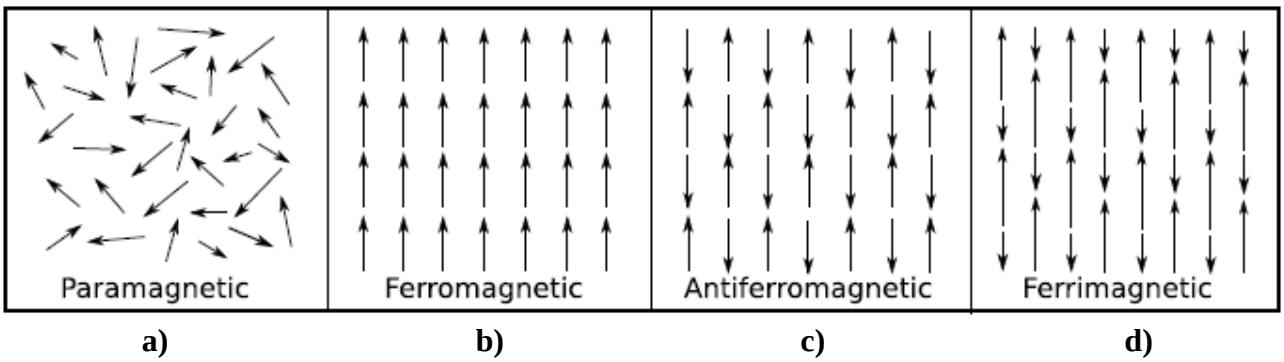

Figure 5.1. Schematic illustration of the alignment of magnetic moments for different types of materials

Ferromagnetic materials have a permanent magnetization even in the absence of a magnetic field, and is due to the same net atomic magnetic moment as in paramagnetism i.e. electron spins that do not cancel.

The magnetic moment of an atom in a antiferromagnetic material are antiparallel to the neighboring atoms, resulting in zero net magnetization. Nickel oxide (NiO), manganese oxide (MnO) and iron manganese alloy (FeMn) are examples of this material group. A material that possess such magnetic properties react as if they were paramagnetic.

5.2.2 Domains

A magnetic domain is a region where the individual magnetic moments of the atoms are aligned with each another. A ferromagnetic or ferrimagnetic material is composed of several domains, individually changing their alignment. In a polycrystalline specimen the domains do not correspond with the grain in the material as each grain can consist of more than a single domain. The magnitude of the magnetization, for the entire solid is therefore the vector sum of the magnetization for all the domains. In a permanent magnet, the domains stays aligned and the vector sum is non-zero even in the absence of a magnetic field. Materials that obsess this possibility is called hard magnetic material. On the other hand, soft magnetic materials are materials that lose their memory of previous magnetization and can therefore not be a permanent magnetic.

5.2.3 Hysteresis

When a ferromagnetic or ferrimagnetic material is exposed to an externally applied magnetic field H, the relationship to the magnetic flux density B may not be linear as in Eq. (5.2). A typical hysteresis curve showing a non-linear relation between B and H and is shown on the figure 5.2. Initially, domains in the unmagnetized specimen are in different directions. When an external magnetic field are applied on the specimen, the domains start to line up in the same direction as the applied magnetic field (figure 5.2 (a), line 1). This orientation process will continue until the saturation point B_s is reached and all domains are lined up. After this point there is a linear relation between changes in the magnetic flux and the magnetic field. When the magnetic field is reduced, it will not follow the initial curve but lags behind (figure 5.2 (a), line 2). This phenomena is called the hysteresis. Whenever the magnetic field is zero, B is not reduced to zero but to B_r. This point is called the remanence, or remanent flux density; the material remains magnetized in the absence of an external field. To reduce the magnetic flux in the specimen to zero, a magnetic field of the magnitude H_c in the opposite direction (to the original one) must be applied (figure 5.2 (b)). H_c is called the coercive force. The size and shape of the hysteresis curve is of practical importance. The area within a loop is the energy loss per magnetization cycle which appear as heat that is generated within the body.

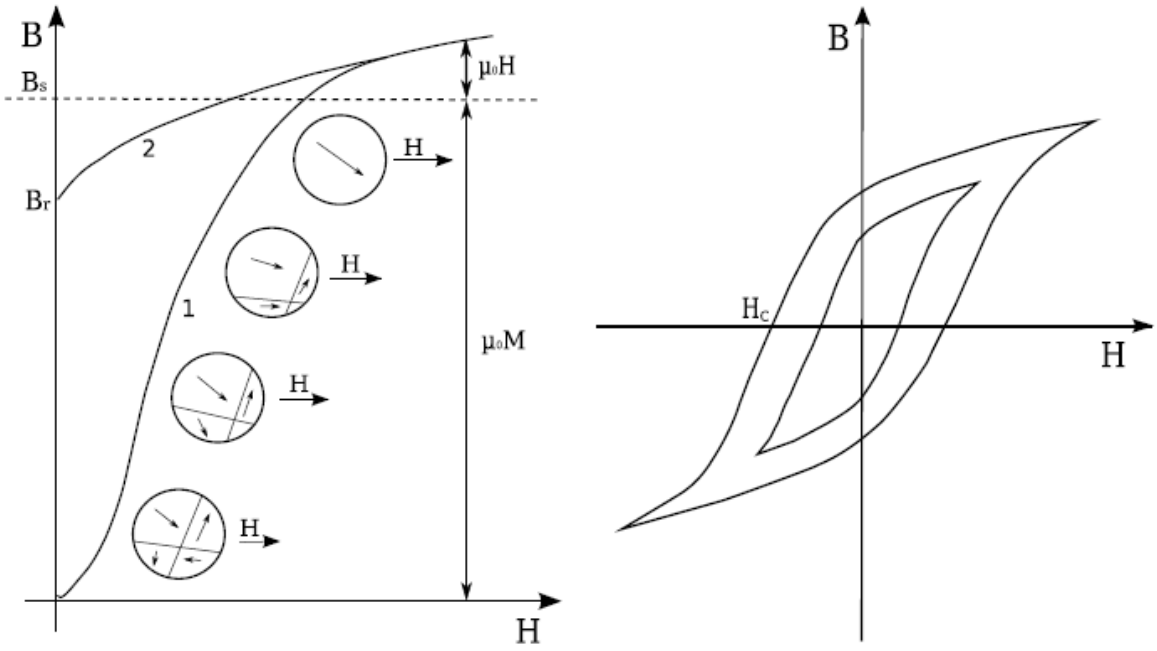

Figure 5.2. Hysteresis curves. A virgin hysteresis curve (a) and a full hysteresis curve (b)

5.2.4 Skin depth

At high frequency eddy currents are extruded by magnetic field to the surface layers of the specimen. This is what is called skin – effect. As the result of this extrusion, current density increases and according to the Joule's law the specimen heats. The deeper layers of the specimen are heated due to its thermal conductivity. In the skin layer δ current density decreases exponentially to the current density on the surface of the specimen and 85% of heat (relatively to all accumulated heat) releases in the skin layer. The depth of the skin layer depends on frequency and magnetic permeability of the metal.

One can calculate the depth of skin layer using next formula:

$$\delta = \frac{1}{\sqrt{\pi \mu_0}} \sqrt{\frac{\rho}{\mu_r f}} \approx 503 \sqrt{\frac{\rho}{\mu_r f}} \tag{5.3}$$

where:

- δ = the skin depth in meters;
- $\mu_0 = 4\pi \times 10^{-7}$ H/m;
- μ_r = the relative permeability of the medium;
- ρ = the resistivity of the medium in Ω·m (for Sn = $11{,}5 \times 10^{-8}$ Ω·m);
- f = the frequency of the wave in Hz.

5.3 Practical implementation of induction heating system

In theory only three things are essential to implement induction heating:

1. A source of High Frequency electrical power;
2. A work coil to generate the alternating magnetic field;
3. An electrically conductive workpiece to be heated.

Having said this, practical induction heating systems are usually a little more complex. For example, an impedance matching network is often required between the High Frequency source and the work coil in order to ensure good power transfer. Water cooling systems are also common in high power induction heaters to remove waste heat from the work coil, its matching network and the power electronics. Finally some control electronics is usually employed to control the intensity of the heating action, and time the heating cycle to ensure consistent results. The control electronics also protects the system from being damaged by a number of adverse operating conditions.

In practice the work coil is usually incorporated into a resonant tank circuit. This has a number of advantages. As first, it makes either the current or the voltage waveform become sinusoidal. This minimizes losses in the inverter (which is driving high power and will be described below) by allowing it to benefit from either zero-voltage-switching or zero-current-switching depending on the exact arrangement chosen. The sinusoidal waveform at the work coil also represents a more pure signal and causes less Radio Frequency Interference to nearby equipment.

5.3.1 Parallel resonant tank circuit

The work coil is made to resonate at the particular operating frequency by means of a capacitor placed in parallel with it (see figure 5.3). This causes the current through the work coil to be sinusoidal. The parallel resonance also magnifies the current through the work coil, much higher than the output current capability of the inverter. The inverter “sees” a sinusoidal load current. However, in this case it only has to carry the part of the load current that actually does real work. The inverter does not have to carry the full circulating current in the work coil. This property of the parallel resonant circuit can make a ten times reduction in the current that must be supported by the inverter and the wires connecting it to the work coil. Conduction losses are typically proportional to current squared, so a ten times reduction in load current represents a significant saving in conduction losses in the inverter and associated wiring. This means that the work coil can be placed at a location remote from the inverter without big losses in the wires.

Work coils using this technique often consist of only a few turns of a thick copper conductor but with large currents of many hundreds or thousands of amps flowing. (This is necessary to get the required Ampere turns to do the induction heating.) Water cooling is common for all but the

smallest of systems. This is needed to remove excess heat generated by the passage of the large high frequency current through the work coil and its associated tank capacitor.

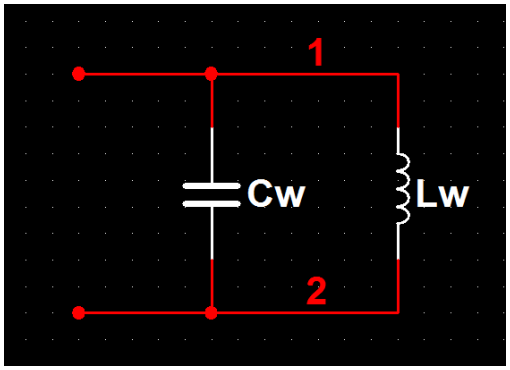

Figure 5.3. Parallel resonant tank circuit. 1,2 – different values of current

In the parallel resonant tank circuit the work coil can be thought of as an inductive load with a "power factor correction" capacitor connected across it. The PFC capacitor provides reactive current flow equal and opposite to the large inductive current drawn by the work coil. The key thing is that this huge current is localised to the work coil and its capacitor. Therefore the only real current flow from the inverter is the relatively small amount required to overcome losses in the "PFC" capacitor and the work coil. There is always some loss in this tank circuit due to dielectric loss in the capacitor and skin effect causing resistive losses in the capacitor and work coil. That's why a small current is always drawn from the inverter even with no workpiece present. When a workpiece is inserted into the work coil, this damps the parallel resonant circuit by introducing a further loss into the system. Therefore the current drawn by the parallel resonant tank circuit increases when a workpiece is entered into the coil.

5.3.2 Impedance matching

This refers to the electronics that is between the inverter and the work coil. In order to heat a solid piece of metal via induction heating we need to cause a tremendous current to flow in the surface of the metal. However this can be contrasted with the inverter that generates the high frequency power. The inverter generally works better if it operates at fairly high voltage but a low current. Increasing the voltage and decreasing the current allows common switch mode MOSFET or IGBT transistors to be used. It is the job of the matching network and the work coil itself to transform the high-voltage/low-current from the inverter to the low-voltage/high-current required to heat the workpiece efficiently.

A parallel resonant circuit, which consists of the work coil (L_w) and its capacitor (C_w) has a resistance due to the magnetic coupling between coil and the workpiece. In practice the resistance of the work coil, the resistance of the tank capacitor, and the reflected resistance of the workpiece all introduce a loss into the tank circuit and damp the resonance. Therefore it is useful to combine all of these losses into a single "loss resistance".

When driven at resonance the current drawn by the tank capacitor and the work coil are equal in magnitude and opposite in phase and therefore cancel each other out as far as the source of power is concerned. This means that the only load seen by the power source at the resonant frequency is the loss resistance across the tank circuit. The job of the matching network is simply to transform this relatively large loss resistance across the tank circuit down to a lower value that better suits the inverter attempting to drive it. There are many different ways to achieve this impedance transformation including tapping the work coil, using a ferrite transformer, a capacitive divider in place of the tank capacitor, or a matching circuit such as an L-match network.

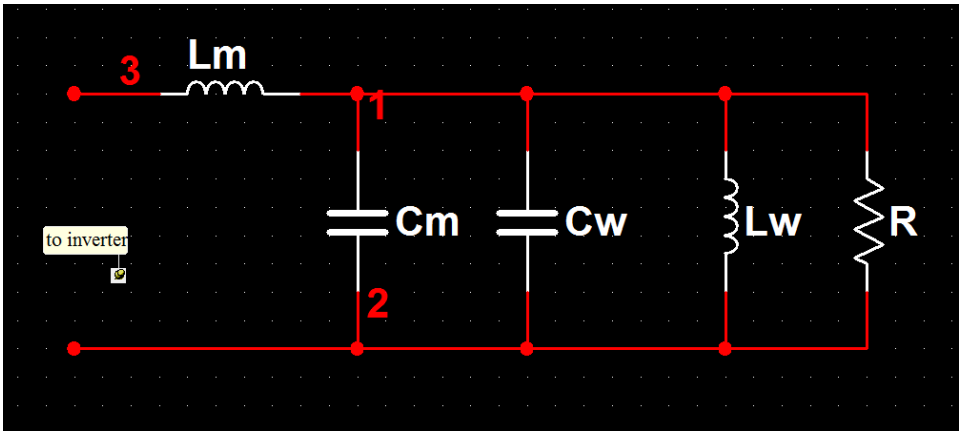

Figure 5.4. The L – matching network

The L-match network (see figure 5.4) consists of inductance L_m and capacity C_m. The inductor at the input to the L-match network presents a progressively rising inductive reactance to all frequencies higher than the resonant frequency of the tank circuit. This is very important when the work coil is powered by a voltage-source inverter that generates a squarewave voltage output. It is so, because the squarewave voltage generated by inverter circuit is rich in high frequency harmonics as well as the wanted fundamental frequency. Direct connection of such a voltage source to a parallel resonant circuit would cause excessive currents to flow at all harmonics of the drive frequency. This is because the tank capacitor in the parallel resonant circuit would present a progressively lower capacitive reactance to increasing frequencies. This is potentially very damaging to a voltage-source inverter. It results in large current spikes at the switching transitions as the inverter tries to rapidly charge and discharge the tank capacitor on rising and falling edges of the squarewave. The inclusion of the L-match network between the inverter and the tank circuit negates this problem. Now the output of the inverter sees the inductive reactance of L_m in the matching network first, and all harmonics of the drive waveform see a gradually rising inductive impedance. This means that maximum current flows at the intended frequency only and little harmonic current flows, making the inverter load current into a smooth waveform.

In summary, the inclusion of an L-match network between the inverter and the parallel resonant tank circuit achieves two things:

- impedance matching so that the required amount of power can be supplied from the inverter to the workpiece;

- presentation of a rising inductive reactance to high frequency harmonics to keep the inverter safe.

Looking at the previous schematic above we can see that the capacitor in the matching network C_m and the tank capacitor C_w are both in parallel. In practice both of these functions are usually accomplished by a single purpose built power capacitor (figure 5.5). Combing these two capacitances into one leads us to arrive at the LCLR model for the work coil arrangement, which is commonly used in industry for induction heating.

5.3.3 LCLR work coil

The LCLR work coil has a number of desirable properties:

- a huge current flows in the work coil, but the inverter only has to supply a low current;
- only comparatively low current flows along the transmission line from the inverter to the tank circuit, so this can use "light" cable;
- any stray inductance of the transmission line simply becomes part of the matching network inductance L_m. Therefore the heat station can be located away from the inverter;
- the series matching inductor can be altered to dial with different loads placed inside the work coil;
- the power to tank circuit can be supplied by several matching inductors from many inverters to reach power levels above those achievable with a single inverter. The matching inductors provide inherent sharing of the load current between the inverters and also make the system tolerant to some mismatching in the switching instants of the paralleled inverters.

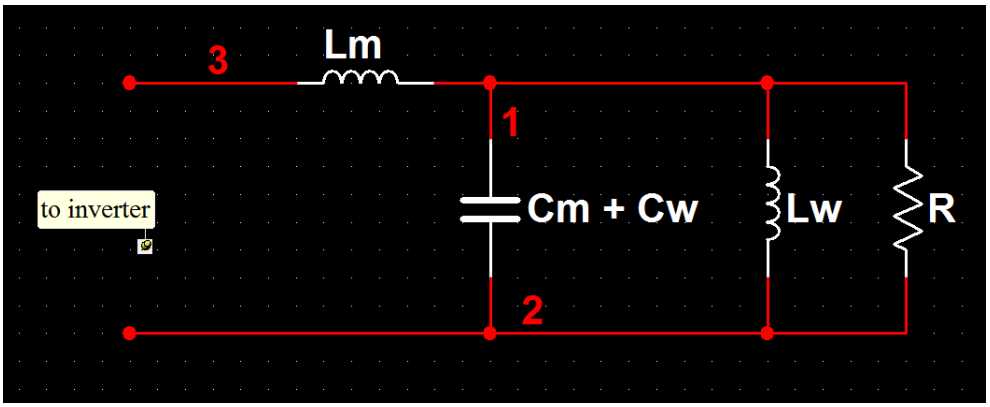

Figure 5.5. The LCLR work coil

Another advantage of the LCLR work coil arrangement is that it does not require a high-frequency transformer to provide the impedance matching function. Ferrite transformers capable of

handling several kilowatts are large, heavy and quite expensive. In addition to this, the transformer must be cooled to remove excess heat generated by the high currents flowing in its conductors. The incorporation of the L-match network into the LCLR work coil arrangement removes the necessity of a transformer to match the inverter to the work coil, saving cost and simplifying the design.

5.3.4 Conceptual schematic

The system schematic shown on the figure 5.6 is the simplest inverter driving its LCLR work coil arrangement. This schematic doesn't show the MOSFET gate-drive circuitry and control electronics.

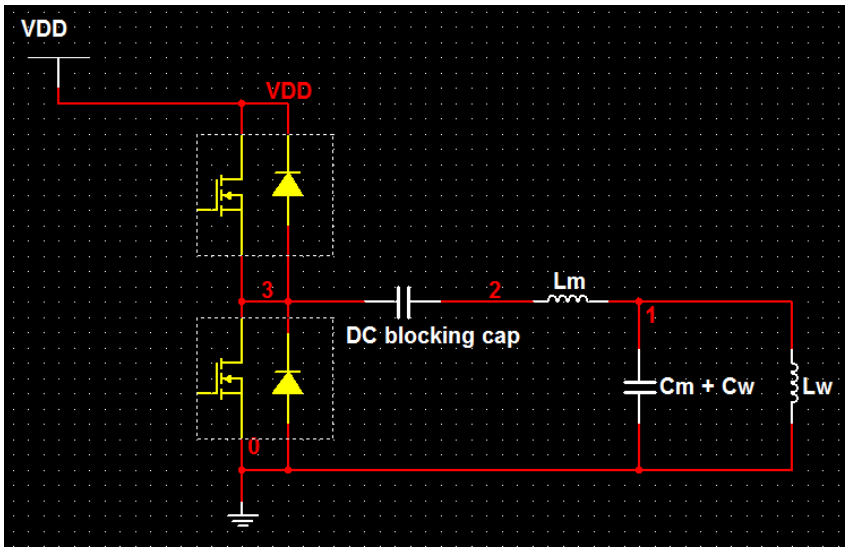

Figure 5.6. Half bridge induction heater using LCLR – work coil

The inverter in this demonstration prototype is a simple half-bridge consisting of two MOSFET transistors. The power is supplied from a smoothed DC supply. The DC-blocking capacitor is used merely to stop the DC output from the half-bridge inverter from causing current flow through the work coil. It is sized sufficiently large that it does not take part in the impedance matching, and does not influence the operation of the LCLR work coil arrangement.

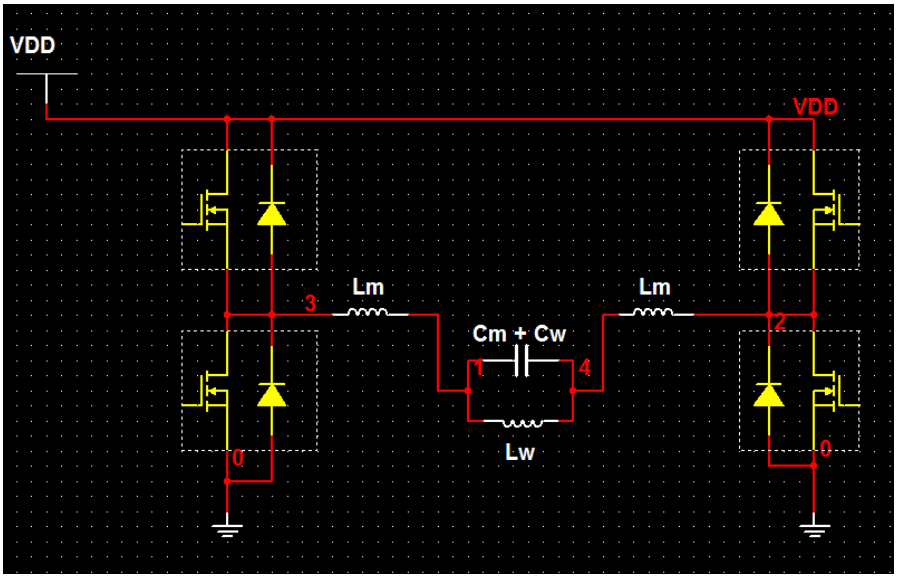

Figure 5.7. Full bridge induction heater using LCLR – work coil

In high power designs it is common to use a full-bridge of 4 or more switching devices. In such designs the matching inductance is usually divided equally between the two bridge legs so that the drive voltage waveforms are balanced with respect to ground. The DC-blocking capacitor can also be eliminated if current mode control is used to ensure that no net DC flows between the bridge legs. The system schematic of the full-bridge switching device is shown on the figure 5.7.

5.3.5 Fault tolerance

The LCLR work coil arrangement is very well behaved under a variety of possible fault conditions.

- open circuit work coil;
- short circuit work coil or tank capacitor;
- shorted turn in work coil;
- open circuit tank capacitor.

All of these failures results increase in the impedance presented to the inverter and therefore a corresponding drop in the current drawn from the inverter.

5.3.6 Power control methods

It is often desirable to control the amount of power processed by an induction heater. This determines the rate at which heat energy is transferred to the workpiece. The power can be

controlled in a number of different ways. In this work we'll not go dipply into the electronic part of power control methods, because it is out of topic, but just represent a list of possible ways:

- varying the DC link voltage;
- varying the duty ratio of the devices in the inverter;
- varying the operating frequency of the inverter;
- varying the value of the inductor in the matching network;
- impedance matching transformer;
- phase-shift control of H-bridge.

6. Nb_3Sn by «double furnace» Liquid Tin Diffusion fabrication technique

6.1 Introduction

The base idea of the liquid tin diffusion method is introducing the Niobium substrate into a molten Sn bath and in its subsequent annealing. Method has some advantages in comparison with other fabrication techniques, such as, for example Tin vapor diffusion or sputtering. This advantages are:

- LTD is a relatively cheap technique (considering the goal is to coat a large number of cavities, this technique is probably the less expensive one: it employs a low technology equipment and it is quite fast);
- uniformity of the film (stoichiometrically);
- can be used for covering surface of wide and complex shaped substrates (!).
- we don't need to manipulate dangerous substances as $SnCl_2$ to create a nucleation centers, and the diffusion process is considerably faster

6.2 Nb_3Sn samples fabrication

6.2.1 L-samples

In order to reduce the cost of experiments the L-samples were designed. Samples are made of Niobium (RRR = 300), has 50 mm long, 20 mm wide and imitates the shape of the cavity as it shown in the figure 6.0. Each sample has its own number, made by extrusion.

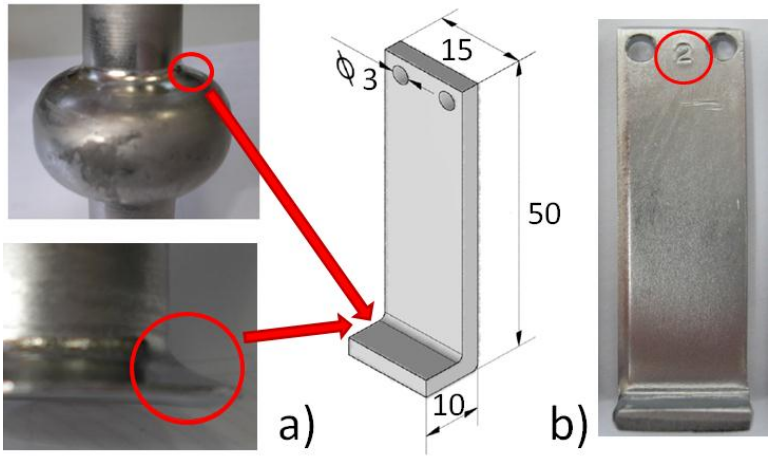

Figure 6.0. Shape of L-sample (a), and number of the sample (b)

6.2.2 Preliminary surface treatments (mechanical treatment and BCP)

Mechanical treatment

In order to remove scratches caused by Nb-sheets manufacturing, samples have been grinded using different particle sizing SiC abrasive papers. The idea is to have the same starting surface for the chemical polishing. Typically the chosen sequence begins with a 600 grained paper and finish with a soft cloth to remove the possible residual particulate. During the process, a water flow is continuously refreshing the substrates to avoid their worming up. At the end of the described mechanical treatment, the Nb pieces were washed in ultrasonic with Rodaclean for 60 minutes, cleaned with acetone and alcohol and after dried.

Chemical treatment

Following the classical surface treatments after the mechanical polishing the procedure counts a chemical polishing. Chemical treatments are performed to smooth further on the sample surface, to remove the possible niobium oxides and contaminants. The used solution is the acid mixture containing HF 40%, HNO_3 65% and H_3PO_4 85% (standard Buffered Chemical Polishing, BCP 1:1:2). Nitric acid plays the niobium surface oxidizing role. Hydrofluoric acid reduces the niobium pentaoxide into a salt that is soluble in water. Phosphoric acid acts as a moderator for the chemical reaction giving rise to a less turbulent and more controllable reaction (see Equations 6.0, 6.1 and 6.2).

The examples of the samples treated with and without BCP is shown on the figure 6.1

Figure 6.1. L-samples with and without BCP

$$6Nb_{(s)} + 10HNO_{3(aq)} \rightarrow 3Nb_2O_{5(s)} + 10NO_{(gas)} + 5H_2O_{(l)} \quad (6.0)$$

$$Nb_2O_{5(s)} + 6HF_{(aq)} \rightarrow H_2NbOF_{5(aq)} + NbO_2F_{(s)} \cdot \frac{1}{2}H_2O + \frac{3}{2}H_2O_{(l)} \quad (6.1)$$

$$NbO_2F_{(s)} \cdot \frac{1}{2}H_2O + 4HF_{(aq)} \rightarrow H_2NbOF_{5(aq)} + \frac{3}{2}H_2O_{(l)} \quad (6.2)$$

6.2.3 Glow Discharge

Part of the samples, in order to increase cleanness of the surface were treated with use of vacuum plasma discharge in the glow regime. The goal was to obtain extremely clean surface in order to improve diffusion of Tin into Niobium and reduce the residual Tin droplets (see chapter 5.3.8).

The glow discharge was provided in the stainless steel UHV chamber in the top of which was connected the transmitting CF-100 – CF-36 (see figure 6.2a). To the CF-36 was connected flange with the copper feedthrough, to which the sample connects by meaning of Niobium wire. The flange with the sample is depicted on the figure 6.2b. In the bottom of the chamber is connected the window-flange, in order to visually control the discharge process and having possibility to take the pictures of the process.

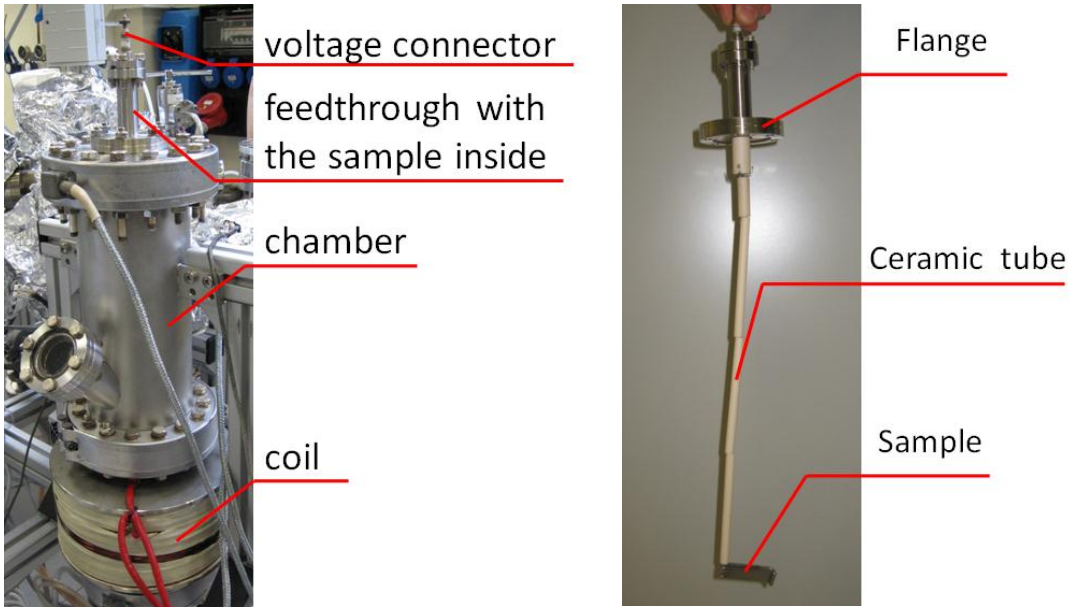

Figure 6.2. The glow discharge chamber (a) and the feedthrough with L-sample connected

Niobium-wire feedthrough was insulated by the ceramic tubes, in order to prevent discharge of the wire. With the aim of uniform discharge of all of the sample planes we fixed it in a horizontal position, otherwise (in vertical position) the magnetic field is perpendicular to the bended part of the sample and this plane doesn't discharge.

The pumping unit is made of a rotary TriScroll (12.6 m^3/h) pump and a turbomolecular pump (70 l/s), and has a pneumatic gauge, mount in the inlet of turbomolecular pump for preventing damage of the pump while venting and opening the chamber and a whole-metal valve for disconnecting the chamber from the main chamber (i.e. glow discharge camber is a part of the system, contain of four chambers). Also there are the argon inlet, controlled by a leak valve for regulating the process pressure in the chamber, controlled by a leak valve, and the nitrogen inlet for venting the chamber, controlled by a leak valve.

The magnetic field was provided by means of the external coil, connected to tension-stabilized source. Relationship between the current, flowing through the coil and inducted magnetic field is shown on the figure 6.3

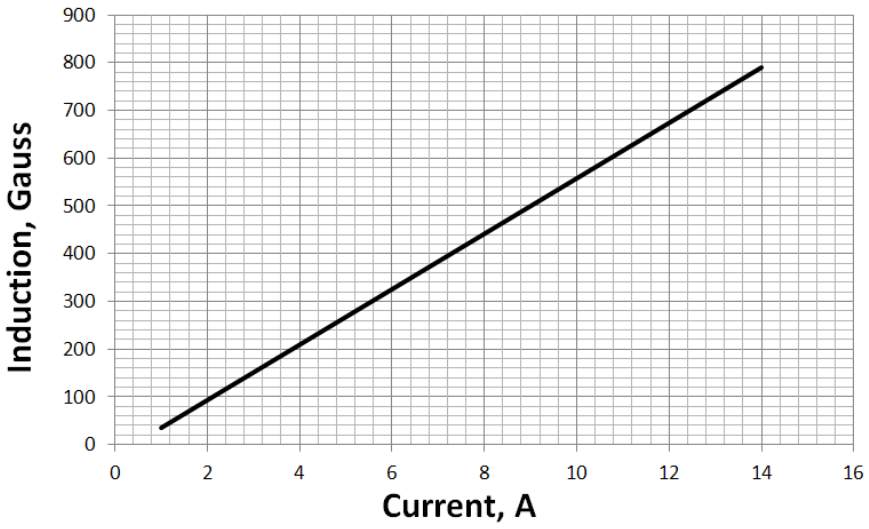

Figure 6.3. Relationship between the current, supplied to the coil and inducted magnetic field

Parameters of the glow discharge process are reported in the table 6.1

base pressure	$1{,}65 \cdot 10^{-8}$ mBar
baking time	16 hours
baking temperature	120^{O}C
process gas	Nitrogen
glow discharge pressure	10^{-3} mBar
cathode current	0,04 A
magnetic field	525 Gauss

Table 6.1. Glow discharge parameters

The process of discharging the sample is depicted in the figure 6.4 Discussion of the results see on the chapter 5.3.8

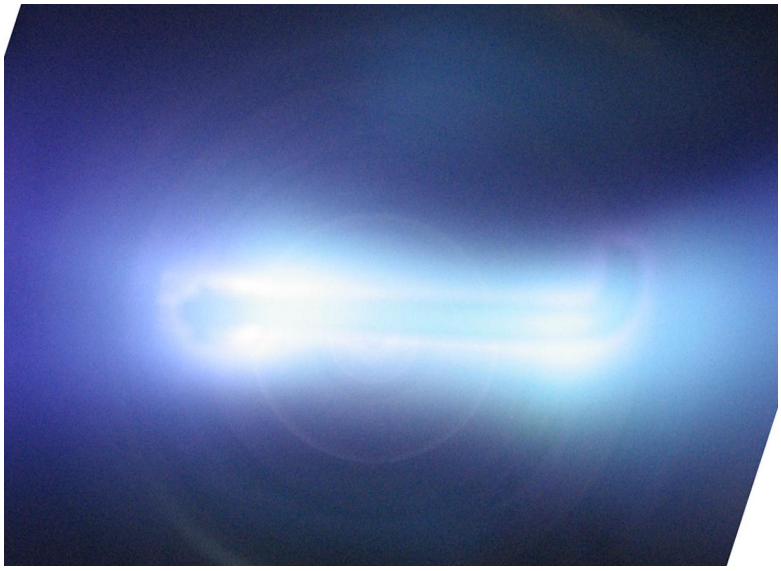

Figure 6.4. Glow discharge process

6.2.4 Anodization

In order to reduce the residual Tin droplets described in the chapter 5.3.8, was provide the anodization of the part of samples. It is well known from electrochemistry, that anodization, is an electrolytic passivation process used to increase the thickness of the natural oxide layer on the surface of metal parts.

The process is called "anodization" because the part to be treated forms the anode electrode of an electrochemical cell. Anodization changes the microscopic texture of the surface and changes the crystal structure of the metal at the surface [23].

The laboratory stand for anodizing the samples is shown in the figure 6.5. It consists of the chemically resistive glass filled with electrolyte. Two electrodes are introduced into the solution – the anode (L-sample), and the cathode, made of stainless steel. When supplying power, on the anode occurs ionization of oxygen, which immediately chemically reacts with material of the sample (Nb), creating niobium oxides. The stoichiometry of oxides is strongly depended on supplied current density. Meanwhile in the cathode occurs the reduction of hydrogen. Glass with electrolyte and electrodes (electrochemical cell) stands on the magnetic mixer with heater built-in. During the process solution is on-time mixing in order to remove the bubbles of hydrogen from the surface of the cathode, and cooling the solution. As a electrolyte for anodizing was chosen the citric acid, as one that showed the most stable results in the work [23]. Power is supplied by voltage – stabilized source, and equal 20V. Time of treatment – 2 minutes.

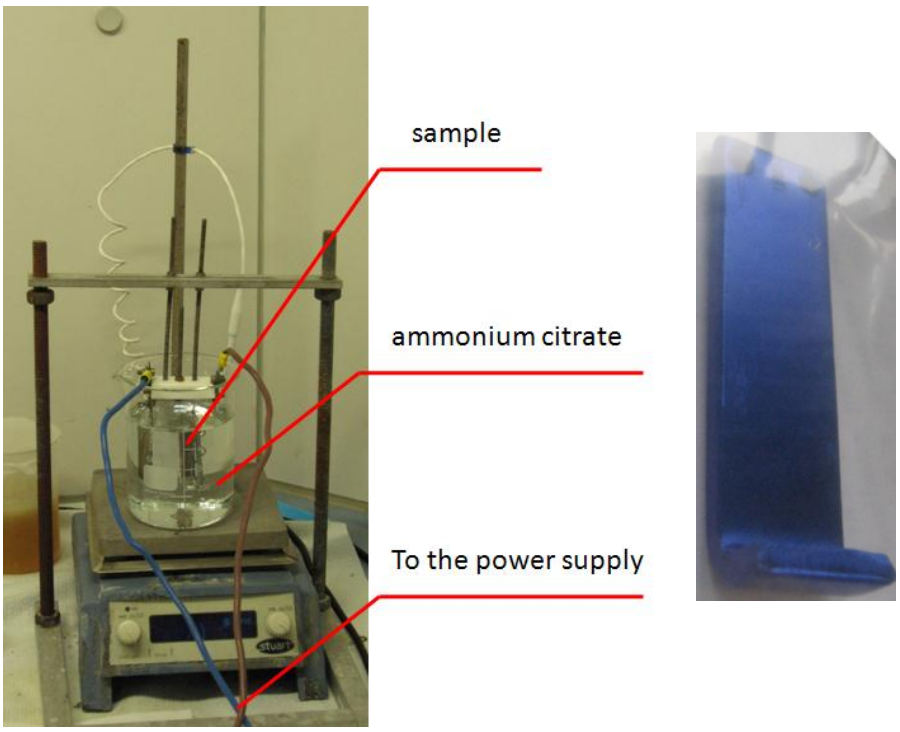

Figure 6.5. Anodization laboratory stand (a) and the L-sample after anodization treatment(b)

6.2.5 Chemical etching

Another kind of treatment, that has been tried in order to increase the purity of the sample surface was the chemical etching. For etching we decide to use the same solution as for BCP (HF 40%, HNO_3 65% and H_3PO_4 85%), but without the ortophosphoric acid, which is normally used as a buffering agent controlling the rate of etching. When introducing the sample to the solution we were observing the high rate reaction, with a big amount of brown gas (NO_3) producing. The rate of reaction grows exponentially with the increasing the temperature. Material erosion becomes too violent and heat evolution makes the solution to boil in 3 minutes.

Process of the chemical etching is depicted in the figure 6.6

Figure 6.6. Chemical etching process

6.2.6 Experimental apparatus for dipping

Experimental apparatus, that was used for producing the Nb_3Sn layer over the superconductive 6 GHz Nb cavities and Nb samples is depicted on the figure 6.7. The high vacuum cylindrical reaction chamber is made of Inconel: it is a Ni-Cr-Fe alloy chosen because of its stability at the high process temperature, that we have to reach. It contains an Alumina crucible with the Tin inside (99.99% nominal purity) (Figure 6.8 (a)). The Al_2O_3 vessel extraction can be done through a long metallic rod which can be hooked up to the Inconel cooling jacket that encloses the crucible. The vacuum chamber has a Chromel-Alumel thermocouple, which monitors temperature in the zone between the chamber wall and the alumina vessel. A pneumatic gauge, mount in the inlet of turbomolecular pump for preventing damage of the pump while venting and opening the chamber. Also there are the nitrogen inlet for venting the chamber, controlled by a leak valve.

The pumping unit is made of a rotary TriScroll (12.6 m^3/h) pump and a turbomolecular pump (70 l/s). A UHV linear manipulator permits us to move the samples (cavity) from the top to the bottom (and vice versa) and to rotate them around the chamber principle axis. To avoid contaminations, the support for the samples is made of niobium (Figure 6.8 (b)).

The chamber (it's lower part) can be heated by an resistive furnace (hot zone) while, to avoid Sn vapor condensation in the manipulator and in the pumping systems, the upper section ("cold zone") can be cooled with a water jacket.

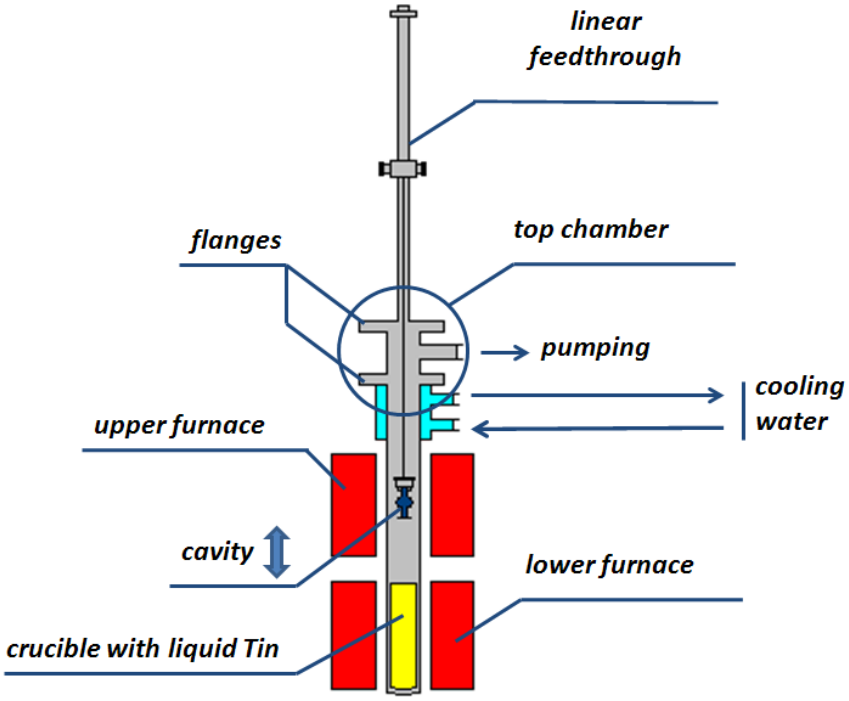

Figure 6.7. Experimental apparatus for dipping

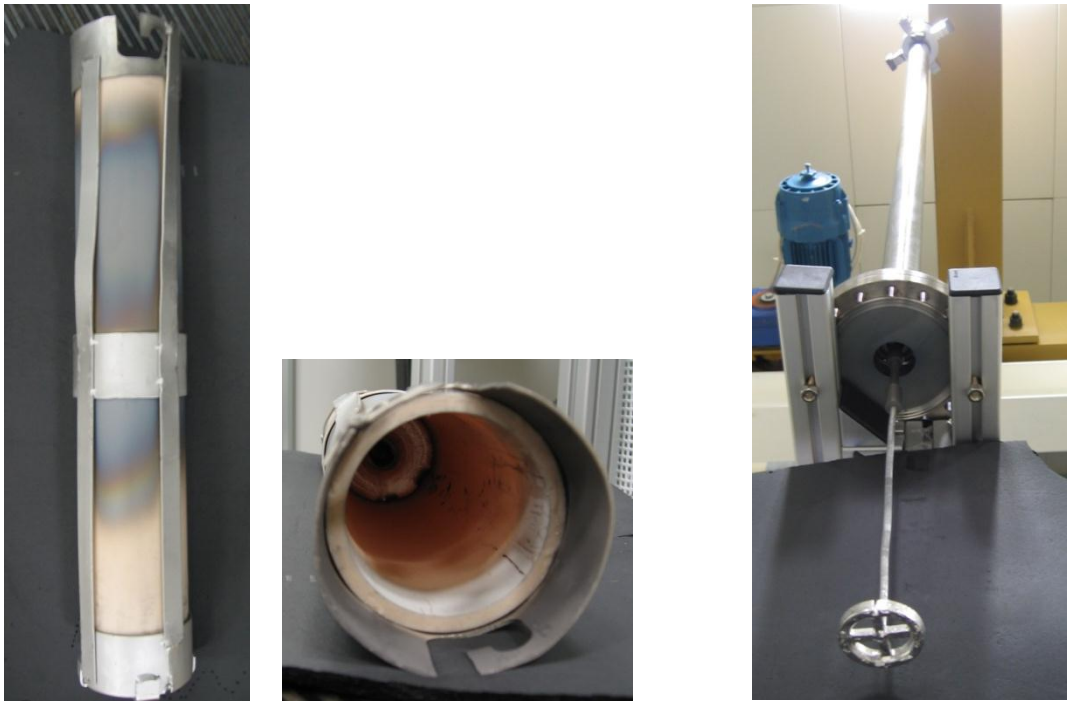

a) **b)**

Figure 6.8. Al_2O_3 crucible with Tin inside (a), and samples (cavity) support (b)

The external furnace has a 30 cm long heating region: its maximum working temperature is 1150±C (1200±C peaks) and controlled by programmable digital controller. During the heating, the chamber bottom is thermally shielded with a ceramic disk in order to reduce the heat loses.

The controlling unit of the stand consists of three main blocks:

- the pumping control unit, which allows to switch on/off the power of all system, the pump, indicates the parameters of turbomolecular pump, has an emergency button, and gate switcher;
- the baking control unit with digital programmable "Eurotherm 2416" and "Eurotherm 3216" temperature controllers;
- the two programmable controllers of external furnaces;

The picture of controlling unit of the stand is given on the figure 6.9

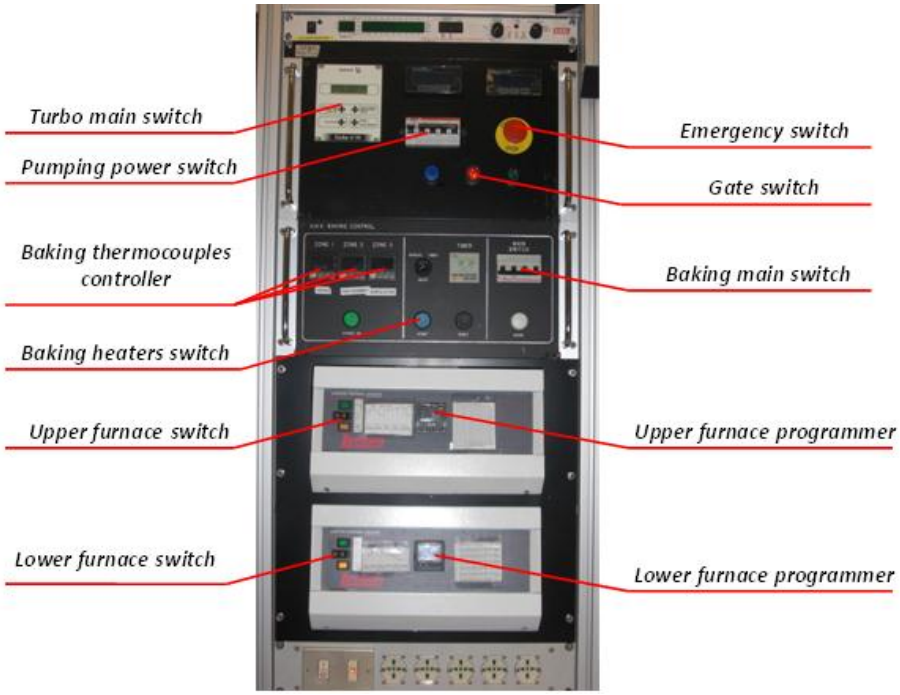

Figure 6.9. Controlling unit

Figure 6.10. Photograph of the liquid tin diffusion experimental stand

6.2.7 Dipping of L-samples

Samples were fixed on the support by means of Niobium wires in order to avoid contaminations (see figure 6.11)

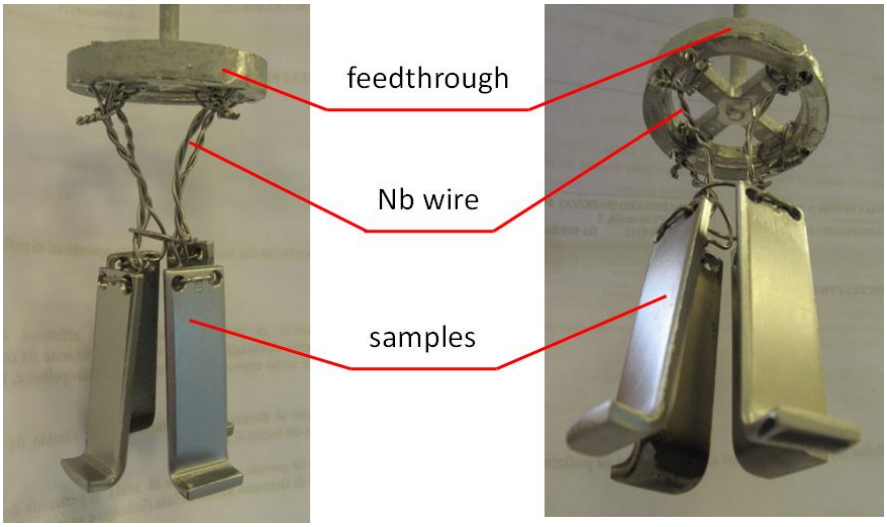

Figure 6.11. The way to fix the samples on the support

Measuring the distance between the manipulator flange end the samples, and knowing the Sn level in the chamber, it becomes easy to calculate the necessary displacements to position the sample inside the liquid bath, in the hot zone or in the cold one. Below it is shown the calculations.

ρ_1(Sn) = 7.365 g/cm^3 (room temperature)

ρ_2(Sn) = 6.99 g/cm^3 (liquid)

$h_1 = 22.2$ cm

$V_{Solid\ Tin} = \pi r^2 \cdot h_1 = 61903$ cm^3

$\rho_1 V_1 = \rho_2 V_2 \rightarrow V_2 = \frac{\rho_1 \cdot V_1}{\rho_2} = 65260$ (cm^3)

$h_2 = \frac{V_2}{\pi r^2} = 23.4$ cm

$\Delta h = h_2 - h_1 = 23.4 - 22.2 = 1.2$cm

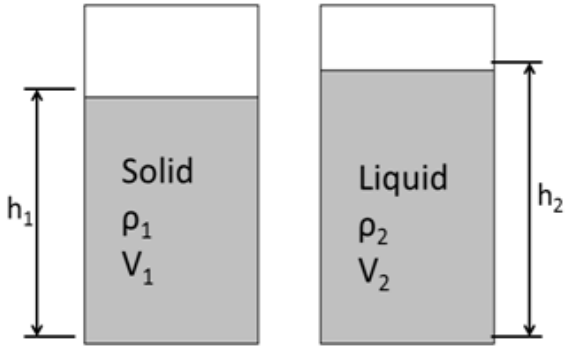

After samples were fixed, and closed inside, the chamber is evacuated until p < $5 \cdot 10^{-6}$ mBar. This process usually takes 2-3 hours. Before starting dipping, in order to degas the surface of the chamber, a baking process was provided. Usually it's about twelve hours long: temperature of the system, during baking process is maintained at 120^{O}C. After baking, when the experimental apparatus cools down, its pressure reaches the order of 10^{-9} – 10^{-10} mBar. And this pressure is a basic for starting dipping.

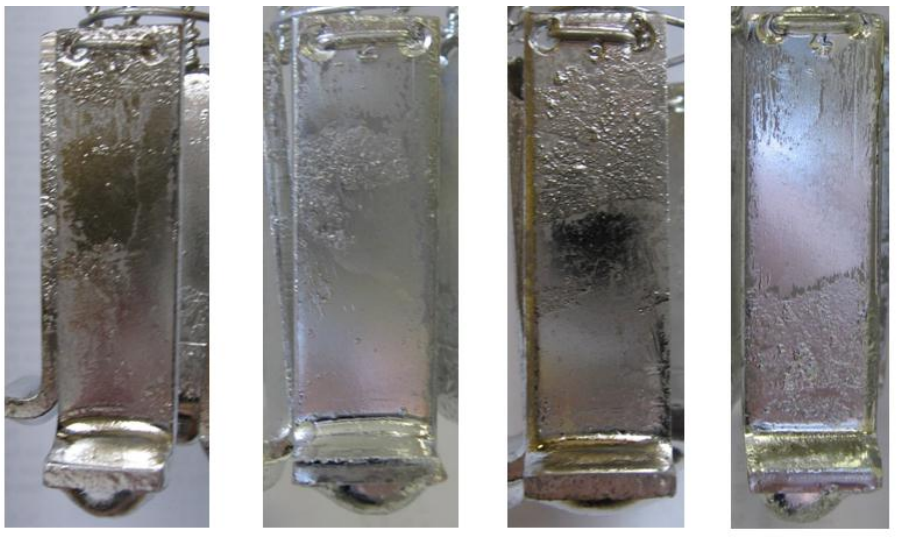

Figure 6.12. L – samples after dipping

The dipping step simply consists in the substrate lowering inside liquid tin through the linear manipulator motion: it has been done for various combinations of T and time. Samples were preheated in the annealing zone before dipping. In this fabrication technique is not anticipated opening the chamber between dipping and annealing steps, that's why it is impossible to represent results of the dipping step before annealing of all samples. Only four samples were taken out just after dipping in order to see the uniformity of the film, and the picture of this samples is represented in the figure 6.12.

6.2.8 Resistive furnace annealing

In order to anneal the samples, resistive furnace is preliminary heated up to $1050^{O}C$. It is the maximum temperature, which is limited by the melting point of Inconel – chamber and the fact, that over this temperature, the process of hydrogen diffusion through the wall of the chamber becomes extremely fast, and this hydrogen contaminates the samples (cavity), what is very undesirable. After dipping step, by meaning of moving up the manipulator, samples are transported into annealing zone for the preliminary estimated time of annealing (4 – 24 hours).

After annealing samples are moved up to the cold zone (which is cooled by water inside the cooling jacket) in order to fix the phase of obtained film. And finally, all the system is cooled down to the room temperature (it takes about 10 hours), pumping stops, the chamber vents with Nitrogen in order to prevent adsorbing of air inside the chamber walls and samples, end the samples are taken out of system.

6.2.9 Obtained films and problem of residual Tin droplets

The most representative results of the obtained films, and the regimes of producing are shown on the table 6.2.

№ of the sample	Preliminary surface treatment	Time of dipping, min	Temperature of dipping, ^{O}C	Time of annealing, min	Temperature annealing, ^{O}C
1-1	alcohol + acetone cleaning	10 min	1050	12 hours	1050
2-1	BCP 10 min	10 min	1050	12 hours	1050
3-1	BCP 10 min + glow discharge 1 min	10 min	1050	12 hours	1050

4-1	BCP 10 min + glow discharge 2 min	10 min	1050	12 hours	1050
1-2	BCP 10 min	2 min	1050	4 hours	1050
2-2	BCP 10 min + anodization	2 min	1050	4 hours	1050
3-2	chemical etching	2 min	1050	4 hours	1050
4-2	glow discharge	2 min	1050	4 hours	1050

Table 6.2. Obtained films on the L – samples by LTD with resistive furnace annealing

Pictures of the samples are represented on the figures 6.13 and 6.14 Numbers of the samples corresponds to same on the table 6.2.

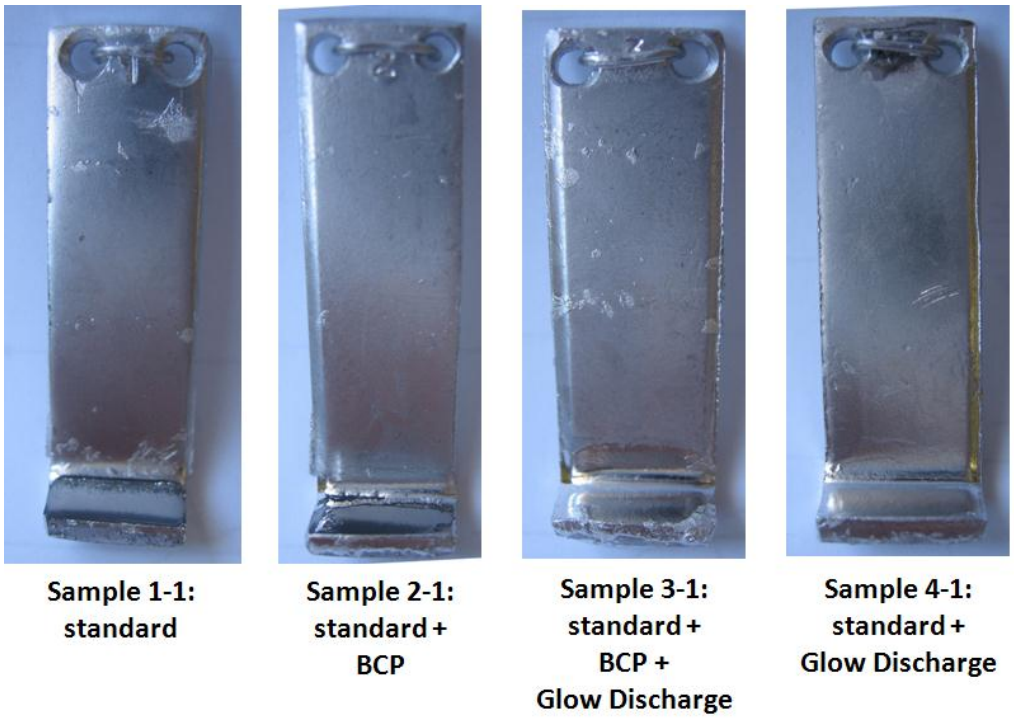

Figure 6.13. L – samples covered with Nb_3Sn with different surface treatments techniques

The main problem, which we were dialed with in this research was the problem of non-uniform coating of the sample after dipping step – a droplet of Tin on the band part of the sample and the residual Tin after annealing.

As one can see from the pictures, each sample has a problem of residual unreacted Tin on the surface, especially on the band part of the sample. From the obtained results we can make the

conclusion, that different surface treatment before dipping doesn't influence essentially on the quality of the film.

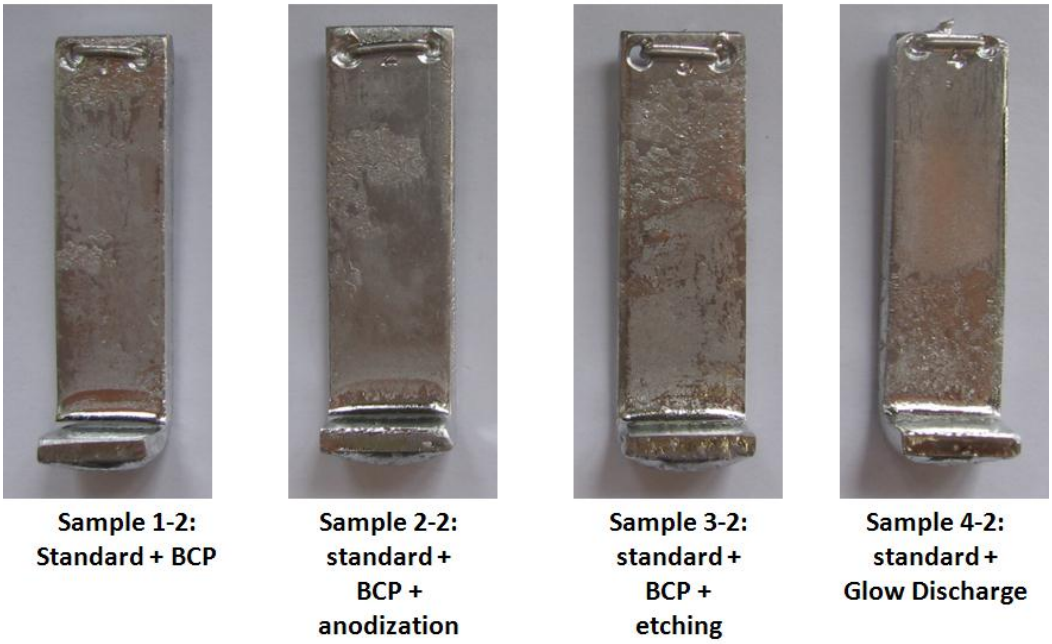

Figure 6.14. L – samples covered with Nb$_3$Sn with different surface treatments techniques

Samples 2-1 and 1-2 which were treated just with the standard technique of ultrasonic cleaning with the following BCP showed the same result as the samples treated with etching, anodization and glow discharge. Only increasing the time of annealing allows us to obtain a little bit better results. But it was proved that with increasing time of annealing, size of residual Tin droplet decreases only up to the one particular moment, after which diffusion stops and the size of droplet doesn't decreases any more. This estimated optimal time of annealing is 8 hours.

We didn't provide any analyses of the samples, produced by this technique because this work has been done during previous two years and as shown in [24], [25] the results of analysis of the samples and cavities which has a residual Tin droplets was not satisfactory.

6.3 Nb$_3$Sn cavities production

6.3.1 Preliminary surface treatments

After the spinning process material has surface defects, stress and dislocations. The cavity cell is characterized by the presence of evident vertical scratches due to the used mandrel (see figure

6.20). The internal surface finishing of a resonant cell is directly correlated to its performance, especially at high fields. Moreover the lubricant, necessary for the metal mechanical processing can contaminate the used material. The idea is to make the surface smooth and free from contaminants. As it is well known in the SRF science, when trying to obtain a Nb_3Sn cavity, the first step is the preparation of niobium substrate in order to get its quality to the maximum possible value. The superior Nb finishing gives us possibility to obtain a more homogeneous Nb_3Sn film.

Mechanical treatments

The primary treatment, which was provided to the cavities in order to reduce vertical scratches due to the used mandrel, was tumbling: the 6 GHz cavities were filled with a certain number of abrasive agent pieces (media), plugged up and fixed to the machine. The tumbler makes the cavity rotate so that the small media pieces can erode the metal surface in a uniform, controllable and reliable way. Before tumbling, in order to remove residual after spinning lubricants and dust cavities were cleaned in the next way:

a. rinsing with DI water;
b. ultrasonic with DI water (60 min);
c. rinsing with DI water;
d. drying with compressed nitrogen;
e. rinse with acetone;
f. rinsing with alcohol;
g. drying with nitrogen.

After cleaning, cavities were filled with a special abrasive media. In this work we used such media as Zr oxide balls and SiC pieces, which are depicted on the figure 6.15.

Figure 6.15. Zr oxide balls and SiC pieces for tumbling

Cavities, with the media inside, were closed with the special plastic flanges, with use of the rubber o-rings, and fixed inside the support by means of the plastic clamps (see figures 6.16, 6.17).

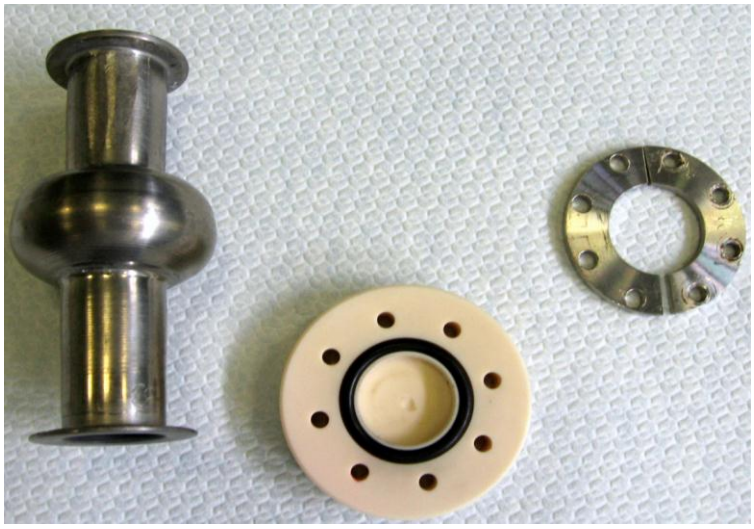

Figure 6.16. 6 GHz cavity and the plastic flange with o-ring

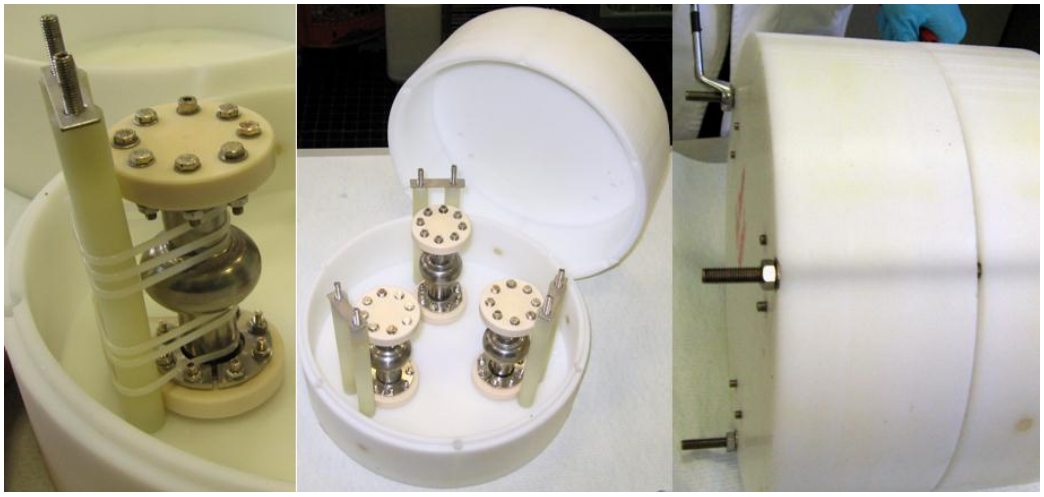

Figure 6.17. Filled with the media cavities fixed in a tumbling support

And finally the support with cavities inside was placed into the drum cavity holder of the tumbler, depicted on the figure 6.18, 6.19.

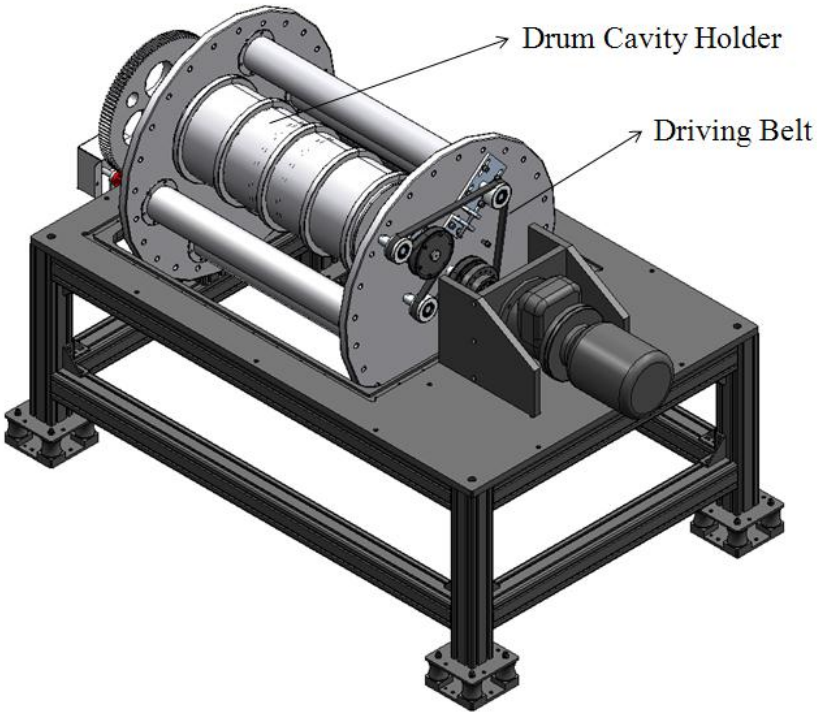

Figure 6.18. Tumbler drawing

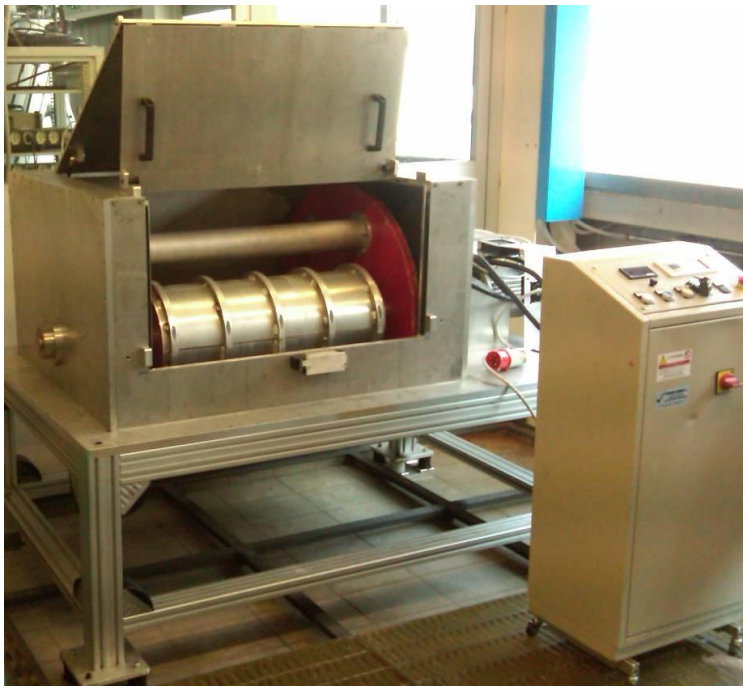

Figure 6.19. Photograph or the tumbler

The tumbling parameters for the 6 GHz cavities are presented on the table 6.3. The speed of the media was calculated with use of next formula:

$$V_{media} = w_2 \times R_2 \tag{6.3}$$

were:

- V_{media} - velocity of the media sliding on cavity wall;
- ω_2 - angular velocity of media inside cavity;
- R_2 - radius of the cavity.

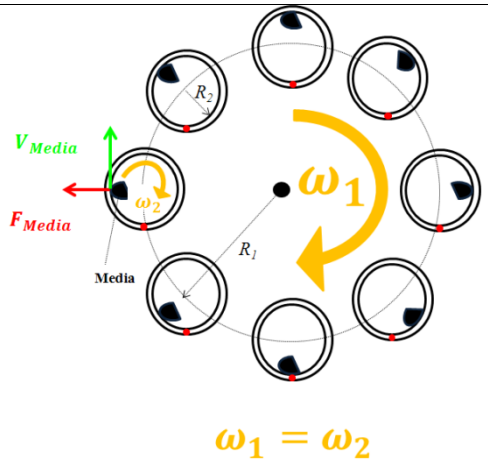

Tumbler Rotary Speed	200 RPM f = 3,3 Hz ω = 20,7	300 RPM f = 5 Hz ω = 31,4
V_{media} [m/s] On Equator R_2 = 0,02 m	0,4	0,6
V_{media} [m/s] On Tube R_2 = 0,01 m	0,2	0,3
F_{media} [N] Mass = 0,005 Kg R_1 = 0,24 m	0,5	1,2

Table 6.3. Tumbling parameters for the 6 GHz cavities

The pictures of the internal surface of the cavity cell-part were taken with use of the special mini-camera, which allows to take pictures with different angle corresponding to the zero-angle (zero angle corresponds to the position of the cavity, when it's number, extruded on the cut-off part is in the lowest point). The picture of the mini-camera and the results of cavity – tumbling is presented on the figure 6.20.

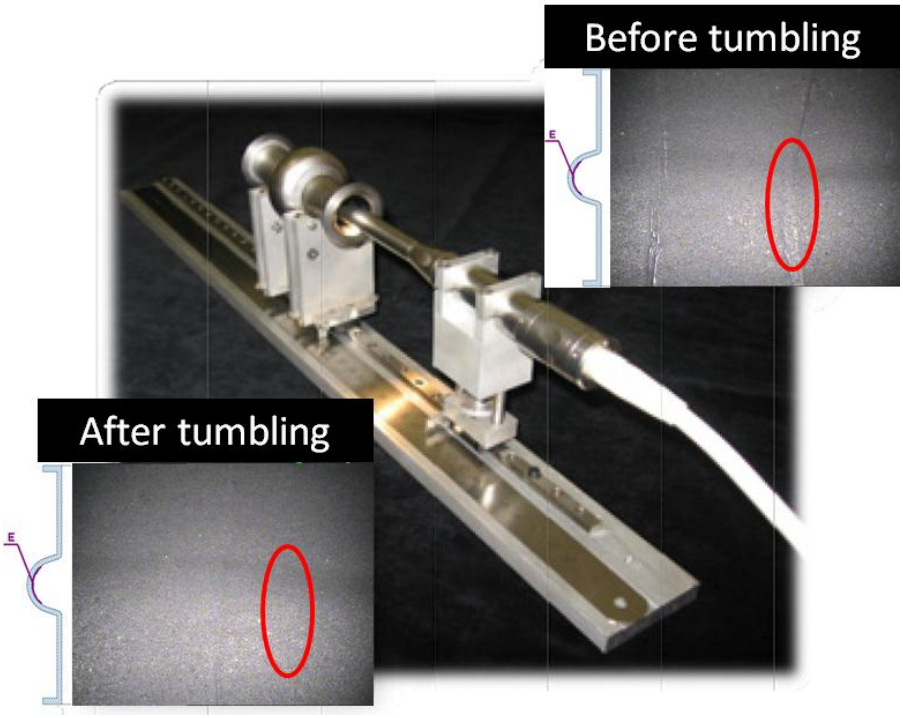

Figure 6.20. Mini-camera for taking pictures of the internal surface of the cavity and the results of 6GHz cavity tumbling (cell-part)

After all mechanical operations follows cavities flanges preparation. Flanges surface must be flat and polished to prevent leaks on cavities rf testing stand. For this aim we used polishing circle with different abrasive papers wetted with water. First is paper 400 for rough treatment which produces flat surface. Next will go 600, 800, 1000 which will decrease roughness. Final is 1200 with using alcohol instead of water. After lapping is necessary to make precise washing of cavity in ultrasound bath with soap in few steps and rinsing.

Chemical treatments

The procedure and solution for 6GHz cavities BCP is the same that for Nb L-samples (see chapter 5.2.2). But the chemical treatment is performed in a pulsed way using a closed circuit. In the static case, a buffer layer forms the concentration gradient in the solution - metal surface zone and H_2 evolution limit the reaction rate. Hydrogen bubbles, which are not evacuated from the cavity cell reduce the rate of chemical reaction. In the pulsed system, the acid flux is directed from the bottom to the top of the cavity in order evacuate the hydrogen, produced during the process. The 3-way valves are used for inversion the flux direction. Stand for pulsed BSP is represented on the figure 6.21.

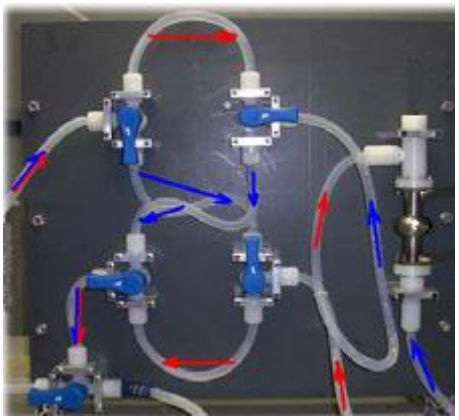

Figure 6.21. Stand for pulsed BSP of 6 GHz cavity

Pictures of the internal surface of the cavity before and after BCP are shown on the figure 6.22.

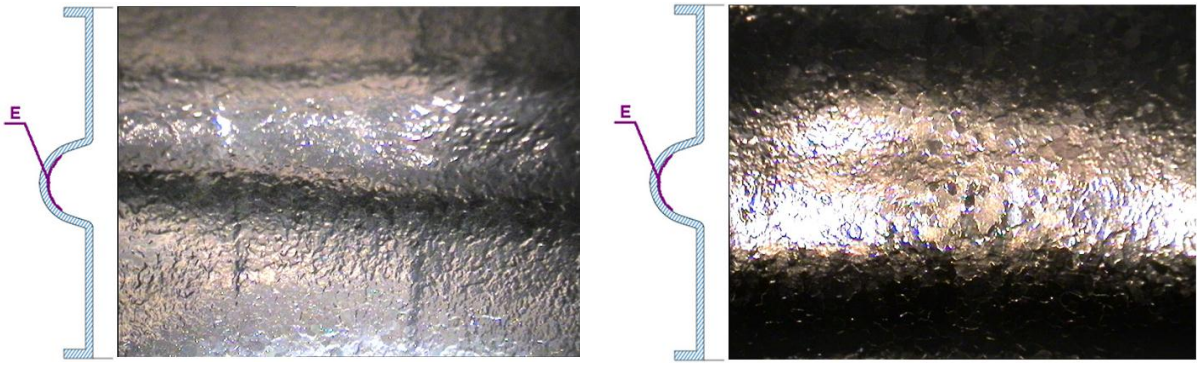

Figure 6.22. Internal surface of the cavity-cell part before (a) and after (b) BCP

6.3.2 Dipping.

For dipping cavities the same experimental stand that for samples was used. Cavities were fixed on the bottom edge of the linear feedthrough with use of Niobium wire in special way, which limits the movement of the cavity. The picture of the cavity, fixed on the feedthrough is shown on the figure 6.23.

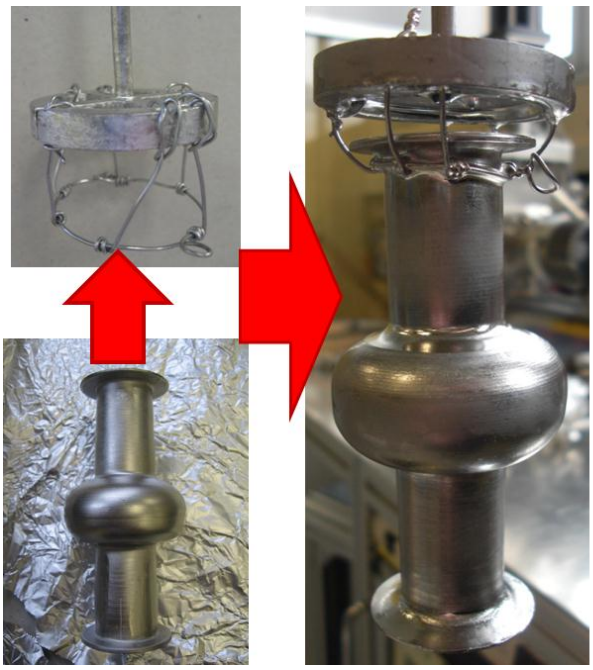

Figure 6.23. The way to fix the cavity on the support

After cavity is fixed, and closed inside, the chamber is evacuated until $p < 5 \cdot 10^{-6}$ mBar. This process usually takes 2-3 hours. Before starting dipping, in order to degas the surface of the chamber, a baking process was provided. Usually it's about twelve hours long: temperature of the system, during baking process is maintained at 120^{O}C. After baking, when the experimental apparatus cools down, its pressure reaches the order of $10^{-9} – 10^{-10}$ mBar. And this pressure is a basic for starting dipping.

The dipping step simply consists in the substrate lowering inside liquid tin through the linear manipulator motion: it has been done for various combinations of T and time.

6.3.3 Resistive furnace annealing

For annealing of each cavity, resistive furnace is preliminary heated up to 1050^{O}C. After dipping step, by meaning of moving up the manipulator, cavity is transported into annealing zone for the preliminary estimated time of annealing (4 – 24 hours). All limitations of the resistive furnace were described in the chapter 5.2.8.

After annealing cavity is moved up to the cold zone (which is cooled by water inside the cooling jacket) in order to fix the phase of obtained film and avoid possible formation of spurious phases such as Nb_6Sn_5 or $NbSn_2$ that one can see on the Nb – Sn diagram. And finally, all the system is cooled down to the room temperature (it takes about 10 hours), pumping stops, the chamber vents with Nitrogen to prevent adsorbing of air inside the chamber walls and cavity, and the cavity is taken out of system.

6.3.4 Obtained coatings

List of the cavities that were done with parameters of process is represented on the table 6.4. As one can see from the table, for some cavities we provide also the pre-heating step, but the long exposure to Sn vapors, at low temperature, could promote spurious phase formations, so soon we decline this step.

№ of the cavity	$T_{pre\text{-}heat}$, ^{O}C $t_{pre\text{-}heat}$, hours	$T_{dipping}$, ^{O}C $t_{dipping}$, min	$T_{anneal}1$, ^{O}C $t_{anneal}1$, hours	$T_{anneal}2$, ^{O}C $t_{anneal}2$, hours	Droplets of Tin
1	300 3	1050 10	1050 4	1050 24	yes
2	1000 1	1050 5	1050 4	/	yes
3	1000 1	1050 5	1050 10	/	yes

Table 6.4. Parameters and results of coating 6 GHz cavities

The main problem of the of the method applied to the 6 GHz cavities was still the presents of droplets of unreacted residual tin. The most problematic zones of the cavity one can see on the figure 6.24.

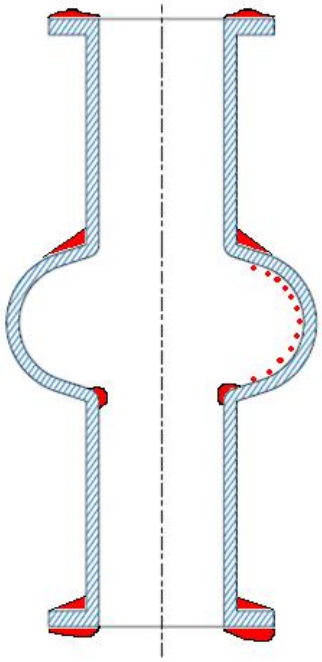

Figure 6.24. Zones of the highest concentration of unreacted Tin on the 6 GHz cavity surface (Tin is marked by the red color)

As shown on the picture, the main zones, where droplets of Tin are concentrated, are on the horizontal planes, because the layer of Sn there is the thickest after dipping step.

In the case of first cavity, after first annealing, the droplets of residual Tin were still present on the internal and external surfaces. So it was decided to provide the second extra- long time annealing (24 hours), in order to estimate possibility of removing residual Tin by slow evaporation at $1050^{O}C$. Pictures of the external and internal surface of the first cavity are represented below.

Cavity №1 after first annealing (figure 6.25):

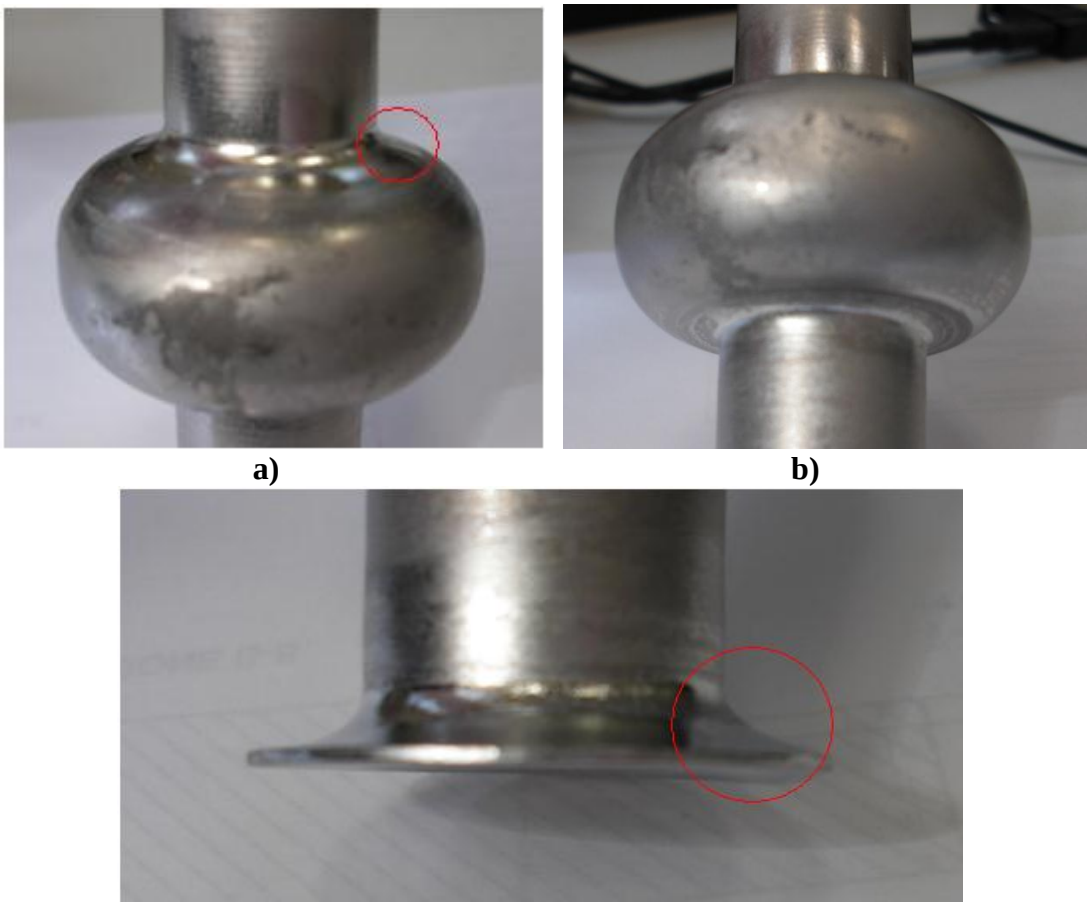

Figure 6.25. External surface of the cavity №1 after first annealing. Tin accumulation on the upper part of the cell (a), clear lower part of the cell (b) and the layer of Tin on the lower flange (c)

And the same cavity after second annealing is represented on the figure 6.26.

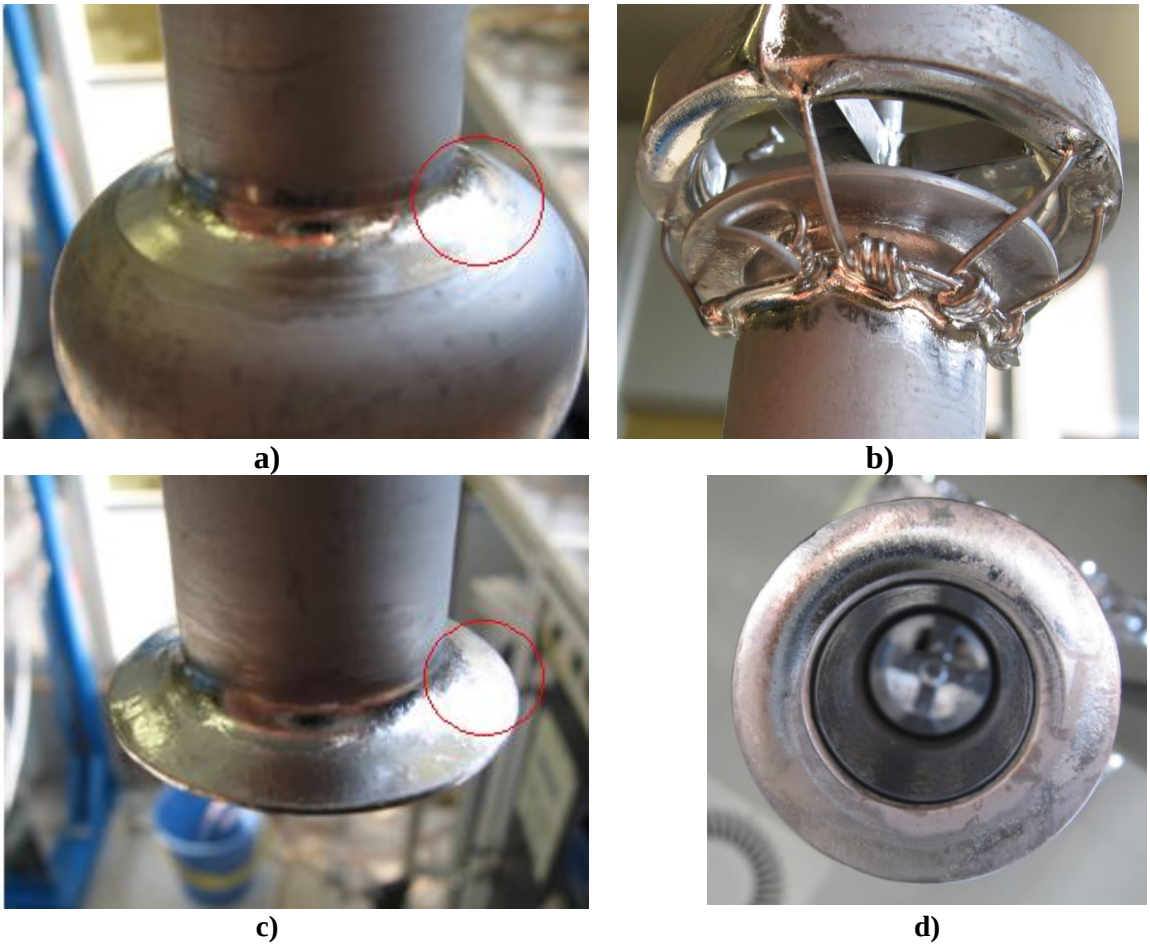

a) **b)**

c) **d)**

Figure 6.26. External surface of the cavity №1 after first annealing. Tin accumulation on the upper part of the cell (a), upper flange and the support (b) and the layer of Tin on the lower flange (c), (d)

The second and third cavities were made with one – step annealing, 4 and 10 hours correspondingly. But for this cavities the temperature of pre heating was increased to 1000^{O}C. The pictures of this cavities are presented on the figures 6.27 and 6.28.

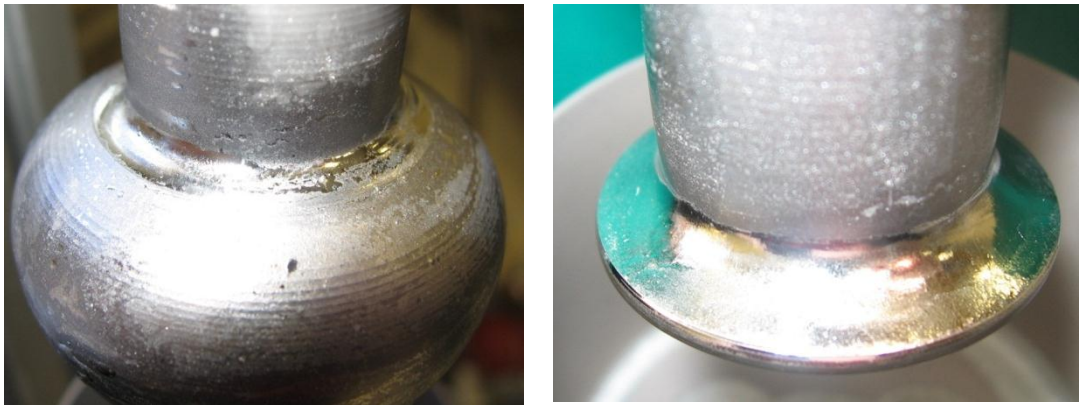

a) **b)**

Figure 6.27. External surface of the cavity №2 after annealing. Tin accumulation on the upper part of the cell (a), and the lower flange (b)

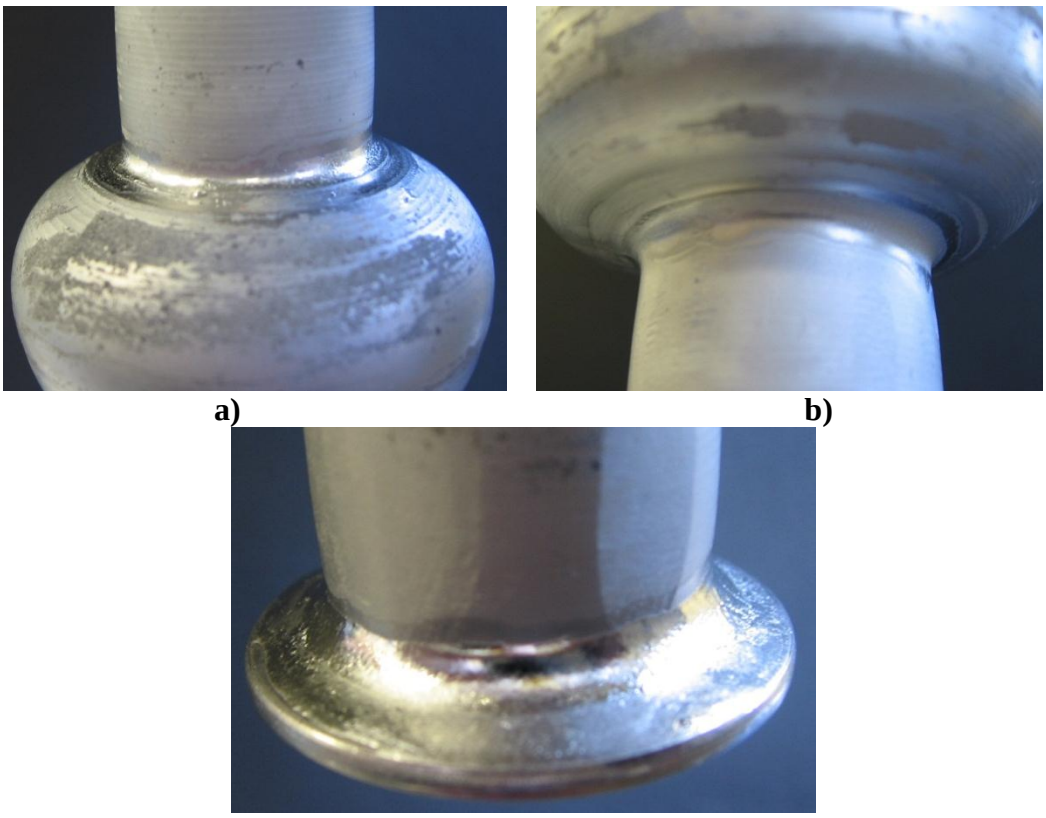

Figure 6.28. External surface of the cavity №3 after annealing. Tin accumulation on the upper part of the cell (a), lower part of the cell is clear (b), and the lower flange (b) is covered with the layer of Tin

6.4 Nb_3Sn 6 GHz cavities analysis

6.4.1 Internal surface pictures by mini – camera

Because of the resonator small dimensions the 6 GHz internal surface inspection is quite complex. 6 GHz cavities have been observed through a miniature camera (which is described in the chapter 5.3.1) to check the material surface after each performed operation: a series of photographs can be easily taken to monitor the internal surface of the cavity. On the picture 6.29 is represented the pictures of the cavity №1 internal surface.

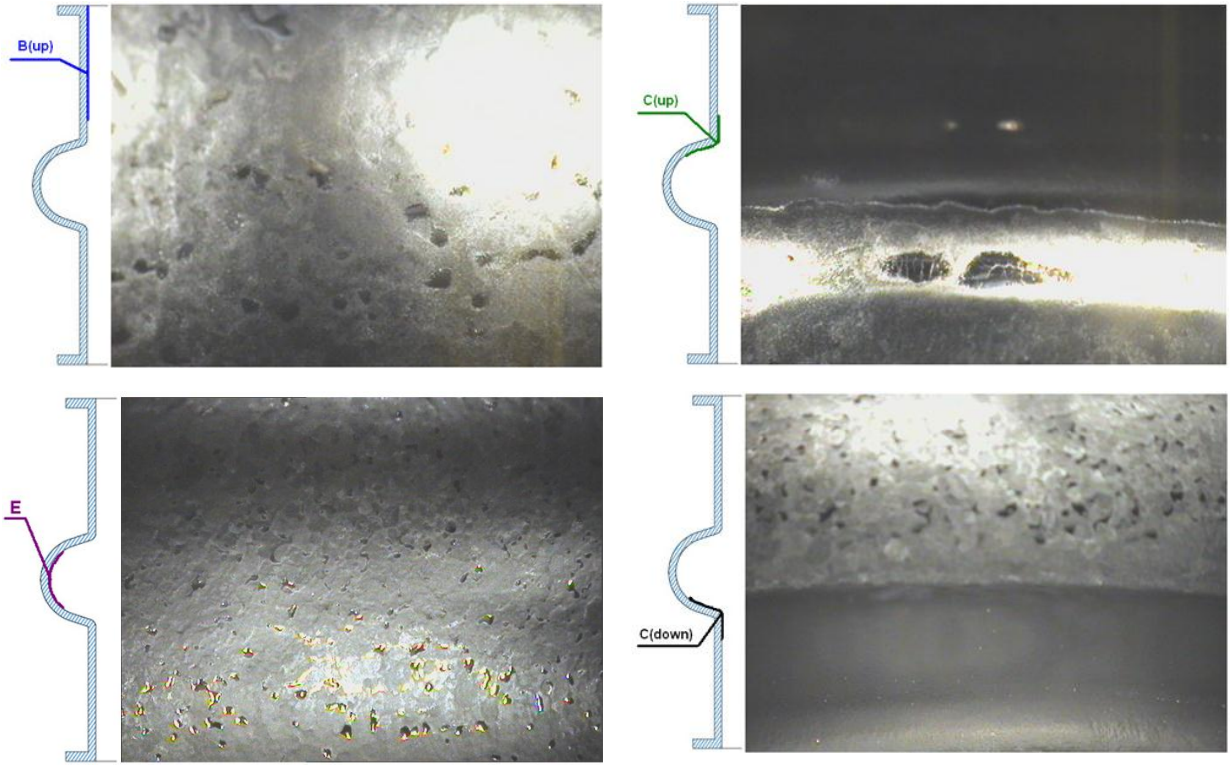

Figure 6.29. Internal surface of the cavity №1 after first annealing. Accumulation of residual Tin on the different parts of the cavity.

As one can see from the figure 6.29, the Tin droplets problem is particularly evident: droplets are present on the both cut-off part (less) and especially the cell bottom and iris parts.

6.4.2 RF - test

The work of measuring Q_{value} of the cavities which has droplets of residual Tin inside was done for previous 3 years [24], and it was absolutely proved, that cavities with residual Tin doesn't show a good Q_{value}. So, in order to economy time and materials, we didn't provide rf – tests of the cavities with residual Tin, because the result was wittingly bad. As an example, here is shown one of results of measuring the Q_{value} of the cavity with Nb_3Sn film and residual Tin droplets in comparison with pure Niobium cavity, which was treated just mechanically and BCP (figure 6.30). As one can see from the plot, the Qvalue of treated cavity is one order of magnitude worth, than pure Niobium cavity.

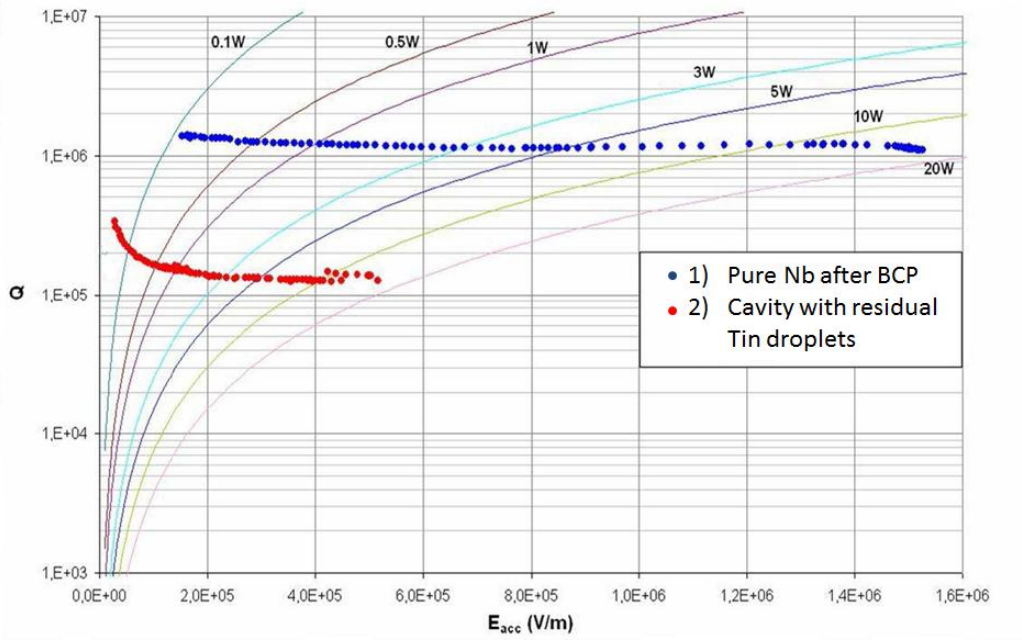

Figure 6.30. Results of measuring the Q_{value} of the cavity with Nb_3Sn film and residual Tin droplets in comparison with pure Niobium cavity, which was treated just mechanically and BCP

7. Nb_3Sn by LTD with high-temperature annealing

After a lot of work, that has been done during 3 years in the Liquid Tin Diffusion method we understood that the only one way to solve the problem of residual Tin droplets is rising the temperature of annealing in order to improve the diffusion of Tin into Niobium, and evaporate all residuals. The base idea of the liquid tin diffusion method with high – temperature inductive annealing is the same as for standard LTD technique: introducing the Niobium substrate into a molten Sn bath and in its subsequent annealing. But the high temperature annealing gives some advantages in comparison with standard resistive furnace annealing. This advantages are:

- the maximum temperature, that can be reached is much higher than the temperature of resistive furnace and lies in the range of 1900 – 2100^{O}C;
- time for heating the cavity (or the sample) from 0 to 1500^{O}C is less than 3 minutes;
- no diffusion of the contaminations through the wall of the chamber, because it stays relatively cold;
- chamber doesn't heats during the annealing so it becomes possible to use stainless steel as a material for chamber;
- technique doesn't require cooling of the chamber;

7.1 Nb_3Sn samples production

7.1.1 L – samples and LL – samples

For producing Nb_3Sn coating by LTD with high-temperature annealing were used two kind of samples: the L – samples and the so called LL – samples. L – samples were described in detail on the chapter 6.2.1. The LL – samples carries out the same role that L – samples, but they are smaller in dimensions and consequently easier for analysing. Samples are made of Niobium, has 20 mm long, 10 mm wide and has the LL – shape as shown on the picture 7.1. Each sample has its own number, made by extrusion.

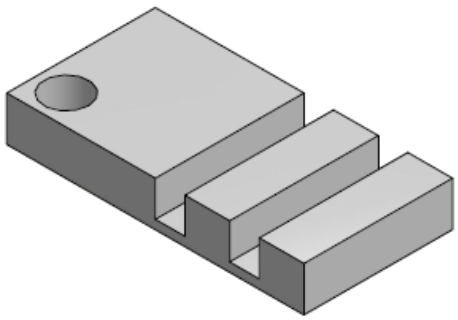

Figure 7.1. The LL – sample

7.1.2 Preliminary surface treatments (mechanical treatment and BCP)

Preliminary surface treatments of the L – samples were described in detail in the chapter 6.2.2 and consist of:

- mechanical treatment (lapping);
- chemical treatment (BCP).

The LL – samples are not scratched and their surface finishing is satisfactory. Our substrates have just been subjected to a BCP.

7.1.3 Procedure of dipping

The experimental apparatus and procedure of dipping stage has not been changed, and is the same as for dipping the samples and cavities produced by "standard" technology with resistive furnace annealing. It was described in details in the chapters 6.2.6 and 6.2.7. The only one difference is that the samples extracts from the chamber just after dipping in order to be annealed in the chamber of induction heater.

For annealing in induction oven were produced 14 samples. The list of this samples (both L- and LL-, with process parameters is given on the table 7.1.

№ of the sample	Type of the sample	Time of dipping, min	Temperature of dipping, ^{O}C
1-1	L	10 min	1050
2-1	L	10 min	1050
3-1	L	10 min	1050
4-1	L	10 min	1050
1-2	L	2 min	1050
2-2	L	2 min	1050
3-2	L	2 min	1050
4-2	L	2 min	1050
1-3	LL	10 min	400
2-3	LL	10 min	400
3-3	LL	10 min	400
4-3	LL	10 min	400
5-3	LL	10 min	400
6-3	LL	10 min	400

Table 7.1. Parameters of the samples dipping process

The film, that was obtained as the result of dipping stage is depicted in the figure 7.2. As one can see from the picture, film is not uniform, with the presence of the droplets of Tin, especially in the corners. And this picture is representative for all produced samples after the dipping stage. From this we can resume, that the most important stage, that influence on the quality of Nb_3Sn film, produced by LTD is annealing.

Figure 7.2. Film obtained as the result of dipping on LL – samples

7.1.4 Inductive annealing experimental apparatus

For inductive annealing both the samples and the 6 GHz cavities was specially designed a new experimental apparatus which is depicted on the figure 7.3. It consist of the two main parts: vacuum system and inductor.

The high vacuum cylindrical reaction chamber is made of stainless steel. In this case we don't need using Inconel, because the chamber stays relatively cold during the process. It contains a 7 – rings copper inductor work coil (Figure 7.4 (a)). The vacuum chamber has a Chromel-Alumel thermocouple, which monitors it's temperature. Inductor chamber connected to the main vacuum chamber through the whole – metal valve. A pneumatic gauge, mount in the inlet of turbomolecular pump for preventing damage of the pump while venting and opening the chamber. Also there is the nitrogen inlet for venting the chamber, controlled by a leak valve.

The pumping unit is made of a rotary TriScroll (12.6 m^3/h) pump and a turbomolecular pump (70 l/s). A UHV linear manipulator, connected to the upper flange of the chamber permits

moving the samples (cavity) up and down in the range of 50 mm in order to find the best position inside the work coil while preparing the chamber to experiment. To avoid contaminations, the support for the samples is made of niobium (Figure 7.4 (a)).

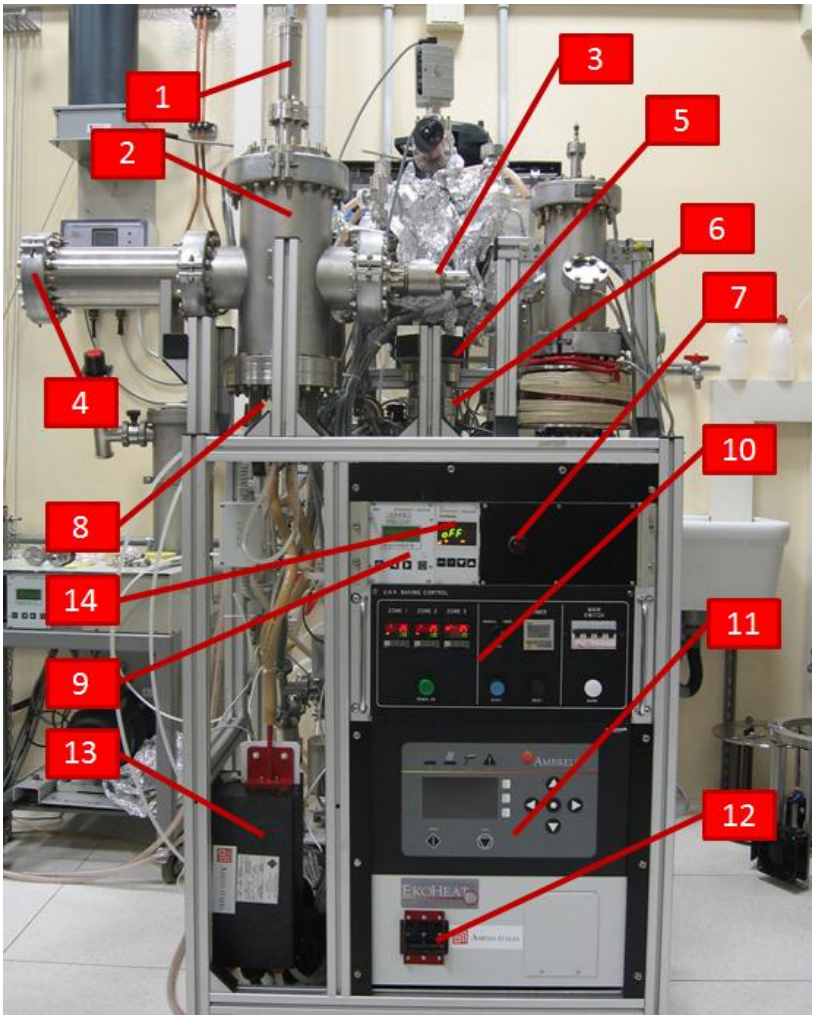

Figure 7.3. Inductive annealing stand

1-manipulator; 2-vacuum chamber; 3-whole metal valve; 4-window flange; 5-pneumatic gauge; 6-turbomolecular pump; 7-gauge switcher; 8-inlet of work coil; 9-pump controller; 10-baking control unit; 11-induction heater controlling and inverter block; 12-inductor main switcher; 13-tank capacitors block; 14-pressure indicator.

Vacuum chamber has a window flange which needed for precise displacing the samples inside the work coil, and for visual control of the annealing process. As it is well known from the theory the inductor main coil must be well insulated from the chamber. That's why in this system we use the lower flange (through which work coil enters the chamber) with the ceramic insulator.

During annealing inside the chamber creates the atmosphere of evaporated Tin, which sedimentates to the walls and bottom of the chamber. To prevent short circuit of the inlet and outlet

tubes of the work coil by sedimentated Tin we decide to use the ZrO_2 balls. The capacity of the lower flange is filled with this balls as shown on the figure 7.4 (b). After each experiment the balls are mixed, and so we can use the one "charge" of balls for 3-5 annealings. After balls are totally covered by Tin, they can de recovered by chemical etching and used again and again.

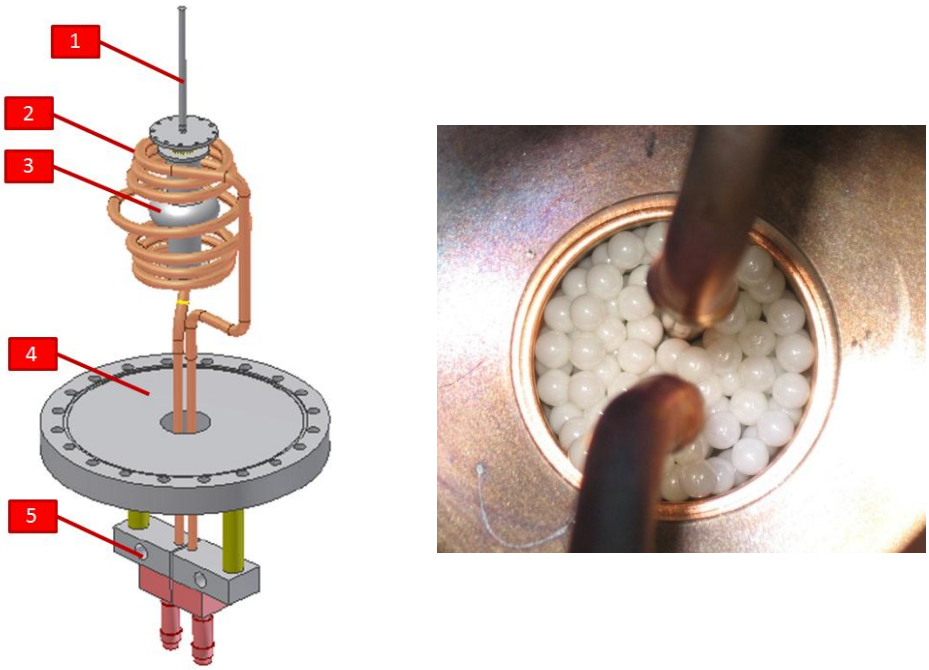

a) **b)**

Figure 7.4. Lower flange with work coil (a) and the ZrO_2 balls in the lower flange capacity (b).

1-Nb samples/cavity support; 2-work coil; 3-cavity; 4-flange; 5-cooling water inlet/outlet

The inductor that is used in our research is the EKOHEAT Model 10C 300-0771. It contains two main blocks: The power control block (11, figure 7.3), and the parallel resonant circuit content of tank capacitors block (work head, 13, figure 7.3) which is connected to the copper work coil (2, figure 7.4). Work coil made with the shape which follows the shape of the cavity for improving the uniform heating. Power control block is made on the two inverters build on the power IGBT, and has programmable interface. Tank capacitor block has summary capacitance of 2μF with 1000 V_{RMS} voltage. Here are listed some important features of the inductor heating system:

- efficient heating of many part geometries (either samples or cavities);
- agile operation for repeatable, reliable results;
- touch – pad interface for control and programming;
- backlight LCD display for indicating data;
- electrically isolated water-cooled work head.

The power can be controlled using one of following ways:

- manually from the front panel;
- remotely by the signals provided to the rear panel;
- remotely through the RS-485 serial communication port;
- from one of 10-step heating profiles specified in advance.

The parameters of the inductor are represented on the table 7.2.

Feature	**Value**	**Units**
Power supply		
Dimensions H×D×W	432×616×451	mm
Construction	aluminum	
Weight	32	kg
Input AC Voltage	360-520	V_{RMS}
Input Frequency	50-60	Hz
AC Line Power	11	kVA max
Power Factor	0.92	
Output Frequency	50-150	kHz
RF Output Voltage	1020	V_{RMS} max
Output Power	10	kW max
Work head		
Dimensions H×D×W	229×203×457	mm
Mounting	M6×1×12 screws (8×)	
Weight	20	kg
Total capacitance	2	μF
Voltage	1000	V_{RMS} max
Work coil		
Material	copper	
Number of rings	7	
Cooling	water	

Table 7.2. Parameters of the induction oven

7.1.5 Inductive annealing procedure

After finishing the dipping step, samples are mounted to the inductive annealing chamber. For fixing the samples on the support is used Niobium wire, as shown on the figure 7.5. After samples were fixed, and closed inside, the chamber is evacuated until $p < 5 \cdot 10^{-6}$ mBar. This process usually takes 1-1,5 hours. Before starting annealing, in order to degas the surface of the chamber and improve vacuum, a baking process is provided. Usually it's about twelve hours long:

temperature of the system, during baking process is maintained automatically at $120^{O}C$. After baking, when the experimental apparatus cools down, its pressure reaches the order of $10^{-9} – 10^{-10}$ mBar. And this pressure is a basic for starting annealing.

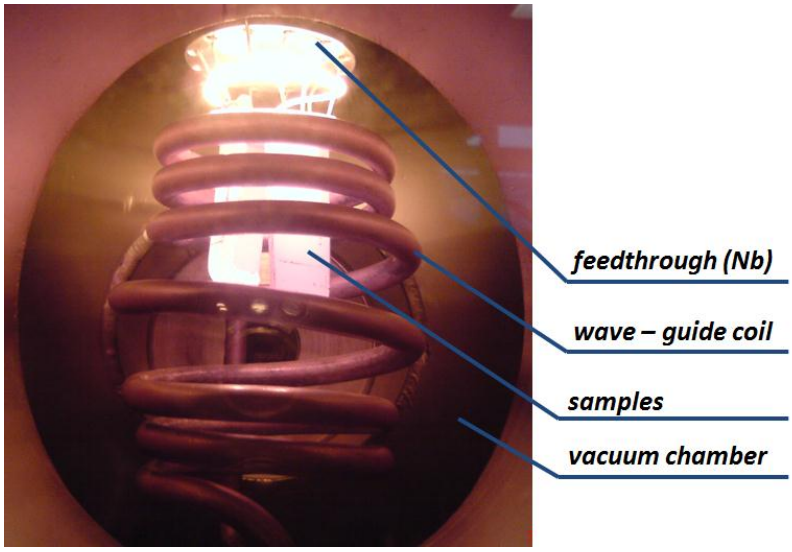

Figure 7.5. Process of L-samples annealing

Before switching on the system, it is necessary to open the cooling water flow through the power supply, and the work head. After follows switching on the inductor and choosing the way of power control (manually or automatically). In the case of automatical control, annealing is simply consist of pressing start button, and after the system will automatically follow chosen pre-set heating program. In the case of manual control, operator have to control the output power by controlling the invertor voltage.

The temperature of the samples (cavity) is controlled through the window – flange (4, figure 7.3) by the IRtec P-2000 infrared pyrometer, fixed on the special 3 – legs support. Pyrometer is shown on the figure 7.6.

Figure 7.6. Pyrometer IRtec P-2000

Using this instrument permits measurement of the temperature starting from $500^{O}C$. But in fact, during the annealing process the window is progressively metalises with the Tin, and measurement firstly becomes not correct, and after totally impossible. That is why we were trying to estimate the quality of the Nb_3Sn film as a function of output inverter voltage, but not of temperature.

7.1.6 Obtained films

The regimes of samples annealing are represented on the tables 7.3 (L-samples 1-2, 2-2, 3-2, 4-2); 7.4 (LL-samples 1-3, 2-3, 3-3, 4-3, 5-3, 6-3). The frequency in all cases was constant and equals 85 kHz.

Output voltage, V	Output power, kW	Pressure, mBar	approximate temperature, ^{O}C	time of step, min
100	0,7	1×10-5	//	1
200	2,2	1,1×10-5	1118	1
250	3,3	9,3×10-6	1320	1
300	4,6	2,6×10-5	1500	2
Total Time of annealing, min				5

Table 7.3. Annealing parameters of the L-samples 1-2, 2-2, 3-2, 4-2

The photograph of the L-samples 1-2, 2-2, 3-2, 4-2 is represented on the figure 7.7.

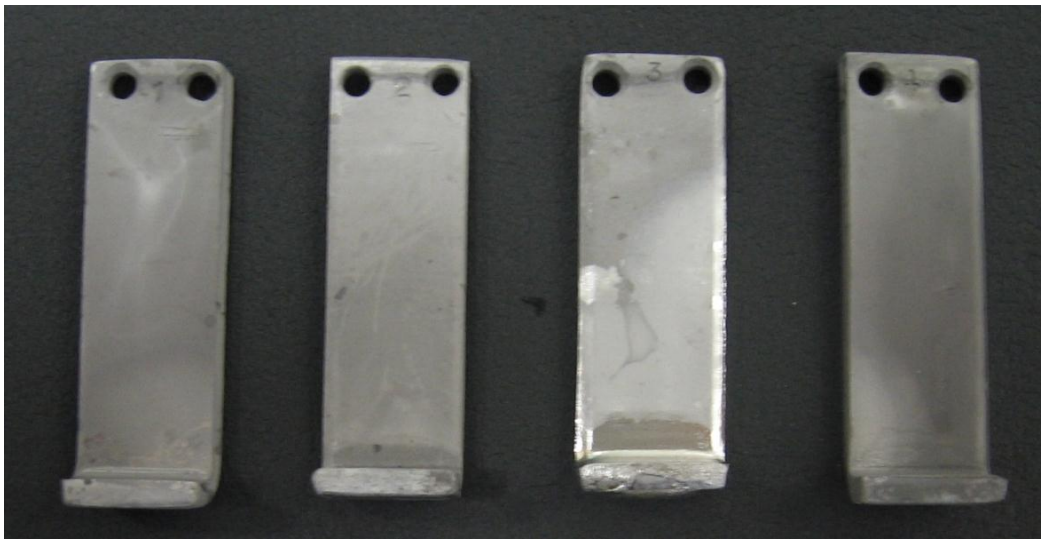

Figure 7.7. The photograph of the L-samples 1-2, 2-2, 3-2, 4-2 after annealing in the induction oven

As one can see from the picture 7.6, the Nb_3Sn film is very uniform and without droplets of residual Tin (except the sample number 3-2), which has a biggest quantity of residual Tin after dipping stage.

Output voltage, V	Output power, kW	Pressure, mBar	approximate temperature, ^{O}C	time of step, min
100	0,6	5,5×10-6	610	5
200	1,6	1×10-5	920	5
250	2,1	4,4×10-6	1030	5
320	3,2	1,2×10-6	1160	5
360	3,9	3,9×10-7	//	30
400	5,1	4,3×10-7	//	20
Total Time of annealing, min				70

Table 7.4. Annealing parameters of the LL-samples 1-3, 2-3, 3-3, 4-3, 5-3, 6-3

The photograph of the LL-samples 1-3, 2-3, 3-3, 4-3, 5-3, 6-3 is represented on the figure 7.8.

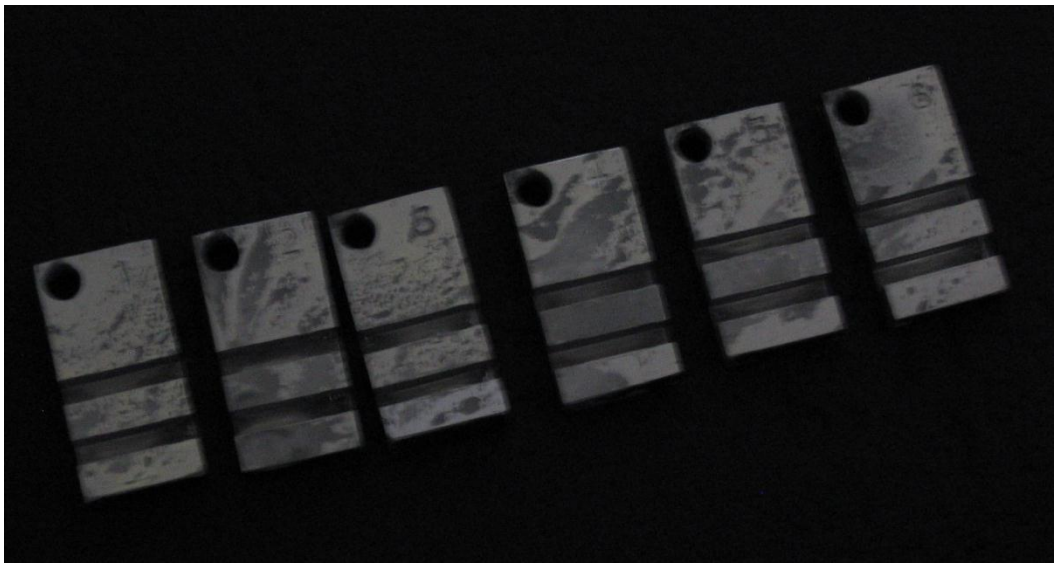

Figure 7.8. The photograph of LL-samples 1-3, 2-3, 3-3, 4-3, 5-3, 6-3 after annealing in the induction oven

7.2 Nb_3Sn samples analysis

The Nb_3Sn samples we obtained are described. The instruments that were used for samples analysing are: X-ray diffractometer to examine the crystal structures of the samples, a inductive (phase shift) system to evaluate Tc and ΔT_c. Below are reported the results of the samples analysing.

7.2.1 XRD measurements

The X-ray diffraction analysis is extremely useful to have information about the obtained material crystal structure and plane orientations. Furthermore it is possible to detect the eventual presence of undesired species.

The instrument at our disposal is a diffractometer "X'Pert-Pro" (produced by the Philips company). The X-ray beam wavelength is 0.15428 nm (Cu Kα). During scanning the incident beam is fixed at a small angle (calculated respect to the sample surface) while the detector rotate depending on the parameters chosen through the software (mainly start and stop angles and acquisition time). Changing the operation mode it is possible to increase the examined penetration depth (both beam source and detector move, one towards the other). The XRD spectra have been acquired for the most of the samples.

On the pictures 7.9, 7.10 is shown the bulk scan and the thin film scan typical spectra of obtained coatings on the samples, produced by LTD with inductive annealing.

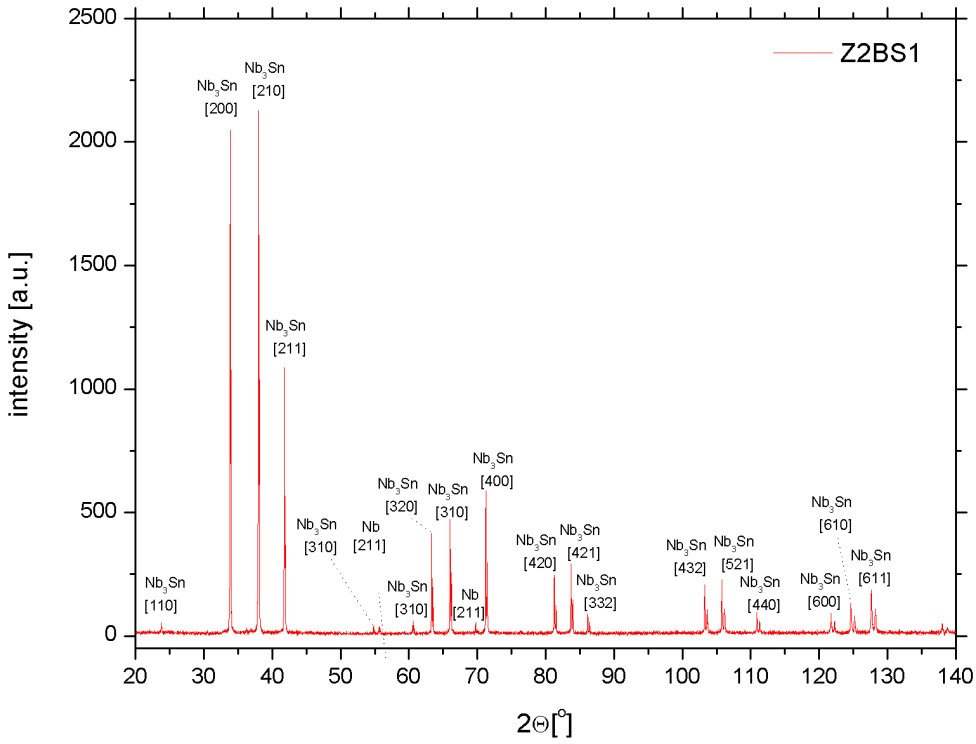

Figure 7.9. The bulk scan XRD spectra of the sample, produced by LTD with annealing in the induction oven

As it is seen from the XRD spectra, all of the peaks are associated to the Nb_3Sn A15 phase, confirming the method of LTD with inductive annealing as the very encouraging technique that must be developed more and more.

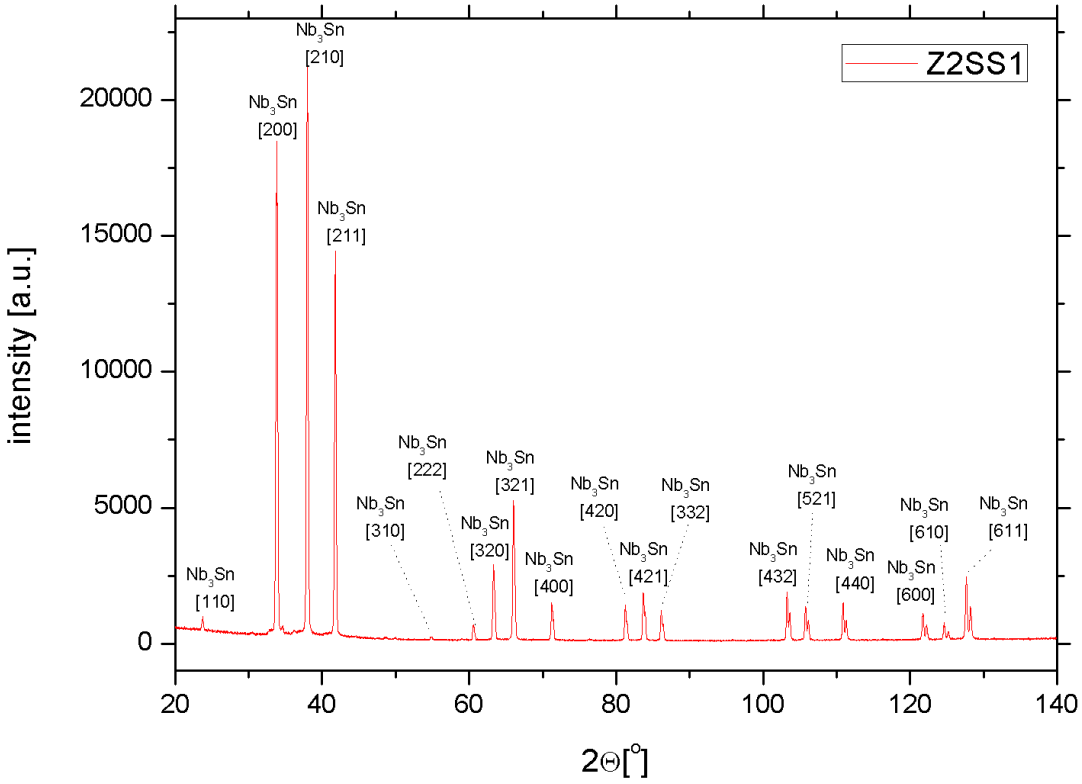

Figure 7.10. The thin film scan XRD spectra of the sample, produced by LTD with annealing in the induction oven

7.2.2 Inductive T_c and ΔT_c measurement

Measuring Tc and ΔT_c in this work was done with use of inductive method. The method makes use of the perfect shielding of a magnetic field by a superconducting thin film carrying subcritical current densities only. This technique implicates using of a two – coil arrangement, which is shown on the figure 7.11. Samples were cooling down with the liquid helium, by dipping the set up into the helium tank.

The results of measuring T_c and ΔT_c on the LL – samples are represented on the table 7.5.

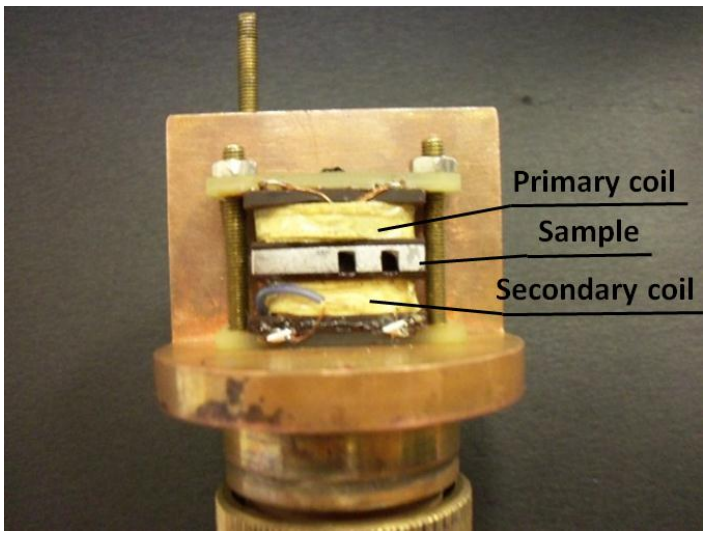

Figure 7.11. Two coil arrangement of the inductive T_c set up

Number of the sample	Theoretical value	1	2	3	4	5	6
T_c1, K	18,2	17,91	17,89	17,88	17,90	17,90	17,80
ΔT_c1	//	0,07	0,06	0,04	0,06	0,06	0,12
T_c2, K	9,2	9,31	9,27	9,27	9,30	9,28	9,28
ΔT_c2	//	0,01	0,01	0,01	0,01	0,02	0,01

Table 7.5. Results of measuring T_c and ΔT_c on the LL – samples

7.3 Nb_3Sn 6 GHz cavities production

7.3.1 Preliminary surface treatments

The goal of the cavity preliminary surface treatments is to make the internal surface smooth and free from contaminants. As it is well known in the SRF science, when trying to obtain a Nb_3Sn cavity, the first step is the preparation of niobium substrate in order to get its quality to the maximum possible value. All the cavities, before depositing the film were treated mechanically (tumbling) and chemically (BCP) as described in the chapter 6.3.1.

7.3.2 Dipping

The dipping step has not been change, and the procedure is totally the same as described in the chapter 6.3.2.

For inductive annealing was produced 4 cavities: №№ 33, 5, 25, 29. We did two different ways of dipping process: with pre- and post- heating of the cavity, and just a standard dipping without this steps. Pre heating was provide for improving the diffusion, and post heating is needed to reduce the quantity of Tin after dipping step. The film, that covers the cavity after dipping without post – heating was non-uniform, with a presence of big quantity of droplets and thick layer of Tin on the lower flange. On the opposite, the film that was produced with post heating was more uniform, but also with presence of Tin on the lower flange as shown on the figure 7.12.

The parameters of the process are represented in the table 7.6.

№ of the cavity	baking time, hours t, ^{O}C	basic pressure, mBar	pre-heating time, hours t, ^{O}C	dipping time, min t, ^{O}C	post-heating time, hours t, ^{O}C
33	14 120	$3{,}01\times10^{-9}$	//	5 1050	//
5	14 120	$2{,}75\times10^{-9}$	//	15 700	//
25	14 120	$3{,}42\times10^{-9}$	1 1050	10 1050	1 1050
29	14 120	$2{,}41\times10^{-9}$	// //	105 1050	// //

Table 7.6. Dipping parameters of the cavities №№ 33, 5, 25, 29

a) **b)**

Figure 7.12. Cavity after dipping step. Cavity №5 (a) produced without post heating, and cavity № 25 (b) produced with post heating

7.3.3 Inductive annealing

Inductive annealing is the most important step in the LTD technique. The advantages of inductive annealing in comparison with resistive furnace annealing are evident: it is non-contact treatment, the heating process does not contaminate the material being heated. It is also very efficient since the heat is actually generated inside the cavity. This can be contrasted with other heating methods where heat is generated in a flame or heating element, which is then applied to the workpiece.

Procedure of inductive annealing was described in details above, in the chapters 7.1.4, 7.1.5. In the case of annealing the cavity, it was also like a samples, fixed on the support with Niobium wires, as shown on the figures 7.4 (a), 7.13. Power of the heater was regulated manually. All treatments was provide on the output inductor frequency of 85 kHz. Estimated experimentally relating between the output voltage and the temperature of the cavity is shown on the figure 7.14.

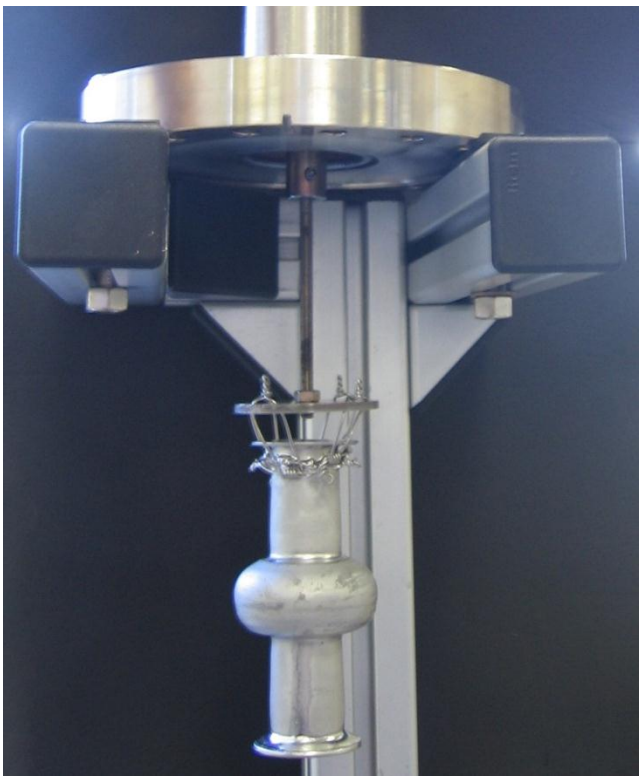

Figure 7.13. Cavity fixed on the support for annealing

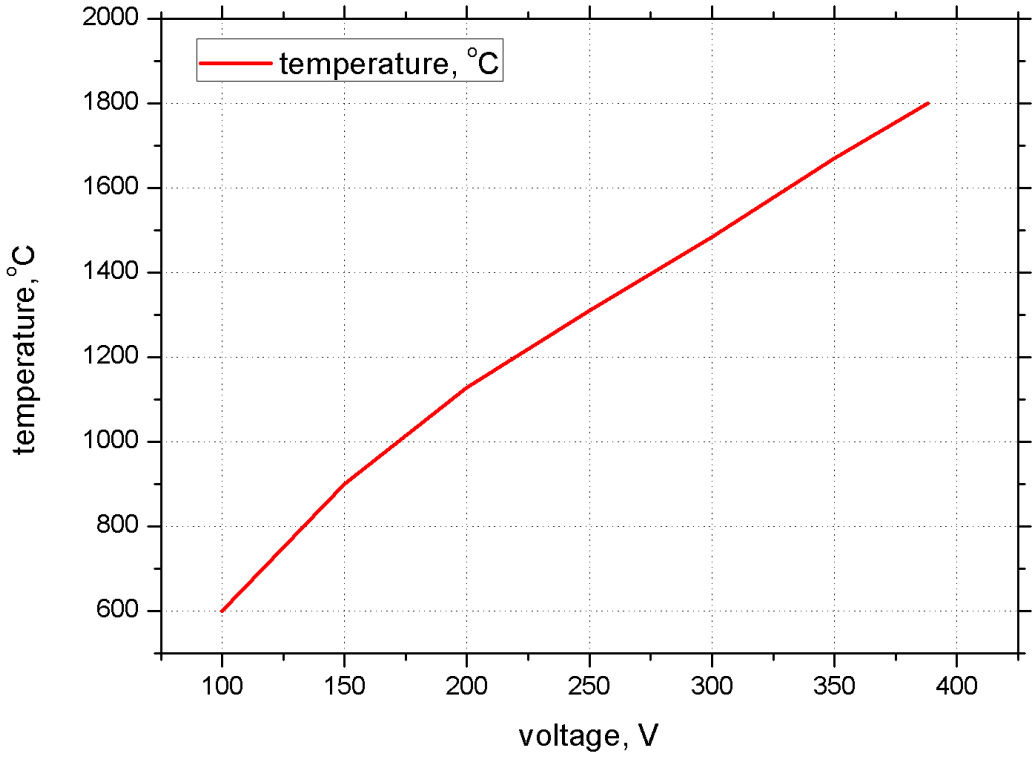

Figure 7.14. Relation between the output inductor voltage and the temperature of the cavity

On the figure 7.15 is shown the process of cavity annealing.

Figure 7.15. Cavity annealing process

Cavity №33 was annealed 2 times, because not all Residual Tin was removed after first annealing. The process parameters of the 1st and 2nd annealing are shown in the tables 7.7 and 7.8 with corresponding photographs of the cavity after annealing on the figure 7.16.

Basic pressure 3×10^{-9} mBar

Voltage, V	Power, kW	Pressure, mBar	Temperature, ^{O}C	Time of step, min
100	0,7	$1,4\times10^{-6}$	//	1
150	1,4	$1,0\times10^{-6}$	980	1
200	2,3	$5,5\times10^{-6}$	1134	2
250	3,3	$6,7\times10^{-6}$	1319	2
300	4,6	$8,5\times10^{-6}$	1500	7
311	5,0	$1,1\times10^{-5}$	//	17

Table 7.7. 1st annealing parameters of the cavity № 33

Basic pressure $7{,}5\times10^{-9}$ mBar

Voltage, V	Power, kW	Pressure, mBar	Temperature, ^{O}C	Time of step, min
100	0,7	$1{,}1\times10^{-6}$	//	1
150	1,4	$6{,}7\times10^{-6}$	900	2
200	2,3	$2{,}6\times10^{-6}$	1128	2
250	3,3	$3{,}2\times10^{-6}$	1310	2
300	4,6	$3{,}2\times10^{-6}$	1485	2
350	6,3	$4{,}9\times10^{-5}$	1670	2
388	7,6	$6{,}6\times10^{-5}$	1800	10

Table 7.8. 2nd annealing parameters of the cavity № 33

after dipping | after 1st annealing | after 2nd annealing

Figure 7.16. Results of annealing cavity №33

On the table 7.9 is represented the parameters of annealing cavity № 5. Here, one can see the abnormal power of 1,4 kW at the output voltage of 400 V. This related to the self – igniting of the plasma inside the coil. The explanation of this phenomena is rather simple: at this temperature (>1800^{O}C) the rate of Tin evaporation becomes very high, the concentration of Sn^{+} ions in the chamber increases and due to the magnetic coupling between the coil of inductor and the cavity (which consequently means the presence of high magnetic field) we have a breakdown. This plasma reduces the resistance between the cavity and the coil and power decreases. Plasma doesn't damage the inductor due to the presence of matching coil between the power supply and the resonant circuit (see chapter 5.3.2, 5.3.5). The picture of the plasma inside the inductor chamber is shown on the figure 7.17.

Basic pressure $3{,}7\times10^{-9}$ mBar

Voltage, V	Power, kW	Pressure, mBar	Temperature, ^{O}C	Time of step, min
100	0,7	$3{,}7\times10^{-7}$	//	1
200	2,3	$2{,}8\times10^{-6}$	900	2
300	4,7	$1{,}6\times10^{-6}$	1428	2
400	1,4	$4{,}6\times10^{-5}$	1810	2
300	4,7	$3{,}2\times10^{-6}$	1485	2

Table 7.9. Annealing parameters of the cavity № 5

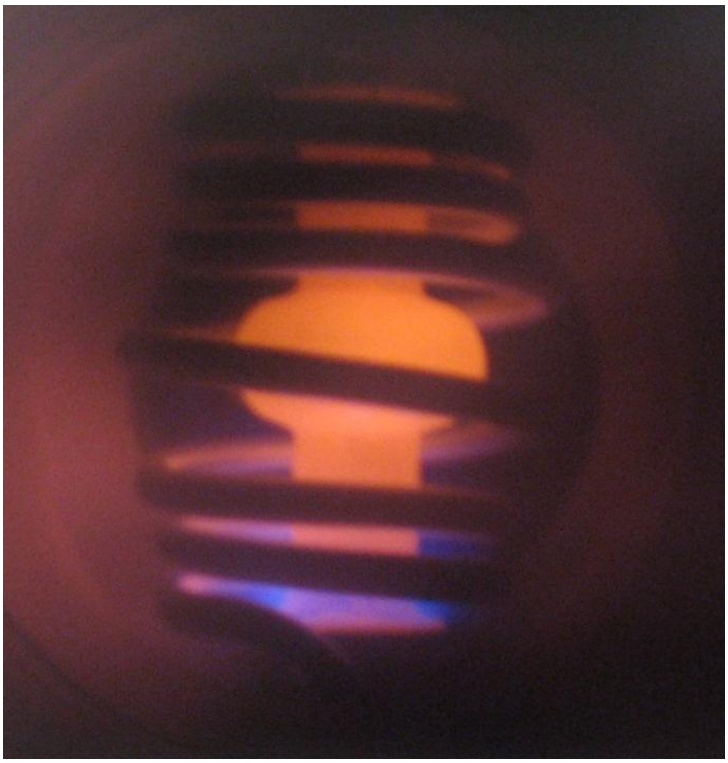

Figure 7.17. Tin – plasma inside the vacuum chamber during the annealing of the cavity

Pictures of the cavity №5 before and after annealing are shown on the figure 7.18.

The next cavity produced was the cavity №25. Table 7.10 represents the results of annealing. The high values of output power at voltages 430 and 300 V corresponds to the plasma ignition in the chamber, that considered to evaporate the residual tin from the cavity in the very short period of time. The mechanism of ignition is described in details in the previous chapter.

after dipping after annealing

Figure 7.18. Results of annealing cavity №5

Basic pressure $1{,}2\times10^{-8}$ mBar

Voltage, V	Power, kW	Pressure, mBar	Temperature, ^{O}C	Time of step, min
100	0,7	$1{,}7\times10^{-8}$	//	1
200	2,3	$2{,}2\times10^{-6}$	1124	10
300	4,6	$4{,}4\times10^{-6}$	1415	1
430	8,9	$3{,}0\times10^{-6}$	1900	0,5
300	8,9	$2{,}6\times10^{-6}$	1482	0,5
200	2,3	$4{,}3\times10^{-7}$	1156	20

Table 7.10. Annealing parameters of the cavity № 25

The pictures of the cavity before and after annealing are shown on the figure 7.19

Beside this cavities, we also tried to anneal the cavities, that were produced by old technique with resistive furnace annealing, which has the droplets of residual tin on the surface. Among them the cavity №22. It was annealed for 30 min. with the temperature of 1200^{O}C. The result of this annealing is described in the chapter 7.4.1.

after dipping

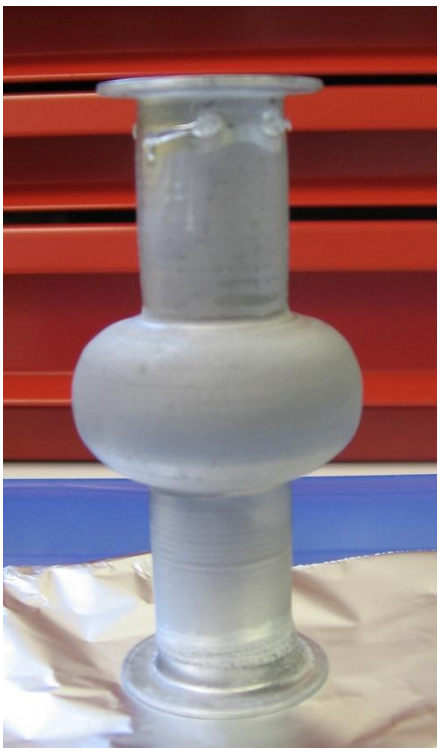

after annealing

Figure 7.19. Results of annealing cavity №25

The parameters and the results of annealing cavity №29 is represented on the table 7.11 and figure 7.20 correspondingly.

Basic pressure $9{,}5\times10^{-9}$ mBar

Voltage, V	Power, kW	Pressure, mBar	Temperature, ^{O}C	Time of step, min
250	3,6	$9{,}2\times10^{-6}$	1300	5
200	2,4	$4{,}4\times10^{-6}$	1050	15

Table 7.11. Annealing parameters of the cavity № 29

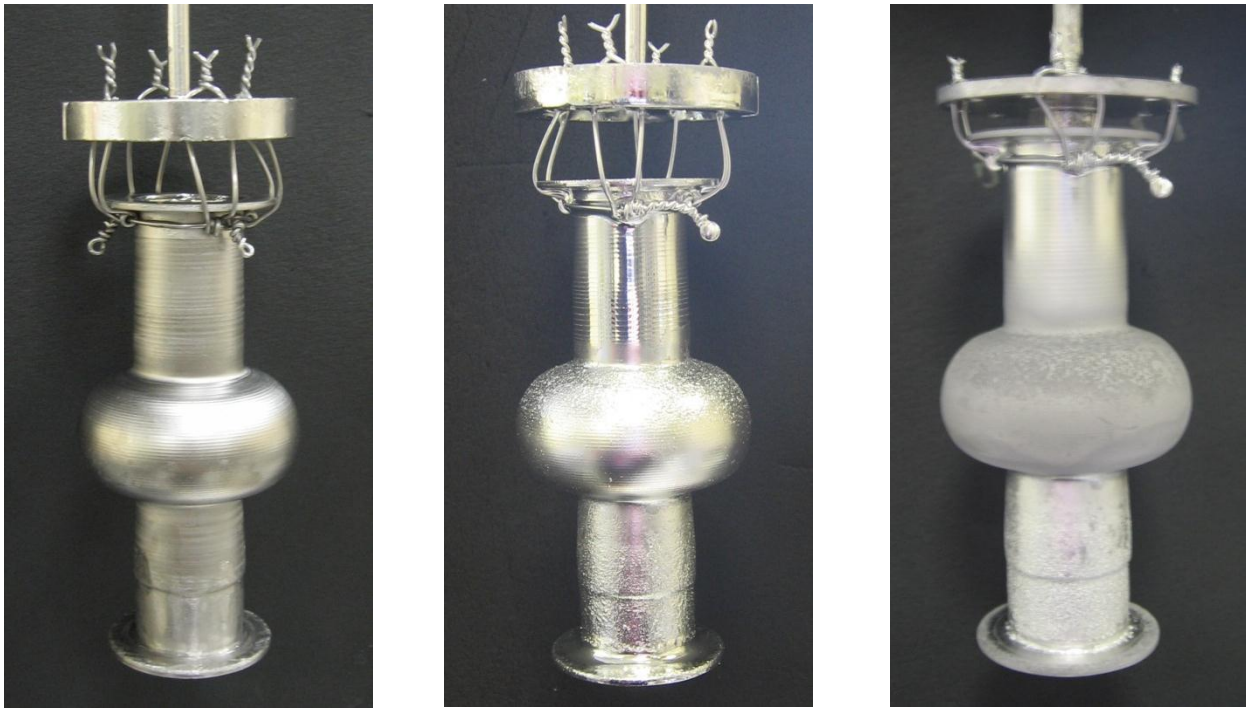

before dipping **after dipping** **after annealing**

Figure 7.20. Results of annealing cavity №29

7.3.4 Post annealing treatment

After providing RF – tests of the cavities №№22, 25 which showed a high Q – value at low magnetization, but fast reducing Q – value with increasing the magnetization, we decide to do a BCP of this cavity in order to reduce roughness of the internal surface. As the solution was chosen the standard BCP solution. And the durations of etching were 20 and 10 seconds correspondingly. The result of RF – test of this cavity is also shown in the chapter 7.4.1.

7.3.5 High pressure rinsing

Microparticle contamination has been identified to be the leading cause of field emission. This stresses the importance of cleanness in all final treatment and assembly procedures. Rinsing with high pressure ultrapure water (HPR) is the most effective tool to remove microparticles and therefore reduces field emission [3]. HPR is also effective in reducing field emission which cannot be processed during an RF-test. The process of HPR of 6 GHz cavity is shown on the figure 7.21.

Figure 7.21. High pressure rinsing of the 6 GHz cavity

7.4 Nb_3Sn 6 GHz cavities analysis

7.4.1 RF – test

During the RF – tests on cold cavities the basic rf properties such as maximum accelerating gradient, field emission, and quality factor Q, as a function of gradient are determined. These tests are done inside the cryostat where the cavity is held vertically. Ideally, these tests are done at or near critical coupling. In addition to improving the systematic errors, setting the fundamental power coupler at or near critical coupling reduces the rf power requirement to a value close to that required for cavity wall losses.

In our case, for providing RF – tests we used the assembly described in the chapter 3.1 which was introduced to the dewar with the liquid Helium with the boiling point of 4,2 K. The arrangement for RF – test was described in details in [24].

The results of RF – tests of all cavities that has been done are plotted on the figure 7.22.

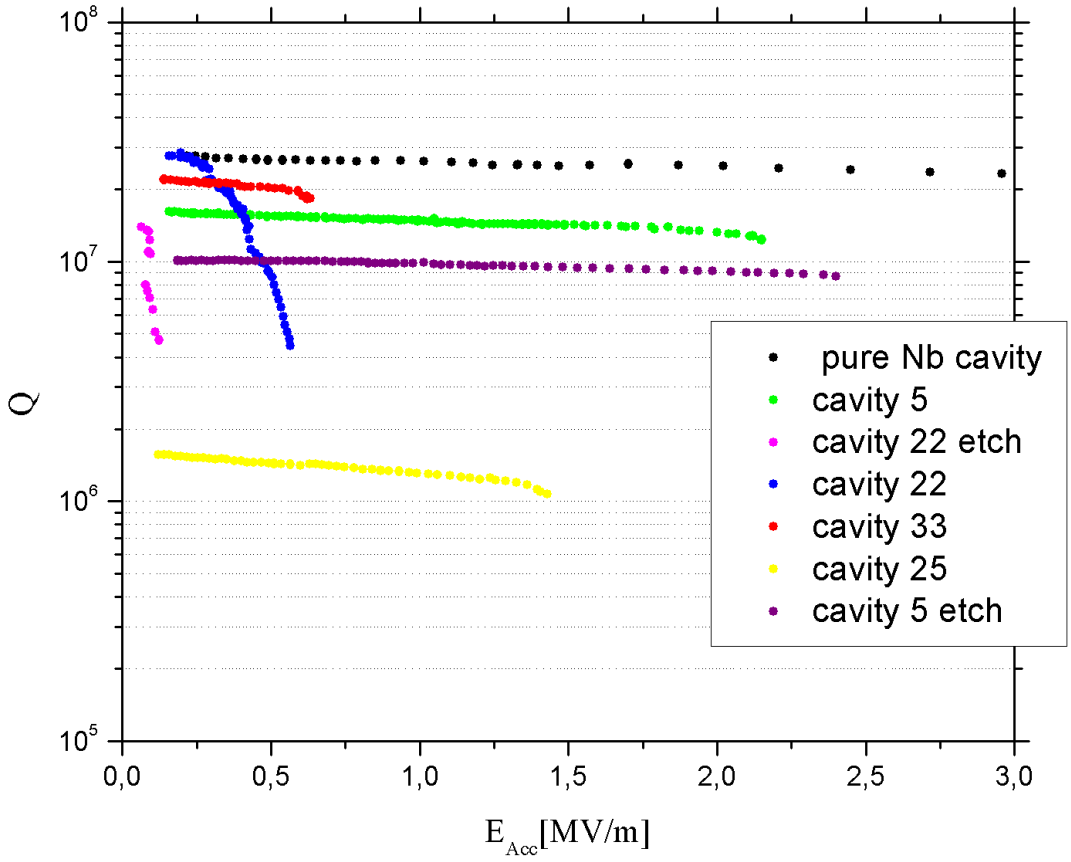

Figure 7.22. The results of RF – tests

8. Discussion

As it was proved during the previous couple years of research, the “classical” liquid Tin diffusion technique with use of so called “double furnace process” with resistive furnace annealing doesn’t shows the satisfactory results on both: the samples and the cavities. The big problem, that we dialed with, using this technique was the presence of the residual drops of Tin on the surface of the sample. Cavities, produced by this technology shows the Q – value factor one order of magnitude lower then pure Niobium cavities. Different combinations of time – temperature regimes of dipping and annealing were tried but the problem has not been solved. In the light of this misfortune efforts, we decide to investigate the influence of different additional surface treatments. Among them there were glow discharge of the sample in the Nitrogen atmosphere, anodization of the surface in the ammonium citrate and chemical etching with use of the mixture of nitric and fluoric acids in the 1:1 proportion. This experiments were done with use of L – samples, which has both vertical and horizontal planes, imitating the problem zones of the cavity (flanges and the horizontal planes of cell-part). But as it was shown above, each of those samples, independently of the treatment method has a residual droplets after annealing. That is why we start thinking about the increasing the annealing temperature. But first of all lets go through the reasons which doesn’t allow us to work at higher temperatures with “standard” annealing. This reasons are:

- use of the external furnace, that means a big losses in heat due to the bad thermal conductivity of the air, which is in between of the furnace and the vacuum chamber;
- the list of possible materials for vacuum chamber, heated up to the temperatures higher then $1000^{O}C$ is not so wide. In our case was produced the Inconel chamber. The Inconel in used compound has the melting point of $1100^{O}C$, so in any case it is impossible to overcome it;
- all the operations must be provided in the ultra high vacuum. But the heated to the temperature over $1000^{O}C$ Inconel chamber, due to the thermal expansion allows the diffusion of contaminations (especially hydrogen) through the wall just from the atmosphere!
- and finally, the maximum temperature, that could be reached with the resistive furnace is $1200^{O}C$, but it is already not so important, because it is limited by the melting point of the Inconel.

That’s why we decide to use another approach. We directed our efforts to finding another king of heater, which doesn’t have all these limitations. These heater is the induction one. Let’s briefly go through the advantages of induction heater:

- The first, and the main advantage is the possibility to reach extremely high temperatures over $2000^{O}C$ without heating the vacuum chamber;
- Possibility to use stainless steel as the material for the chamber;
- fast heating of the substrate, which exclude the formation of spurious phases like Nb_6Sn_5 or $NbSn_2$;

- Excluding the possible contaminations of hydrogen (as in the case of external healer), or Silicon (as in the possible case of using internal lamp heater);
- lack of the necessity to design the water cooling system of the chamber.

The comparative table of two different heating techniques is given on the table 8.1

Parameter	**Induction heater**	**Resistive furnace**
Maximum temperature, ^{O}C	> 2000	1200
Diffusion of contaminations through the wall of the chamber	No	Yes
Material of the chamber	stainless steel	Inconel
Time of heating to 1000^{O}C	< 5 min	3 hours
Cooling	doesn't requires cooling	requires cooling of the pumping zone

Table 8.1. Comparing the characteristics of induction end external resistive heaters

Going through the results of obtaining films of Nb_3Sn on the Niobium samples, one we can make the conclusion, that the critical factor, that influence on the quality of the film is the temperature of annealings. On the picture 8.1 are represented the samples, produced by two different techniques: with resistive furnace annealing and with inductive annealing. The samples, produced with inductive annealing shows a uniform Nb_3Sn film, without the residual Tin droplets. In the same time, it was proved, that the different kinds of preliminary surface treatments such as glow discharge of the sample, anodization of the surface and chemical etching with use of the mixture of nitric and fluoric acids in the 1:1 proportion doesn't influence on the final result.

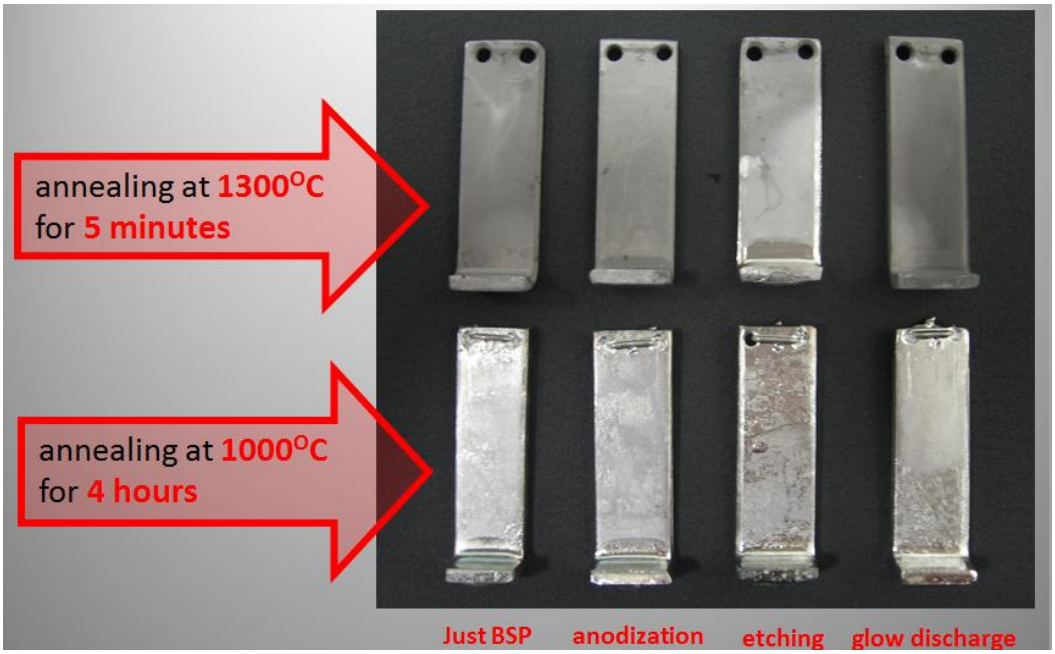

Figure 8.1. Comparative picture of the samples produced by LTD with the resistive furnace annealing and inductive annealing

The results of XRD measurements showed the presence on the surface only the goal compound, which is Nb_3Sn (see pictures 7.9, 7.10).

As for the cavities, the results are also much better. The film of Nb_3Sn on the surface of the resonator is more uniform, without presence of the residual Tin. The highest Q – value has been obtained on the cavity №5, which was annealed for 9 minutes with the highest temperature of $1485^{O}C$. The value of Q in this case is one order of magnitude higher then the Q – value of the cavities annealed on the resistive furnace, and equals $1{,}6\times10^{-7}$, that is pretty close to the pure Nb.

Future developments

The most important thing to do is the improvement of the inductive annealing technology, keep finding the best possible ratio of time/temperature of dipping – time/temperature of annealing parameters.

Another important thing to do is the improvement of the induction annealing system such as designing and installation the water cooling system of the chamber in order to prevent metalising the window with Tin during the annealing process.

As for the samples our future efforts will be directed to the estimation of the optimal thickness of the coating, providing the SEM analysis in order to understand the crystal structure of the films, the XRD measurements for defining the composition.

The future work with the cavities will be dialed with efforts to obtain the maximum uniformity of the film, and maximum Q – value. The new cryostat has been designed and build, that will give us a possibility to measure three cavities simultaneously.

Conclusions

The main purpose of this work was to increase the quality of thermally diffused Nb_3Sn superconductive films over Nb substrates and in particular to avoid the residual droplets of unreacted Tin on the substrate after annealing that was the problem of last couple of years. In order to get a good result two different approaches were applied:

- improving of existing "double furnace technology" by means of different surface pre-treatments, and variation of the time/temperature process parameters;
- development of the new high – temperature annealing technology.

In the framework of improving the "double furnace technology" we studied the influence of preliminary surface treatments such as surface glow discharge, anodization and chemical etching. But it was absolutely proved, that this additional treatments doesn't influence on the quality of the film obtained.

Developing the new technology of high temperature annealing we designed and build the new experimental set up for annealing the 6 GHz cavities by means of induction heater instead of external resistive furnace. With new system it is possible to reach the temperatures over $1800^{O}C$ in less than 5 minutes while the chamber remains relatively cold.

With the new technology it became possible to avoid the residual Tin droplets by means of increasing the temperature of annealing. Samples that were made with use of inductive annealing had the uniform coating. The XRD analysis proved that the only one component of the film is Nb_3Sn. But the T_c value of the samples is not yet satisfactory.

The 6 GHz cavities that had been annealed with induction system had much better Nb_3Sn film than the ones made by "double furnace technology". Unfortunately it still doesn't have the desirable uniformity of the film, but also it doesn't have the residual unreacted Tin. The Q – value of the cavities annealed has the order of magnitude 10^{-7} that is close to the Q – value of pure Niobium cavities.

Also it has been estimated the optimal ratio of time/temperature of dipping – time/temperature of annealing. For the best cavity produced the dipping parameters were 15 minutes at $700^{O}C$ and annealing during 6 minutes at $1800^{O}C$.

However the thermal diffusion technology of obtaining the Nb_3Sn films has not yet achieved its potential performance, but now we have a powerful instrument to advance quickly.

List of tables

List of figures

Bibliography

[1] Michael Tinkham. Introduction to Superconductivity, 2nd edition (1996). McGraw-Hill

[2] J. Bardeen, L. Cooper, J. R. Schrieffer, *Theory of superconductivity*, Physical Review 108 (1957) 1175.

[3] H. Padamsee, J. Knoblock, T. Hays, RF Superconductivity for Accelerators, Wiley and Sons, New York, 1998

[4] J. Jackson, Classical Electrodynamics, Wiley, New York, 2nd edition, 1975.

[5] K. Halbach, R. Holsinger, Particle Accelerators 7 (1976) 213 – 222.

[6] B. Bonin, Commissariat à l'Energie Atomique, DSM/DAPNIA, France « Materials for superconducting cavities »

[7] R. Vaglio, Alternative superconducting materials for rf cavity applications., in: Proceedings of the 8th Workshop on RF Superconductivity, Abano Terme, Padova, Italy,1997.

[8] S.V.Vonsovsky, Yu.A.Izyumov, E.Z.Kumaev, "Superconductivity of transition metals", Springer-Verlag (1982)

[9] V. Palmieri Istituto Nazionale di Fisica Nucleare, Laboratori Nazionali di Legnaro, Legnaro (Padua), ITALY «New Materials for Superconducting Radiofrequency Cavities» Proceedings for the 10th Workshop on RF Superconductivity, 2001, Tsukuba, Japan

[10] G.F.Hardy and J.K. Hulm, Phys. Rev. 87, 884 (1953); 93, 1004 (1954)

[11] B.T. Matthias, T. Geballe, S. Geller, F. Corenzwit, Phys. Rev. 95, 1435 (1954)

[12] S.V.Vonsovsky, Yu.A.Izyumov, E.Z.Kumaev,"Superconductivity of transition metals, their alloys and compounds", Springer-Verlag (1982)

[13] R. Blaugher, R. Hein, R. Cox, J.E. and Waterstrat, J. Low Temp. Phys. 1 (1969) 531.

[14] E. Savitskii, V. Baron, Y. Efimov, M. Bychkova, L. Myzenkova, Superconducting Materials, Plenum Press, New York, 1973.

[15] J. Jorda, R. Flukiger, J. Muller, J. Less-Common Met. 55 (1977) 249.

[16] S. Moehlecke, PhD Thesis, Universidad Estudial de Campinas, Brazil, 1977.

[17] H. Maeda, K. Inoue, T. Kiyoshi, T. Asano, Y. Sakai, T. Takeuchi, K.Etoh, K. Aoki and G. Kido, Physica B 216, 141 (1996)

[18] A. Godeke, International SRF Thin Films Workshop 2006, INFN-LNL, http://master.lnl.infn.it/thinfilms/ (Lawrence Berkeley National Laboratory. Paper LBNL-62140)

[19] J. Yasatis, R. Rose, IEEE Trans. Magn. 11 (1975) 434.

[20] Proceedings de "14th International workshop on RF Superconductivity" (SRF 2009), p.149; web site: http://accelconf.web.cern.ch/AccelConf/srf2009/papers/tuobau06.pdf

[21] Proceedings de "14th International workshop on RF Superconductivity" (SRF 2009), p.155; web site:http://accelconf.web.cern.ch/AccelConf/srf2009/papers/tuobau07.pdf

[22] V. Palmieri, .Spinning of TESLA-Type Cavities: Status of Art., Proc. of the 9th Workshop on RF superconductivity, Santa Fe, USA, Nov. 1999, pp 532-537.

[23] C. Pira "Titaniocromia tramite ossidazione anodica". Bachelor thesis, academic year 2003-2004. Supervisor prof. V. Palmieri.

[24] S.M. Deambrosis "A method to test A-15 intermetallic compounds rf properties". PhD thesis, academic year 2007-2008. Supervisor prof. V. Palmieri.

[25] S.M. Deambrosis, V. Rampazzo, A.A. Rossi, V. Rupp, R.G. Sharma, S. Stark, F. Stivanello, and V. Palmieri "A-15 superconductors by thermal diffusion in 6 GHz cavities" Proceedings of SRF2009, Berlin, Germany

[26] M. Straumanis, S. Zyszczynsk, J. Appl. Cryst. 3 (1970) 1

[27] H. Devantay, J. Jorda, J. Decorux, M. and Muller, R. Flukiger, J. Mat. Sci. 16 (1981) 2145

[28] D. Dew-Hughes, Cryogenics 15 (1975) 475.

[29] R. Flukiger, H. Kupfer, J. Jorda, J. Muller, IEEE Trans. on Magn. MAG-23 (1980) 980.

[30] M. Beasley, Adv. Cryog. Eng. 28 (1982) 345.

[31] Julius Adams Stratton. Electromagnetic theory. IEEE Press, Piscataway, NJ, 2007.

[32] Mattew N.O. Sadiku. Elements of Electromagnetics, volume 3. Oxford University Press, Inc., 2001.

[33] Web site dedicated to induction heating systems http://www.richieburnett.co.uk/indheat.html